Researches on Gradient Index Lens Using Perforated Dielectric

	Wenyi Shao
	Tohoku University
	11301 20382
URL	http://hdl.handle.net/10097/00135883

RESEARCHES ON GRADIENT INDEX LENS USING PERFORATED DIELECTRIC

（空洞誘電体を用いた屈折率分布型レンズに関する研究）

by

WENYI SHAO

A dissertation

Submitted to Tohoku University

in partial fulfillment of the requirements for the degree of

Doctor of Philosophy

Department of Communications Engineering

Graduate School of Engineering, Aobayama Campus, Sendai, Japan

April 2022

Dedicated to my beloved parents, my caring elder brother and my respectful supervisor

ACKNOWLEDGEMENTS

ABSTRACT

Gradient index (GRIN) lens has attracted significant interest for its attractive properties, such as broadband, high gain and competitive efficiency in micro- and millimeter wave applications. There have been several well-known GRIN lenses, such as Luneburg lens, Maxwell fisheye lens, and Eaton lens. Although these lenses have various refractive index pro files defined under different spatial coordinates, a common feature among them is the spherical nature of their shapes that poses a significant manufacturing challenge. To overcome such limitations, a more convenient approach is to use extremely complex transformation optics (TO) to design flat shaped lens while maintaining the original electromagnetic performances. Moreover, the GRIN lens has been manufactured by metamaterials consisting of many sub-wavelength metallic resonant structures. However, metamaterial has the inherent drawbacks of large loss and narrow bandwidth as well as complicated and expensive fabrication process exist. In addition, to obtain the high-resolution images in micro and millimeter waves imaging, imaging systems must require a large lens. But the larger the lens, the more obvious the tendency of spherical aberration, which in turn limits the resolution of micro and millimeter waves imaging.

In this dissertation, inspired by optical fiber, a new lens antenna type called hyperbolic secant (H-S) lens antenna with high gain, broadband and high-resolution imaging characteristic was proposed to solve above-mentioned drawbacks. The design theory for proposed hyperbolic secant lens based on 2-by-2 ray matrix transfer analysis, and the unique structural extensibility of lens was discussed and explained in detail, which provides a very useful analytical method for the study of high directive and beam scanning application for H-S lens. Moreover, the fabrication methods by using perforated and infill structure for 3-D printing was briefly introduced, which guarantees a simple and economical way to fabricate H-S lens prototype compared with other manufacturing technologies such as foam pressing, PCB milling and metamaterials with metallic

resonant. Most importantly, the attractiveness of this new lens concept is its intrinsic flat shape characteristic and extensibility for different antenna application scenarios, in addition to the advantages of low-profile, lightweight, and high performance. Compared with conventional Luneburg, Maxwell fish-eye, and Eaton lens, the proposed lens has the unique flat shape characteristic, which provides great advantages in designing the low-profile planar lens antenna, avoiding using extremely complex conformal mapping methods.

Moreover, the functionality of high directive, beam scanning, and subwavelength imaging was first explored in detail in this dissertation. The corresponding all dielectric H S lens prototype was fabricated and verified without using complex transformation optics method. A high gain and wideband printed antipodal fermi antenna as feeding source are employed in the proposed lens antenna prototype operating at 10 GHz. The simulated and experimental results showed good agreement, demonstrating 23.8 dBi realized gain at 10 GHz with 3-dB beamwidth of 9° and 2-dB fractional realized gain bandwidth of 41.6%. The total radiation efficiency is above ~40% across all tested frequencies (8.2GHz-12.5GHz), which suggests the proposed H-S lens antenna itself has intrinsic broadband response. Based on 2-by-2 ray transfer matrix analysis and full wave simulation, the beam scanning capability for proposed H-S lens was explored by mechanically moving the waveguide. The beam scanning capability in both the E-and H-plane was confirmed. It has been demonstrated that we can achieve 2-D beam steering in both the E-and H-plane among the effective beam-steering range ($\pm 20°$) with around 18.9 dBi of realized gain with less than ~1.2 dB variation and low side-lobe.

In order to solve the drawbacks of mechanical beam scanning, a beam-switching planar H-S lens antenna concept achieved by electronic switch was also proposed, which allows for a simple low-cost planar feed technology. Based on ray tracing analysis and full-wave electromagnetic simulation, the performance of proposed lens prototype excited by five rectangular microstrip patch has been evaluated at 10 GHz. It has been demonstrated that we can achieve beam-steering capabilities in H planes from $-20°$ to

+20° with around 13.2 dBi of realized gain and SLL (less than −11.5dB), and up to ±30° with around 10 dBi of realized gain. Moreover, higher steering angles lead to higher phase error resulting from comatic aberration and deterioration of the corresponding radiated beam. Most importantly, the realized gain, efficiency and SLL can be further improved to get better radiation performances by using other 3-D printing materials with lower loss tangent or more advanced manufacturing technology.

Besides, two H-S lens type operating at X and Ka band using perforation and infill structure was utilized to achieve the high image resolution of ~0.5λ with broadband behavior and small physical aperture for the single pixel scanning micro and millimeter wave imaging. Based on time domain measurement method, the spatial resolution imaging experiment was carried out to demonstrate the excellent imaging performance for the designed lens prototype with high resolution of ~0.5λ, which revealing great potential for high resolution micro- and millimeter-wave imaging applications. The functionality of the proposed lens concept can be further expanded to higher frequency bands such as THz by using advanced nanotechnology. The proposed H-S lens concept with surface focusing has great potential to obtain the accurate size and shape information of imaging target with small lens physical aperture. In summary, the proposed H-S lens concept in this dissertation with unique structural extensibility for multi-purpose antenna applications will greatly contribute in the field of the lens antenna with enhanced performance and expanded functionalities.

x

TABLE OF CONTENTS

LIST OF FIGURES

LIST OF TABLES

CHAPTER 1

Introduction

A detailed introduction on different lens antenna systems compatible for the applications of the next generation wireless communications (beyond 5G/6G) systems and imaging is provided to illustrate the current trends of lens antenna. Specifically, summary on different types of lens antenna solutions such as hyperbolic lens antenna, Fresnel lens antenna, half Maxwell fish-eye lens antenna and Luneburg lens antenna is further discussed in section 1.2. The emphasis on importance and advantages of lens antenna is the top priority in this chapter. Besides, there are some problems in previous studies about lens antenna, which can be further improved. In order to solve these problems, inspiring by optical fiber, a new lens antenna type called hyperbolic secant (H-S) lens antenna with high gain, broadband and high-resolution imaging characteristic was introduced in the section 1.3. The main purpose of this thesis is to conduct a detailed and feasibility study of H-S lens antenna. The thesis framework is given in section 1.4.

1.1 Background

Lens antennas have been widely used for many applications at micro- and millimeter wave, like imaging systems [1, 2, 3], massive MIMO systems[4, 5], next generation wireless communications (beyond 5G/6G) systems [6, 7, 8] and radar systems [9, 10, 11], due to their simplicity, invulnerability to small imperfections, compact and flexible beam steering ability. Especially, the unprecedented demand in modern wireless communications systems, such as ever-higher data rate and capacity, motivates the development of highly directive antenna with low power consumption.

So, in recent years, the lens antenna has regained extensive attention in industry with the rapid advances in the millimeter and sub-millimeter waves circuit technology. In [12], the mmWave lens antennas aimed to be used in hybrid beamforming structure, as shown in Figure 1-1. The microstrip patch array antenna with patch spacing of 10 mm is

placed at the focal plane of lens. Each patch antenna can be conceded to be an independent port that produces a single radiation beam. The beam-switching feasibility of lens antenna is achieved by activating the port status. The measurement and simulation results prove the properties of lens antennas of much higher gain and directivity compared to those in which no lens is used.
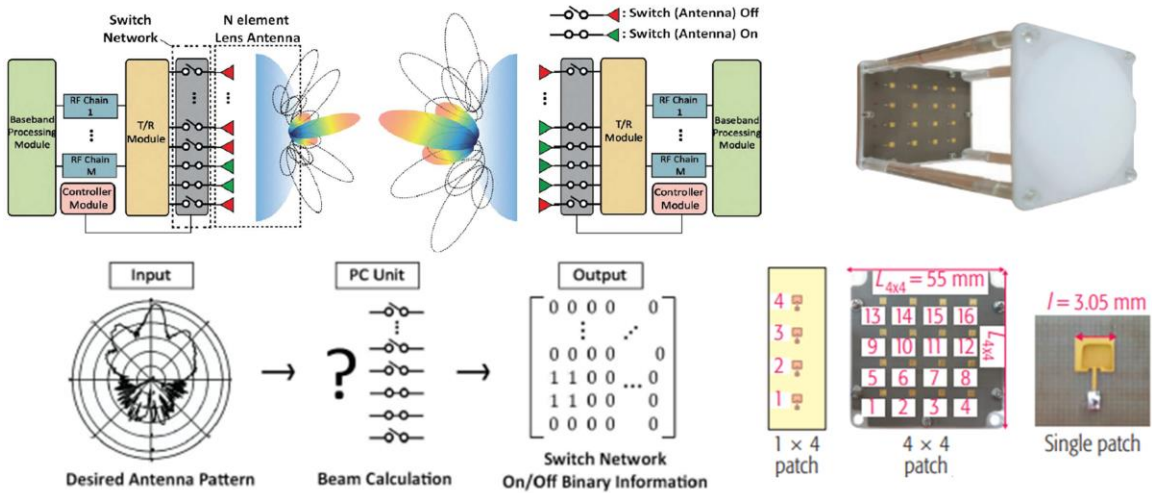
Figure 1-1 The lens-embedded mmWave hybrid beamforming system at 28GHz[12]

Compared with the off-body fed lens antenna, the integrated lens antenna (ILA) has more compact structure, which make it more attractive in the millimeter wave applications. As shown in Figure 1-2, an electronically beam steerable integrated lens antenna for commercial 71-76/81-86 GHz backhaul system was performed during a 3-month test at a mobile operator's network in [13]. In order to increase the bandwidth of the microstrip patch antenna to cover the whole 71-86 GHz band, the microstrip patch antenna with three layers of dielectric substrate was utilized. In addition, the single pole four throw (SP4T) switch controls the radiated beam direction by choosing the transmitted signal for only one of the antenna elements while isolating all other antenna elements in the array.
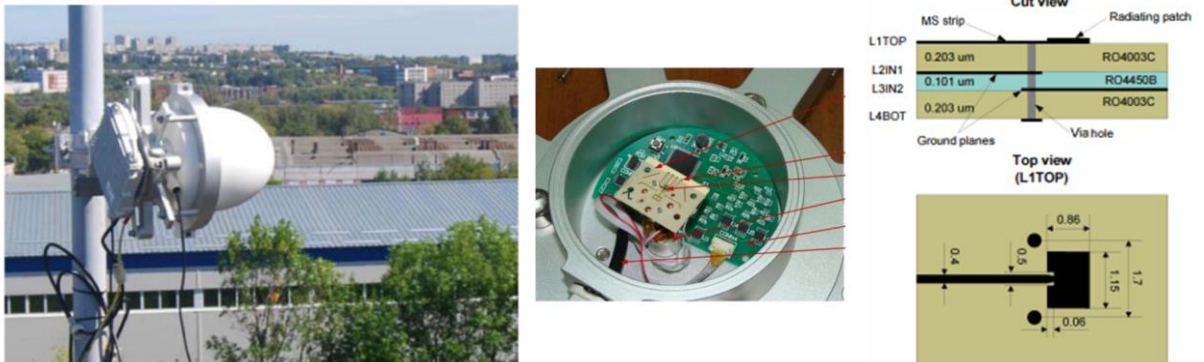
Figure 1-2 The electronically beam steerable integrated lens antenna for 71-76/81-86 GHz backhaul applications[13].

Similarly, the architecture of the integrated lens antenna with a 64-element feed antenna array for E-band 2-D beam-steering capability was presented in [14], as shown in Figure 1-3. The beam steering is controlled by utilizing a number of SP4T GaAs p-i-n diode switches to switch between the feed elements. The continuous beam-steering range of about $\pm 4° \times \pm 17°$ with high gain (> 28 dBi), with low sidelobes from 71 to 76 GHz were achieved.

Figure 1-3 The Nokia millimeter wave (mmW) access and the backhaul demonstrators at E-band based on the beam steering lens antenna[14].

Besides, high resolution quasi-optical system for micro- and millimeter-wave imaging has received significant interest in recent years for a wide range of applications

23

including security imaging, nondestructive detection and biomedical examinations, due to the penetrating capabilities of micro- and millimeter-wave with non-ionizing radiations. Lens antenna with high resolution focusing and broadband bandwidth is one of the most critical devices in quasi-optical millimeter-wave imaging system. In [15], a dielectric aspheric lens operating at 77 GHz was fabricated by using the polyethylene material. the one-dimensional imaging sensor called antipodal fermi antenna (APFA) has 25 individual elements with width of 4 mm and the pitch of 8 mm. The flapping reflector structure is utilized to guarantee imaging speed in fast frame rates. According to the Rayleigh criterion, the spatial resolution of the whole system can reach 20 mm.
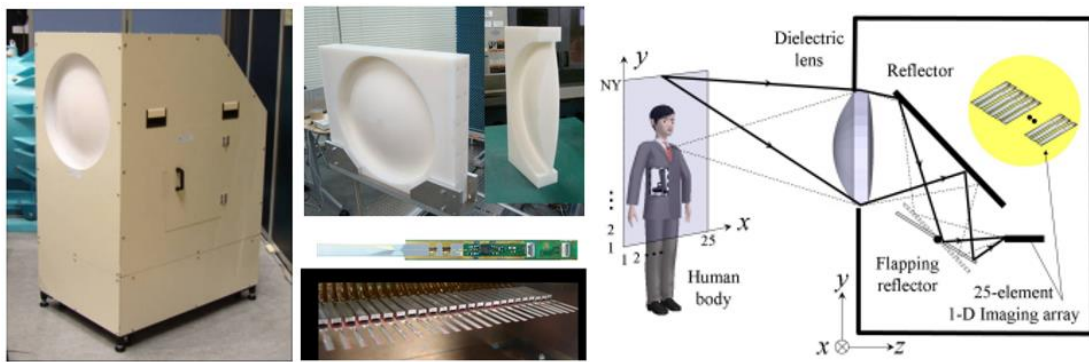
Figure 1-4 77 GHz mm-wave passive imaging system[15].

The broadband characteristics of lens can guarantee that the imaging system is able to cover a large frequency range. Moreover, non-polarized lens is very convenient for obtaining the multiple polarization information of imaging object when simply changing the polarization characteristics or direction of feeding source. In [16], a passive polarimetric imaging system at the W-band for human body imaging was proposed, as shown in Figure 1-5. The lens in the imaging system has a diameter of 460 mm and can converge the bandwidth of 40 GHz (70 ~ 110 GHz). The corresponding spatial resolution is about 2 cm at a distance of 2.5 m.
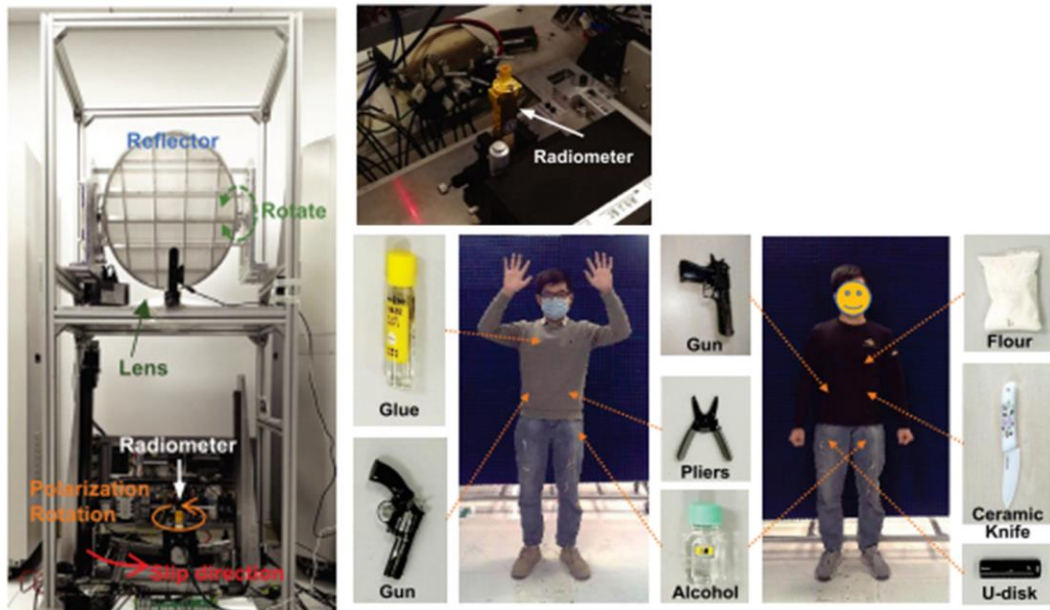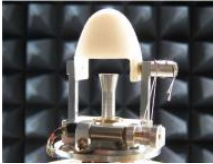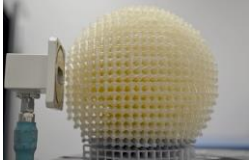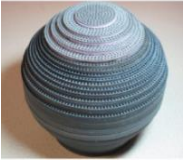
Figure 1-5 W-band passive polarimetric imaging system for human[16].

In summary, lenses are very flexible and simple to design and fabricate for obtaining high gain radiation beam, which can be reliable alternative at high frequencies to other antennas. Although it has been explored since the last century, lens antenna still plays an important role in some application fields such as broadband wireless communications and imaging applications.

1.2 Previously studies on gradient index (GRIN) lens antenna

There are many types of lenses proposed in the field of antenna engineering. It is mainly divided into two categories: homogeneous and non-homogeneous lens, as shown in Table 1-1. The homogeneous lens has optimal geometry shaped profiles such as spherical [17, 18, 19, 20], extended hemispherical [21, 22, 23, 24], elliptical [25, 26]. For the non-homogeneous lens (also called GRIN lens), several materials with different dielectric constant or refraction index are utilized to construct the lens. It should be noted that the refraction index variation can be achieved by using same material based on effective medium theory.

Table 1-1 Types of lenses proposed in the field of antenna engineering

Lens antenna			
Homogeneous		Non-homogeneous	
[27]	[28]	[27]	[29]
Advantage: High efficiency, large bandwidth		Good efficiency, flexible scanning capabilities	
Disadvantage: High-profile, massive bulky		High-profile, non-Flat, and cumbersome	

In section 1.1, the applications of several typical homogeneous lens types are introduced in detail. In the following, a summary on different types of non-homogeneous lens arrays is presented. There have been several well-known GRIN lenses, such as Luneburg lens [30, 31, 32], half Maxwell fish-eye (HMFE) lens [33, 34, 35], and Eaton lens [36, 37]. In [39], a compact metamaterial-based substrate-integrated Luneburg lens antenna operating at X-band was proposed as shown in Figure 1-6. The dimension of the whole antenna is 130×190 mm with the height of 11 mm. A two-dimensional array of waveguided units of complementary closed-ring (CCR) resonators was utilized to achieve the gradient index profile of the Luneburg lens. Based on the printed circuit board technique, the proposed lens is excited by an integrated Vivaldi antenna. The radiation performance under different frequencies is not perfect, which could be mainly due to the metallic closed-ring resonators.
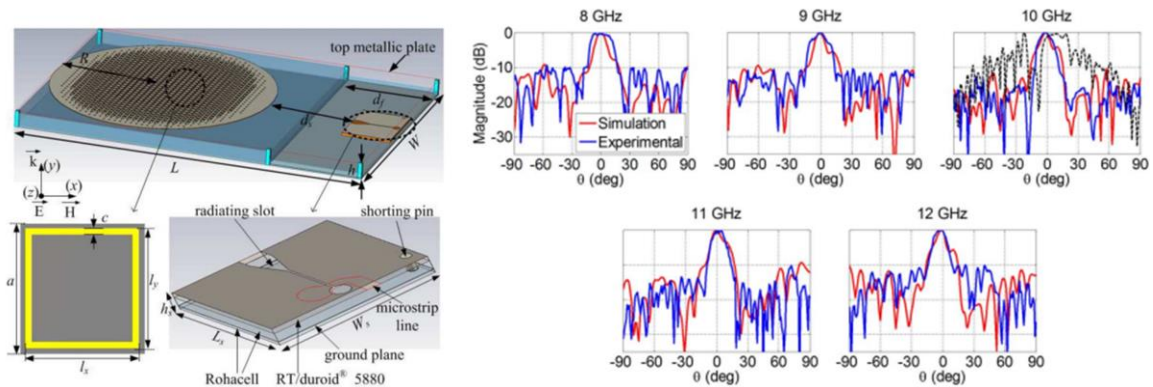
Figure 1-6 X-band metamaterial-based substrate-integrated Luneburg lens antenna[38].

Like Luneburg lens, Maxwell fish-eye (MFE) lens is also a spherical shape GRIN lens. However, due to the limitation of the intrinsic Maxwell fish-eye lens that convert a point source at the lens surface into another point source at the opposite side of the lens, half of the MFE lens is usually utilized as a highly directive antenna in practical antenna application. In [39], a two-dimensional HMFE lens antenna using the I-shaped metallic resonant structure was proposed, as shown in Figure 1-7. The radius of the designed HMFE lens is 48 mm with a thickness of 12 mm. Bases on the lithography technology, the I-shaped PCB strips were fabricated. It was demonstrated that the HMFE lens can transform spherical wave into plane wave to obtain high realized gain. Although the proposed HMFE lens antenna has a good directive behavior, the specific bandwidth characteristic and efficiency has not been analyzed.
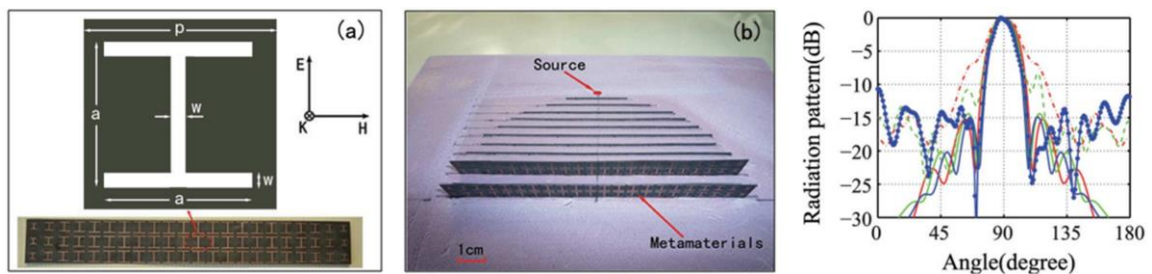
Figure 1-7 Two-dimensional HMFE lens antenna at X-band using I-shaped metallic resonant structure[39].

Other type of spherical GRIN lens is Eaton lens that has the unique beam deflection. In [37], a two-dimensional 90° rotating Eaton lens based on a meta-surface of

square metallic printed patches on a grounded substrate and mushroom structure was proposed, which can bend the direction of surface wave propagation by 90° as shown in Figure 1-8.
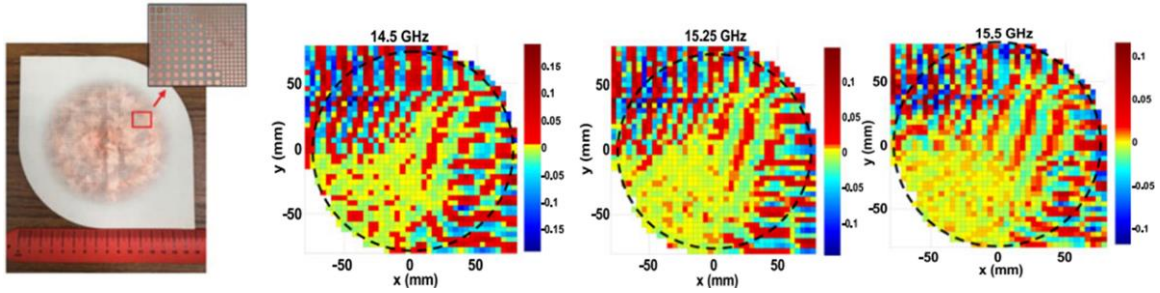
Figure 1-8 90° rotating Eaton lens based on metamaterial and measured E-field patterns at different frequencies[37].

Besides, other material structures such as air-holes and cube-shaped structures based on effective medium theory are utilized to achieve intended permittivity distribution by additive manufacturing or PCB milling techniques. Foam and ceramic materials are also utilized to generates the various permittivity values for satisfying the desired GRIN lens profile. In [40], a 1-D flat Luneburg lens fed by the WR15 open-ended waveguide by using Airex PXc foams was presented, as shown in Figure 1-10. By the special pressing process to control foam material proportion, the corresponding permittivity of material can be obtained. The continuous permittivity profile of Luneburg lens was discretized into 5 homogeneous layers fabricated by the Airex PXc 245 foam and one extra air layer fabricated by Rohacell HF51 foam. The measured radiation patterns in H-plane at 57 GHz, 61 GHz and 65 GHz and loss efficiency is shown in Figure 1-10. The measured gain of ~16dBi can be achieved with loss efficiency of around 60% over the whole bandwidth (57GHz-65GHz).
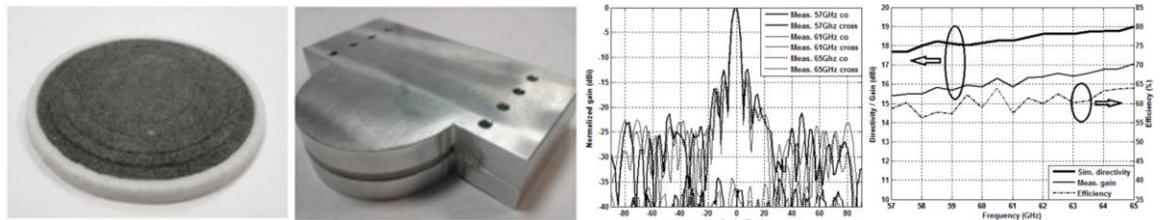
Figure 1-9 A foam-based Luneburg lens of diameter 56mm fed by the WR15 open-ended waveguide[40]

In [41], benefiting from ceramic 3-D printing technology, a flat and lightweight Luneburg lens operating at Ku-Band was fabricated using low-loss MgTiO3 ceramic slurry without complex molds process, as shown in Figure 1-10. The diameter and thickness of the fabricated lens prototype is 70.9 and 7.9 mm, respectively. The unit-cell of is a square structure with air-hole. By controlling the size of air-hole, the effective permittivity of the unit-cell can be changed. While maintaining broadband behavior, the proposed flat lens can achieve maximum measured gain of 19.1 dBi with the side lobe levels of −15 dB.
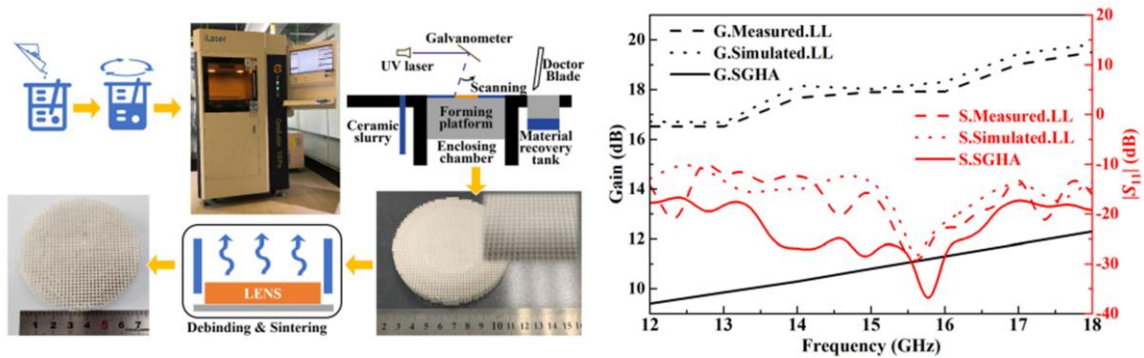
Figure 1-10 A ceramic-based Ku-Band flat Luneburg lens using ceramic 3-D printing [41].

In addition, the GRIN lens can be manufactured by easily accessible 3-D printing technique using low-cost dielectric material. Unlike above-mentioned foam pressing and ceramic 3-D printing technique, this method does not need a complicated and expensive fabrication process. In [42], a light weight, broadband and high gain planar GRIN lens was designed and fabricated by 3-D printer using thermoplastic polylactic acid (PLA), as shown in Figure 1-11. Actually, the proposed lens is a type of Fresnel lens with porosity control in homogeneous material. The diameter and thickness of fabricated lens prototype is 120 mm and 18.5 mm respectively. It has six discrete dielectric concentric cylindrical rings with the width of 10 mm. By controlling the infill ratio of material or volume fraction of the air holes in the unit-cell, the desired effective relative permittivity of the unit-cell can be obtained. The measured gain patterns of the lens in the E- and H-plane for the frequency of 12, 15and 18 GHz can be seen from Figure 1-11. The proposed lens

fed by a conical horn can achieve the broadband realized gain of 16 to 24 dBi over the Ku-band from 12 to 18 GHz.
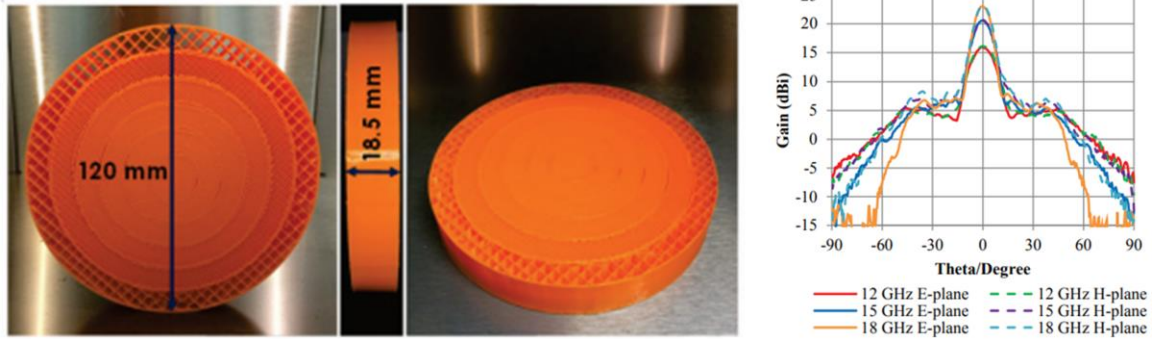
Figure 1-11 A planar GRIN lens was designed and fabricated by 3-D printer using PLA dielectric material[42].

1.3 Problem statement and motivation

If we want to use these GRIN lens antennas such as Luneburg lens and Maxwell fish-eye lens, we need to overcome some problems or drawbacks. Although these lenses have various refractive index profiles defined under different spatial coordinates, a common feature among them is the spherical nature of their shapes. The typical Luneburg lens is spherical symmetric GRIN lens, whose refractive index varies radially from the center to the outermost surface. It has excellent properties such as intrinsic broadband behavior and focusing beam from all directions equally well [43], which exhibits a narrow beam and multibeam capacity. Like Luneburg lens, the Maxwell fish-eye lens is another typical GRIN lens, which can transform a point source to a diametrically opposite focal point on the lens rim. In practical antenna application, half Maxwell fish-eye lens (HMFE) structure was proposed and utilized as a highly directive antenna [44]. But the manufacture of the constantly changing radial permittivity distribution of Luneburg and HMFE lens turns out to be challenging and complex. The characteristic of high profile also poses a significant challenge for manufacturing, feed installation, and antenna system implementation.

In order to eliminate the limitation of its spherical or hemispherical shape, a more complex approach is to use transformation optics (TO) [45], quasi-conformal

transformation optics (QCTO) [46] or field transformation (FT) [47] to form a planar Luneburg lens and hemispherical while maintaining the original electromagnetic performances. Furthermore, the GRIN lens is mainly manufactured by metamaterials consisting of many sub-wavelength metallic resonant structures. Compared to porous dielectric structures, the inherent drawbacks of large loss and narrow bandwidth as well as complicated and expensive fabrication process exist. As above-mentioned, although other materials such as foam and ceramic materials are also utilized to generates the various permittivity values, these methods need a complex and special process techniques.

In addition, there are three common parameters for evaluating imaging systems [48]: spatial resolution, contrast, and depth of view. Among these parameters, the spatial resolution is the most crucial parameter that defines imaging quality. Unfortunately, micro- and millimeter-waves have a long wavelength compared with those of visible light, which inherently limit the resolution of imaging. In order to obtain the diffraction-limited images with high spatial resolution, imaging systems must require a large physical aperture of lens that make the overall system more bulky, complex, and high cost. Besides, the larger the lens, the more obvious the tendency of spherical aberration, which in turn limits the resolution of micro- and millimeter-waves imaging. It is very difficult to obtain the accurate size and shape information of imaging target in the existing imaging system.

So, in order to overcome the above-mentioned drawbacks, a new lens concept [49,50] from optical fiber or graded-index optics is applied in this dissertation. This new self-focusing cylindrical lens structure has not been exhaustively reported in the literature of micro- and millimeter wave applications, thereafter known as hyperbolic secant (H-S) lens. It is also called hyperbolic cosine lens or Mikaelian lens. The main difference of the H-S lens with respect to the Luneburg and HMFE lens is its intrinsic flat shape characteristic. It means the complex TO, QCTO or FT mapping methods is not required to flatten the particular shape (e.g., spherical shape) of lens. Moreover, the refractive index profile of H-S lens is the axial-symmetric, which makes it easier and quicker to manufacture. Because it is a more general form of quadratic index profiles (another

31

GRIN index profile), the optimum structural size of H-S lens for integrated lens antenna and off-body fed lens antenna configurations could be easily determined by selecting the appropriate gradient parameter of H-S index profile, as shown in Fig. 1-12. The suitable feeding source can be placed at the focal point of lens to achieve good radiation performance. Moreover, as one of the most fundamental and important properties, the beam-steering capability of H-S lens has not been investigated in the literature of microwave or millimeter wave applications. In this dissertation, we want to explore the focusing properties and be beam-steering capability of H-S lens in detail.

Most importantly, the proposed H-S lens is spherical aberrations free lens. It means the off-center rays have the same focusing behavior as paraxial rays, which enables to focus rays to the smallest possible spot in subwavelength scale. The very small focal spot can guarantee excellent imaging performance to obtain the accurate size and shape information of imaging object. this unique characteristic of surface focusing provides a potential way to ensure a higher numerical aperture, which produces a more highly resolved image. But in previous study, there is not much information about how to put this lens concept into practice, not to mention the practical imaging application. Another purpose of this dissertation is to apply the surface focusing H-S lens with a compact structure, simple fabrication process and cost-effectiveness into a single-pixel scanning micro- and millimeter-wave imaging application.
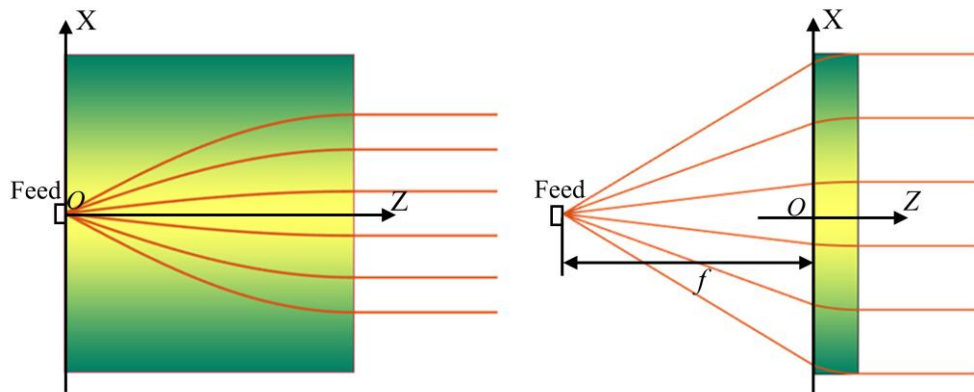
Figure 1-12 The schematic diagram of the extensible characteristics of H-S lens. (Left) Typical H-S lens for integrated lens antenna. (Right) Generalized H-S lens for off-body fed lens antenna.

1.4 Thesis framework

This thesis is divided into six chapters which is proceed as follows.

In Chapter 2, general theory and analysis methods of lens antennas are presented. Particularly, the design theory for proposed gradient index (hyperbolic secant) lens based on ray transfer matrix analysis, and the unique structural extensibility of lens is discussed and explained in detail. The dynamic ray tracing process for H-S lens was verified by full-wave simulation, which provides a very useful analytical method for the study of beam scanning application for H-S lens in Chapter 4. Moreover, the additive manufacturing (3-D printing) technology for proposed H-S lens is briefly introduced. The specific fabrication methods by using perforated and infill structure are introduced, which provide a simple and economical way to fabricate H-S lens.

In Chapter 3, the high radiation performance generalized hyperbolic secant (H-S) lens for broadband high directive antenna applications is designed, fabricated, and tested in X-band (8.2-12.5 GHz). The proposed lens protype are characterized by both simulations and measurements. The functionality of 2-D beam-scanning for H-S lens is also explored by mechanically moving the waveguide in detail.

In Chapter 4, a beam-switching planar H-S lens antenna concept achieved by switch is proposed and explored to solve the drawbacks of mechanical beam scanning in Chapter 3. This solution will be verified by both simulations and outdoor measurements. Particularly, the effects on beam-steering angle caused by coma aberration will be explained in detail.

In Chapter 5, the surface high-resolution focusing of proposed hyperbolic secant lens is utilized for the single-pixel scanning near-field microwave imaging. numerical simulations and spatial resolution imaging experiment is carried out to demonstrate the validity of designed lens porotype.

In Chapter 6, finally general conclusions and perspectives are drawn at the end of the thesis.

<center>**CHAPTER 2**</center>

<center>**Design Theory and Fabrication Methods**</center>

2.1 Ray-transfer matrix analysis of hyperbolic secant lens

The 2-by-2 ray transfer matrix analysis is also known as ABCD matrix analysis [51, 52], which is a type of ray tracing method commonly used in describing the ray propagation in the optical system, as shown in Figure 2-1. The ray transfer matrix is a characteristic of each optical element. Specifically, under the paraxial approximation, the ray behavior can be described by its distance (r) from the optical axis and by the slope (s) in any plane perpendicular to optical axis.
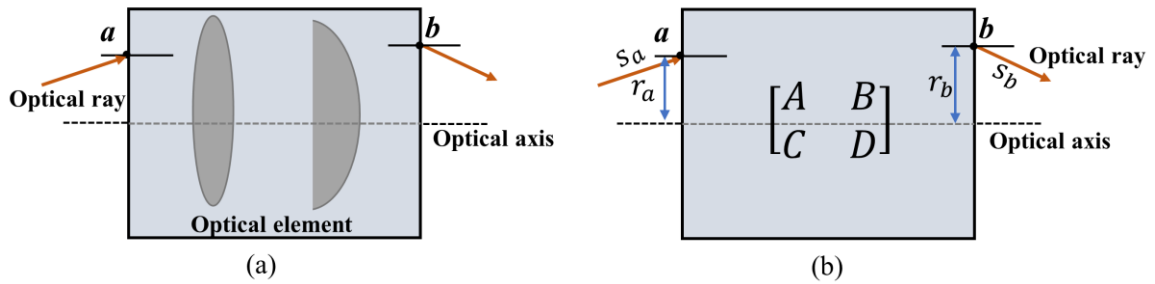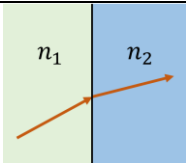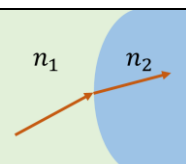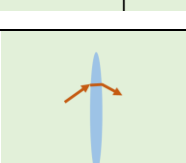
Figure 2-1 The 2-by-2 ray transfer (ABCD) matrix analysis for the optical system.

The commonly used ray transfer matrices for simple optical elements can be found in classical optical textbook, which are shown in the Table 2-1 [53]. In addition, the ray transfer matrix analysis is also a very useful tool to deal with the propagation in GRIN lens. Here, a self-focusing cylindrical GRIN lens structure has not been exhaustively reported in the literature of micro- and millimeter wave applications, thereafter known as hyperbolic secant (H-S) lens [54, 55]. It has unique characteristics that the rays oscillate in a sinusoidal way along the optical axis as shown in Figure 2-2. The oscillation period of the rays inside H-S lens is defined as pitch (p). Various characteristics of the rays such as focusing, diverging and collimation can be realized by

<center>34</center>

choosing different pitches. If p < 0.25, the parallel incident rays still can be focused, in which case the focal point appears at the outside of lens.

Table 2-1 The commonly used ray transfer matrices for simple optical elements [53]

	$\begin{bmatrix} 1 & d \\ 0 & 1 \end{bmatrix}$	Propagation in free space with distance of d.
n_1 n_2	$\begin{bmatrix} 1 & 0 \\ 0 & n_1/n_2 \end{bmatrix}$	Refraction at a planar interface.
n_1 n_2	$\begin{bmatrix} 1 & 0 \\ \dfrac{n_1-n_2}{R\cdot n_2} & \dfrac{n_1}{n_2} \end{bmatrix}$	Refraction at a curved interface. R is the radius of curvature.
	$\begin{bmatrix} 1 & 0 \\ 0 & 1 \end{bmatrix}$	Reflection from a planar mirror.
	$\begin{bmatrix} 1 & 0 \\ -\dfrac{1}{f} & 1 \end{bmatrix}$	Propagation through thin lens with focal length $f > 0$ for convex.
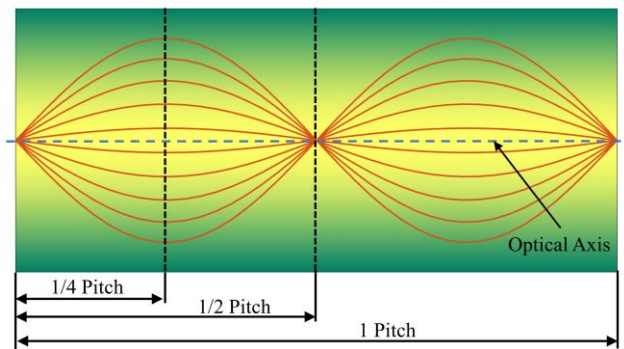
Figure 2-2 The unique self-focusing properties of the H-S lens. The solid orange curve represents the trajectory of the rays.

This unique characteristic provides a potential way to design integrated lens antennas and off-body fed lens antenna by simply adjusting the pitch and thickness of H-S lens.

The ray behavior inside H-S lens can be also explained by Ray equation. This ray equation can be obtained from the expression of a differential arc length along a ray within lens. The transverse refractive index profile of H-S lens is defined by the following equation [50]

$$n(x) = n_0 \text{sech}(\alpha x) \tag{2-1}$$

where n_0 is the central refractive index along the z-axis. $\alpha = 2\pi p / w$ is a gradient parameter. w is the thickness of lens. Figure 2-3 (a) illustrates the ray trajectory through the H-S lens.
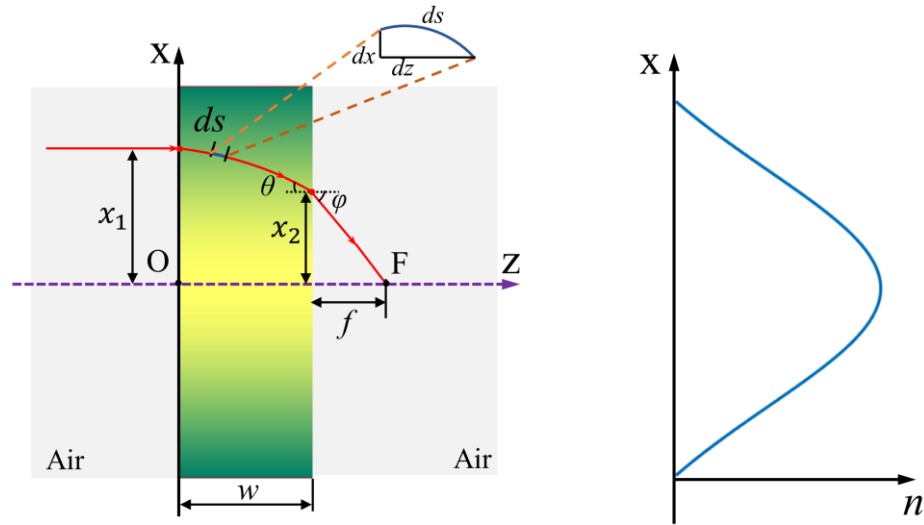
Figure 2-3 The schematic view of ray trajectory through the H-S lens. (Right). Hyperbolic secant distribution of the refractive index (n) profile.

The differential arc length can be mathematically expressed by the following equation.

$$ds = \sqrt{(dx)^2 + (dz)^2} \tag{2-2}$$

Here, we can define $\dot{x} = dx / dz$, then

$$ds = \sqrt{1 + (\dot{x})^2} \, dz \tag{2-3}$$

According to [56], the third optical direction cosine is invariant along any ray within lens, and defined as follows:

$$l_0 = n(x)\frac{dz}{ds} = \frac{n(x)}{\sqrt{1+(\dot{x})^2}}$$

(2-4)

Eq. (2-4) can be written as

$$dz = \frac{l_0}{\sqrt{n(x)^2 - l_0^2}} dx$$

(2-5)

Then, we can get the initial ray trajectory between any two points by substituting (2-1) into (2-5) and performing the integration with respect to x

$$z = \int_{x_0}^{x} \frac{l_0}{\sqrt{n(x)^2 - l_0^2}} dx = \int_{x_0}^{x} \frac{\cosh(\alpha x)}{\sqrt{A^2 - \sinh^2(\alpha x)}} dx$$

(2-6)

where A is a constant value and equals to $\sqrt{(n_0^2 - l_0^2)/l_0^2}$.

Here, in order to solve Eq. (2-6), we use a transformation of the variables as defined below

$$u = \sinh(\alpha x)$$

(2-7)

Under this transformation, the ray trajectory between any two points within the H-S lens becomes

$$z = \frac{1}{\alpha}\int_{u_0}^{u} \frac{1}{\sqrt{A^2 - u^2}} dx$$

$$= \frac{1}{\alpha}\left(\sin^{-1}\left(\frac{u}{A}\right) - \sin^{-1}\left(\frac{u_0}{A}\right) \right)$$

(2-8)

where u_0 is the value of u at $z=0$,that is $u_0 = \sinh(\alpha x_0)$.

Eq. (2-8) can be written as

$$\alpha z + \sin^{-1}\left(\frac{u_0}{A}\right) = \sin^{-1}\left(\frac{u}{A}\right)$$

(2-9)

Here, we can define $\tau = \alpha z + \sin^{-1}(u_0 / A)$, then

$$u(z) = A\sin(\tau) \tag{2-10}$$

Eq. (2-10) indicates the ray position at each point within the H-S lens. The ray slope in the new u-z coordinate system can be calculated as follows:

$$\dot{u}(z) = A\cos(\tau)\dot{\tau}(z)$$
$$= A\cos(\tau)\left(\alpha z + \sin^{-1}(u_0 / A)\right)' = A\alpha\cos(\tau) \tag{2-11}$$

After constituting the parameter to (10) and (11), and performing trigonometric manipulation, we can get the ray position and slope respectively.

The ray position:

$$u(z) = A\cos\left(\sin^{-1}(u_0 / A)\right)\sin(\alpha z) + u_0\cos(\alpha z) \tag{2-12}$$

The ray slope:

$$\dot{u}(z) = A\alpha\left(\cos\alpha z \cdot \cos\left(\sin^{-1}(u_0 / A)\right) - (u_0 / A)\sin(\alpha z)\right) \tag{2-13}$$

But

$$\cos\left(\sin^{-1}(u_0 / A)\right) = \cos(\tau_0) = \dot{u}_0 / (\alpha A) \tag{2-14}$$

where u_0 and τ_0 are the values of u and τ at $z = 0$, respectively.

Then, substituting (2-14) into (2-12) and (2-13) respectively,

$$u(z) = u_0\cos(\alpha z) + \dot{u}_0 \frac{\sin(\alpha z)}{\alpha} \tag{2-15}$$

$$\dot{u}(z) = -u_0\alpha\sin(\alpha z) + \dot{u}_0\cos(\alpha z) \tag{2-16}$$

we can obtain 2-by-2 ray transfer matrices to describe ray propagation in H-S lens,

$$\begin{pmatrix} u(z) \\ \dot{u}(z) \end{pmatrix} = \begin{pmatrix} \cos(\alpha z) & \dfrac{\sin(\alpha z)}{\alpha} \\ -\alpha\sin(\alpha z) & \cos(\alpha z) \end{pmatrix} \begin{pmatrix} u_0 \\ \dot{u}_0 \end{pmatrix} \tag{2-17}$$

After propagating through the H-S lens, the ray refracts obeying Snell's law and enters the free space as shown in Figure 2-3 (a). The refracted rays finally intersect at a point. The distance between that point and rear surface of the H-S lens is defined as the back focal length f.

In order to calculate f, the Snell's law is applied at the rear surface of the H-S lens.

$$n(x_2)\sin\theta = n_{air}\sin\varphi \qquad (2\text{-}18)$$

where $n(x_2) = n_0\mathrm{sech}(\alpha x_2)$ and $n_{air} = 1$.

Here, the ray incident on H-S lens parallel to its optical axis (z-axis).
$\theta = \tan^{-1}\left[\dot{u}(w)\right]$, then Eq. (2-18) can be written as follows

$$n_0\mathrm{sech}(\alpha x_2)\sin\left\{\tan^{-1}\left[\dot{u}(w)\right]\right\} = \sin\varphi \qquad (2\text{-}19)$$

That also means

$$\varphi = \sin^{-1}\left(n_0\mathrm{sech}(\alpha x_2)\dot{u}(w)/\sqrt{\dot{u}(w)^2 + 1}\right) \qquad (2\text{-}20)$$

From Figure 2-3 (a), the tangent of refracted angle can be determined as follows

$$\tan\varphi = \frac{x_2}{f} \qquad (2\text{-}21)$$

Combine (18), (19), (20) and (21) gives

$$f = \frac{x_2}{\tan\left\{\sin^{-1}\left[n_0\mathrm{sech}(\alpha x_2)\dot{u}(w)/\sqrt{\dot{u}(w)^2 + 1}\right]\right\}} \qquad (2\text{-}22)$$

According to the equation $\sin(\arctan(\upsilon)) = \upsilon/\sqrt{\upsilon^2 + 1}$, Eq. (2-22) can be also written as

$$f = \frac{x_2}{\tan\left\{\sin^{-1}\left[n_0\mathrm{sech}(\alpha x_2)\sin\left(\tan^{-1}\left[\dot{u}(w)\right]\right)\right]\right\}} \qquad (2\text{-}23)$$

Under the paraxial approximation [57], that is $\theta \approx \tan\theta \approx \sin\theta$, the (2-23) can be further simplified as follows,

$$f = \frac{x_2}{n_0\mathrm{sech}(\alpha x_2)\sin\left(\tan^{-1}\left[\dot{u}(w)\right]\right)} = \frac{x_2}{n_0\dot{u}(w)} \qquad (2\text{-}24)$$

Combine (15), (16) and (24) gives

$$f = \frac{x_1 \cos(\alpha w)}{n_0 \cdot \left| -x_1 \alpha \sin(\alpha w) \right|} = \frac{w}{2\pi p n_0} \cot(2\pi p) \qquad (2\text{-}25)$$

Eq. (25) provides a flexible and extensible dimension constraint for deigning H-S lens ($n_0 = 1.673$) as illustrated in Fig.2-3. The pitch is easily tunable to get suitable lens width and back focal length. In a particular case, if pitch $p = 0.25$, the back focal length is equal to zero that means the focal point appears at the rear surface of the H-S lens as mentioned above.
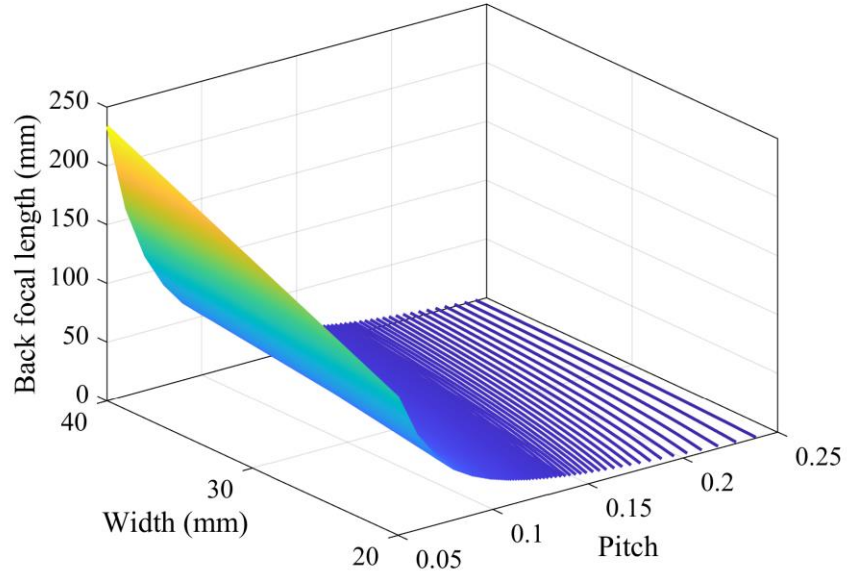
Figure 2-4 3D contour for dimension constraints of H-S Lens design.

The flow chart for different H-S lens types design is given below. The four most critical parameters (lens pitch, diameter, focal length and thickness) need to be first determined according to Eq.2-25 and design requirements. Then, the corresponding refractive index profile of desired lens type according to Eq.2-1 can be obtained. In the following section, the discretization and realization of the corresponding refractive index profile is discussed in detail.

```
                    ┌─────────────────────────────────┐
                    │   Select the desired H-S lens type │
                    └─────────────────────────────────┘
                                    │
              ┌─────────────────────┴─────────────────────┐
              ▼                                             ▼
    ┌──────────────────────┐                    ┌──────────────────────┐
    │ Integrated lens antenna │                    │ Off-body fed lens antenna │
    └──────────────────────┘                    └──────────────────────┘
              │                                             │
              ▼                  NO                         ▼
        ◇ Imaging application? ◇──────────┐   ┌────────────────────────────┐
                                          │   │ Determine the appropriate lens │
           YES                            │   │ size (focal length, diameter and │
              │                           ▼   │ thickness) according to design │
              ▼                   ┌──────────┐│ requirements                  │
    ┌──────────────────┐         │Lens pitch │└────────────────────────────┘
    │ Lens pitch p = 0.5 │         │ p = 0.25  │              │
    └──────────────────┘         └──────────┘              ▼
              │                        │        ┌──────────────────────────┐
              └──────────┬─────────────┘        │ Select a suitable lens pitch │
                         ▼                       │ according to Eq.2-25.       │
         ┌────────────────────────────┐         └──────────────────────────┘
         │ Determine the appropriate lens │                  │
         │ size (focal length, diameter and │                │
         │ thickness) according to Eq.2-25 │                  │
         │ and design requirements        │                  │
         └────────────────────────────┘                     │
                         │                                    │
                         └──────────────┬────────────────────┘
                                        ▼
                         ┌────────────────────────────┐
                         │ Obtain the corresponding      │
                         │ refractive index profile of   │
                         │ desired lens according to Eq.2-1 │
                         └────────────────────────────┘
                                        │
                                        ▼
                         ┌────────────────────────────┐
                         │ Discrete the lens profile and │
                         │ fabricate lens                │
                         └────────────────────────────┘
```

2.2 Fabrication of H-S lens profile with perforated and infill structure

There are various manufacturing technologies such as foam pressing, PCB milling and metamaterials with metallic resonant structures to fabricate GRIN lens. However, compared to the 3-D printing, these manufacturing techniques need complicated and expensive special fabrication process. Here, based on easily accessible 3-D printing, two fabrication processes using the internal perforation structure of various air-hole sizes and different infill ratios of material is utilized to achieve intended refractive index profile of H-S lens, respectively. Polylactic acid (PLA) plastic material is one of the most commonly used materials for 3D printing, which has a relative dielectric constant $\varepsilon_m \approx 2.75$, and loss tangent $\tan\delta \approx 0.015$ at 10 GHz [58].

The perforation structure, traditionally, is achieved by drilling holes of various sizes in a dielectric material or additive manufacturing. The unit-cell element is a cube with circular air-hole, as shown in Figure 2-5. In our case, the size of unit-cell element is a = 7 mm, and P is the radius of circular air-hole. The unit-cell element can be easily and economically fabricated by using the additive manufacturing or 3D-printing.
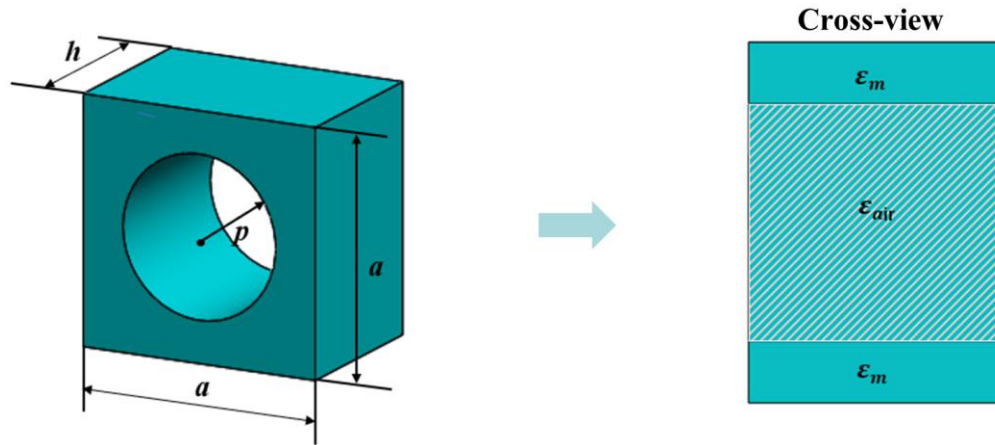
Figure 2-5 The unit-cell element of the perforation structure.

Based on the effective medium theory, the equivalent effective relative permittivity (ε_e) of the unit-cell element can be controlled by changing the diameter of air-hole. Therefore, under the condition that the wave vector is perpendicular to the axis of air hole, ε_e can be calculated using the following expression [59].

$$\varepsilon_e = \frac{\left(a^2 - \pi P^2\right)\varepsilon_m + \pi P^2 \varepsilon_{air}}{a^2} \tag{2-26}$$

where ε_{air} stands for the air permittivity. ε_m is the material permittivity.

For the special case that the whole region of the unit-cell element is occupied with air ($a = 2P$), the lowest achievable effective relative permittivity by using circular air-hole is 1.39. The effective permittivity of unit-cell element with different hole size for PLA plastic materials is shown in Figure 2-6.
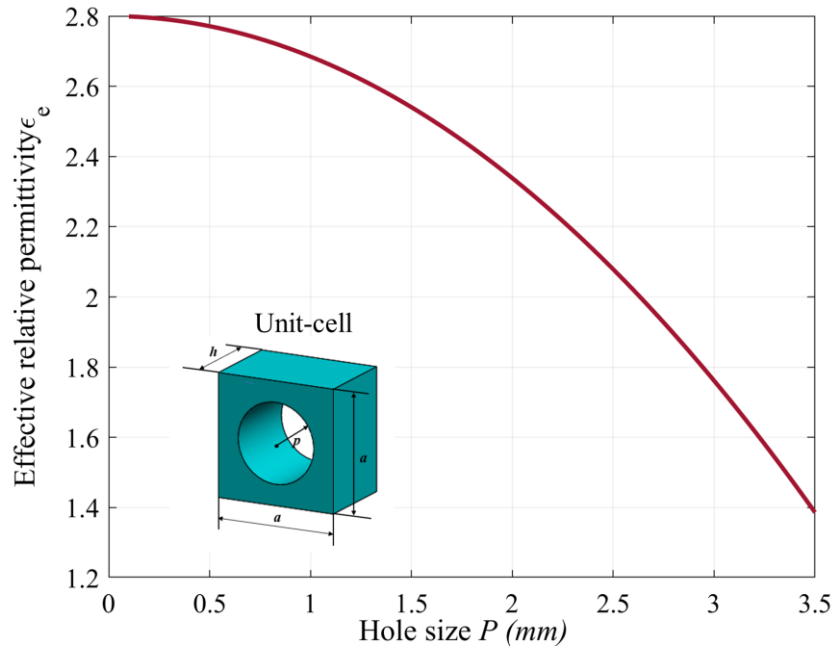
Figure 2-6 Illustration of effective permittivity of unit-cell element with different hole size for PLA plastic materials.

However, considering the practical dimensional accuracy of the FDM (fused deposition modeling) 3D printer, the air-hole structure cannot be fabricated in infinitely small size, which limits its imaging application in the high frequency. However, by controlling the infill ratio of PLA (PLA volume percentages) as shown in Figure 2-7, the functionality of the proposed lens concept can be easily expanded to higher frequency bands such as millimeter wave.
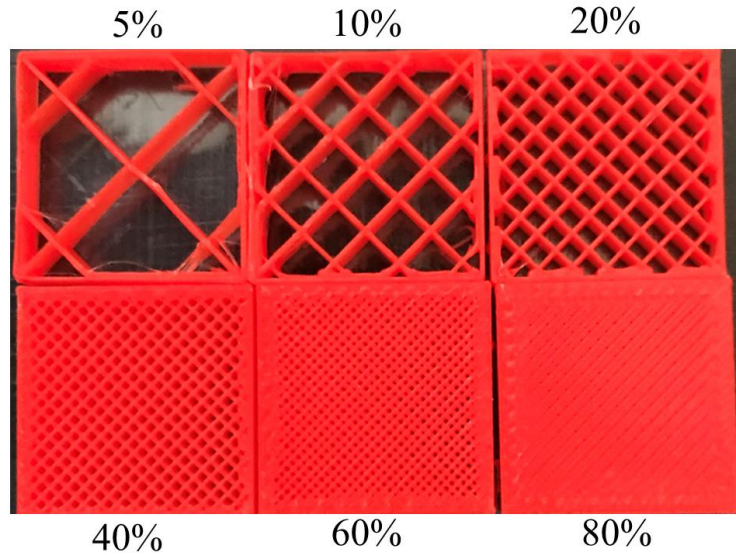
Figure 2-7 Different infill ratio for PLA plastic materials.

According to Ref [60, 61], the relationship between the effective permittivity (ε_e) and infill ratio (v_{ir}) is approximately linear, which can be determined by the following equation

$$\varepsilon_e = 1 + v_{ir}(\varepsilon_m - 1) \tag{2-26}$$

2.3 Lens feeding structure design

Common requirements for a feed source of lens are low back-to-front radiation ratio, minimum spillover losses, well-defined phase center coincident with the focal point and effective illumination. Conventionally, patch antenna, slot antenna, horn antenna and waveguide are commonly utilized as feed sources. Unlike the case of resonant metamaterials lens that are inherently narrowband, the intrinsic broadband response of dielectric lens is usually limited by the bandwidth of the feed source [62]. In our case, to realize the broadband lens antenna, a printed antipodal fermi antenna (APFA) with corrugation structure [63] is designed with advantages of broad bandwidth, high gain, and lightweight. The schematic of APFA structure is shown in Figure 2-8. One pair of antipodal Femi-Dirac type tapered slot is etched on the on both sides of dielectric

44

substrate with a relative permittivity of 3.3, loss tangent 0.001 and a thickness of 0.8 mm. The curve of Femi-Dirac type tapered slot is determined by.

$$f_{APFA}(z) = \frac{-a_s}{1+e^{-b(z-c)}} \tag{2-27}$$

where a_s is the asymptotic value of the width of the taper for $x \to \infty$. b is related to the gradient at inflection point. c denotes the position of inflection point of Fermi-Dirac function.
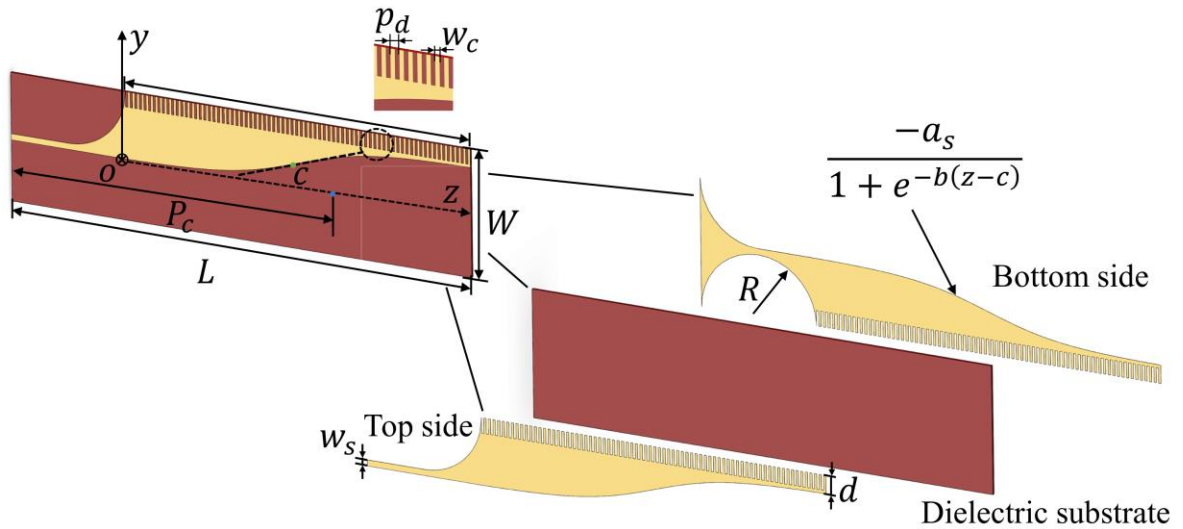
Figure 2-8 The schematic of APFA structure at 10 GHz. One pair of antipodal Femi-Dirac type tapered slot is etched on the on both sides of dielectric substrate.

In our case, the specific design parameters of APFA are listed in Table 2-2. The typical characteristic of APFA is the rectangular corrugations on the lateral side of the substrate, which can enlarge the effective aperture and guarantee the same phase inside and outside the tapered slot. And for that, this corrugation structure is very useful to reduce the side lobe levels and increase the gain.

Table 2-2 Geometry dimensions of APFA structure

Dimensions	Values
L	160 mm
W	42 mm
P_c	110 mm
R	20 mm
d	6 mm
ws	2 mm
p_d	1.6 mm
wc	0.8 mm
a_s	15
b	0.08
c	60

The performance characteristics of the APFA are shown in Figure 2-9. The E-plane and H-plane is defined as y-z and x-z plane, respectively. Figure 2-9(a)-(b) illustrates the simulated and measured normalized radiation patterns for the APFA, for both E-plane and H-plane. Good agreement between simulated and measured radiation patterns (Co-Pol radiation) was obtained with a peak realized gain of 14.2 dBi. Besides, the side lobe level (SLL) is lower than ~17 dB for both E-plane and H-plane. The measured reflection coefficient S11 of the APFA are shown in Fig.2-9(c). It can be observed that the measured S11 are almost less than -10 dB from 8.2 GHz to 12.5 GHz. Fig.2-9(d) shows there are some differences between measurement and simulated results about 1-2 dB in the frequency region of 8.2-12.5 GHz. The phase center is an approximate point in space that need to be coincident with the lens focal point to minimize phase error over aperture. Here, the approximate phase center location of APFA is at P=110 mm with frequency 10 GHz.
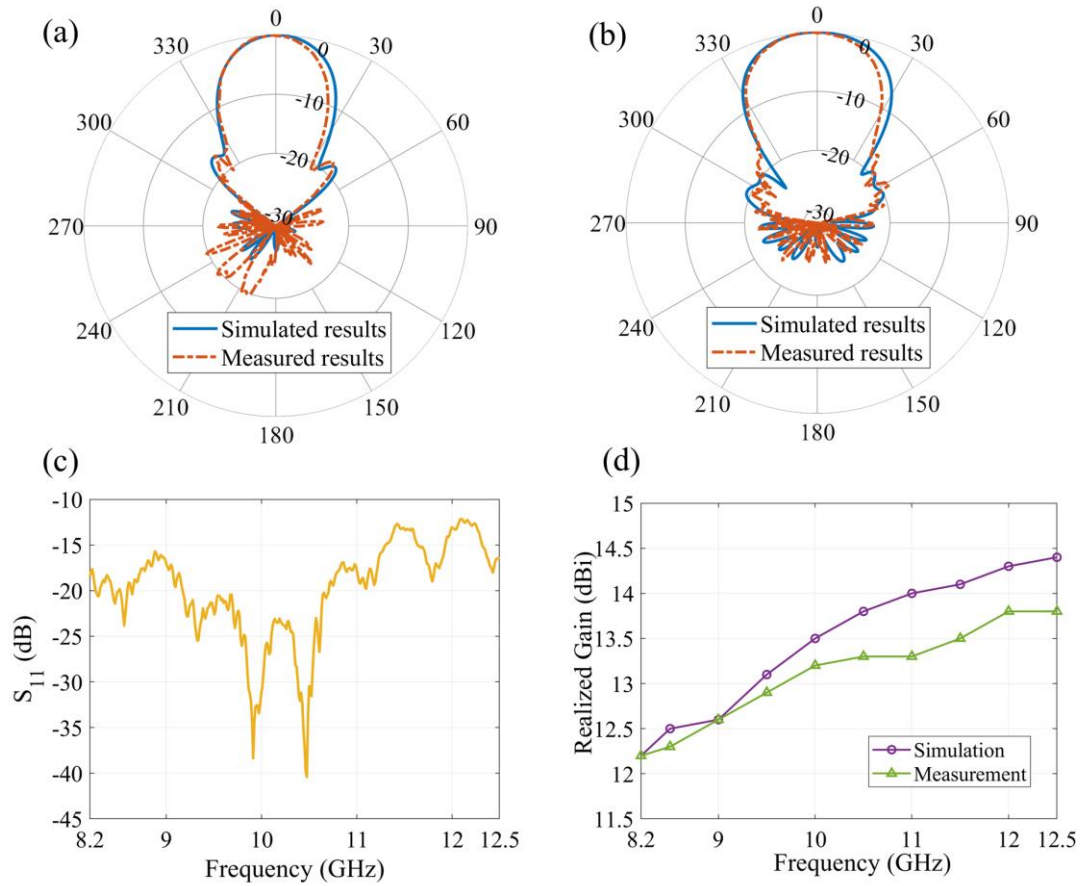
Figure 2-9 APFA performance. (a), (b) Measured and simulated E- and H-plane normalized radiation patterns at 10GHz, unit: dB. (c) Measured reflection coefficient S11 of APFA. (d) Measured and simulated Realized gain.

2.4   Summary

In this chapter, the design theory and analysis methods based on 2-by-2 ray matrix transfer for proposed hyperbolic secant (H-S) lens was discussed and explained in detail. Moreover, the fabrication methods by using perforated and infill structure for 3-D printing was introduced, which provide a simple and economical way to fabricate H-S lens compared with other manufacturing technologies such as foam pressing, PCB milling and metamaterials with metallic resonant.

Besides, in order to realize the broadband lens antenna, a printed antipodal fermi antenna (APFA) with corrugation structure operating at X-band with advantages of broad

bandwidth, high gain, and lightweight was verified by full-wave simulation and experiment.

CHAPTER 3

High-gain, Broadband Hyperbolic Secant (H-S) Lens Antenna and 2-D Beam-scanning Applications

3.1 Realization of H-S lens profile with perforated structure

The implemented design procedure of 3-D H-S lens designed to operate at 10 GHz is shown in Figure 3-1. Here, the pitch, diameter, thick and back focal length of designed H-S lens is 0.05, 189mm, 35mm and 204.9 mm respectively. The continuous relative permittivity profile of H-S lens as shown in Figure 3-1 need to be discretized into different layers (27 layers) by staircase approximation. Figure 3-1(b), (c) illustrates the achieved 2-D continuous and discrete relative permittivity distribution respectively. The different sizes of perforation are utilized to obtain the discrete relative permittivity distribution as shown in Figure 3-1(d). Table 3-1 lists the specific designed perforation sizes with each layer. Noted that only half of layer is shown owing to the axial symmetry of relative permittivity distribution of H-S lens.
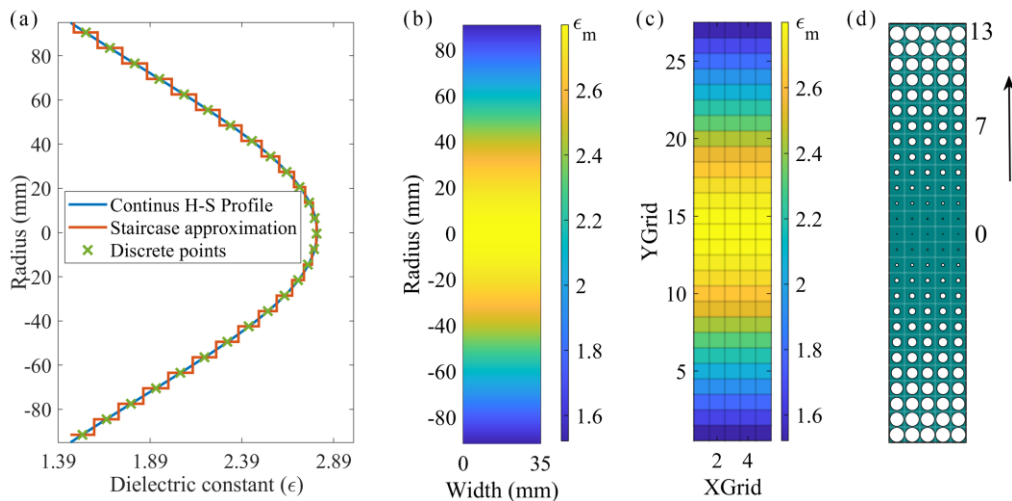
Figure 3-1 The implemented design procedure of 3-D H-S lens designed to operate at 10 GHz. (a) Staircase approximation of continuous relative permittivity profile of H-S lens. (b) Continuous 2-

D relative permittivity distribution. (c) Discrete 2-D relative permittivity distribution. (c) Discrete 2-D relative permittivity profile. (d) Perforated dielectric structure of H-S lens.

Table 3-1 Designed perforation sizes with each layer

Layer	Diameter (mm)
0	0.316
1	0.653
2	1.226
3	1.816
4	2.399
5	2.968
6	3.517
7	4.042
8	4.542
9	5.013
10	5.456
11	5.870
12	6.253
13	6.608

In order to create the 3-D H-S lens, the discrete 2-D distribution need to be rotated around the central axis. Here, the cross-section of 3-D H-S lens model by rotating operation is shown in Figure 3-2, which has circular geometry with the diameter of 189 mm and the thickness of 35mm. The designed back focal length is 204.9mm, and the back focal length to lens diameter ratio (f/D) is 1.08.
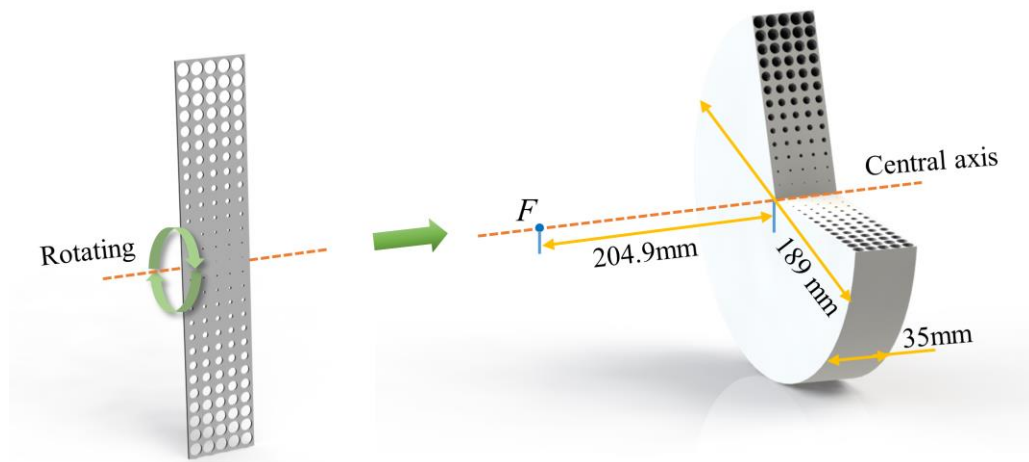
Figure 3-2 Schematic of the cross-section of designed 3-D H-S lens model by rotating operation.

3.2 Focusing performance analysis

To illustrate the H-S lens operation performance, a ray-tracing algorithm based on above-mentioned ray transfer matrices is applied to this relative permittivity distribution, launching rays from focal point that becomes parallel to the central axis, as shown in Figure 3-3(c). The vertical dot line represents the focal plane. Besides, based on the electromagnetic field full-wave simulation, the 2-D electric field distribution, propagating through the lens is presented in Figure 3-3(a) for WR-90 waveguide is placed at the focal point of H-S lens as a feed source.

As expected, very good focusing properties are achieved that H-S lens can be a good phase transformer to convert a spherical wave into a plane wave. Figure 3-3(b), (d) illustrates the aperture phase and magnitude distribution at a plane which is located at the exit aperture of the H-S lens respectively. The phase uniformity across the actual physical aperture of the H-S lens is another evidence of the transformation of the spherical wave into plane wave. The magnitude of the E-field at the center of H-S lens is larger than that at the edge. The dot white and black circle represents the actual physical aperture of H-S lens (0.189 m). It should be noted that the feed source does not need to be located at the surface of the lens, unlike the case of the typical H-S lens. Obviously, the results of these

51

two approaches are in reasonable agreement, which indicates that the ray tracing method can be quite accurate for the analysis of H-S lenses.
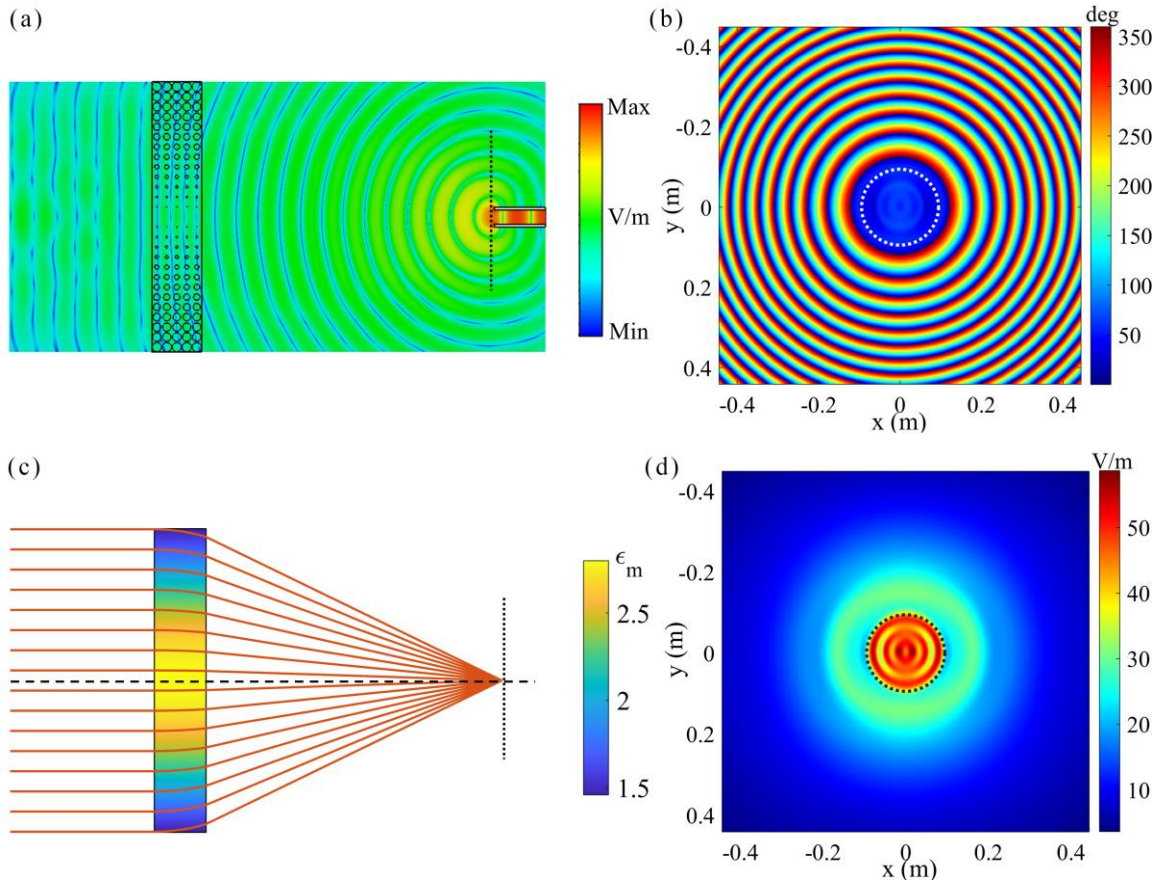
Figure 3-3 Focusing performances of proposed H-S lens. (a) Simulated 2-D electric field distribution with WR-90 waveguide as source feed, and (b) The aperture phase distribution. (c). Ray tracing across the H-S lens. The vertical dot line is the focal plane. (d) The aperture amplitude distribution. Noted that the dot white and black circle represents the actual physical aperture (0.189m diameter) of H-S lens.

3.3 Modeling and simulation results

To validate the design, the proposed 3-D H-S lens antenna model is constructed and simulated using the electromagnetic field full-wave simulation in CST Microwave Studio. Figure 3-4 illustrates the schematic 3D view of the designed H-S lens antenna system. It consists of three main parts, the H-S lens, its feeding source (APFA) and the supporting foam. It is noted that the phase center of APFA varies based on the frequency. There is some variation (10~20mm) in approximate phase center location from 8.2 GHz

to 12.5 GHz. The phase center should be located at the focal point of H-S lens to obtain an optimum coupling. As mentioned above, the approximate phase center location is at P_c = 110mm with frequency 10GHz. So, the approximate distance (S) between APFA and H-S lens is 154.92 mm, which gives a −10 dB edge taper at the angle of 24.7 degree.
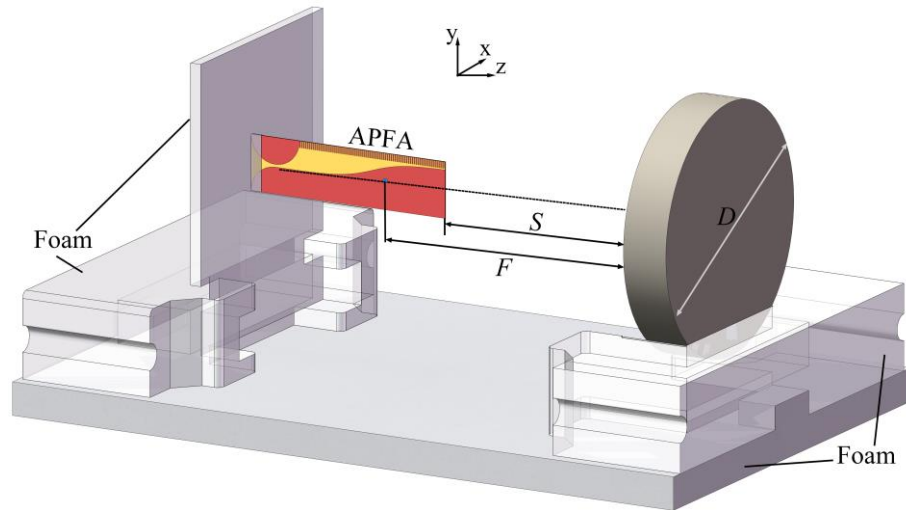
Figure 3-4 3-D perspective view of proposed H-S lens antenna system at 10GHz composed of feeding source (APFA), H-S lens and the supporting foam.

Figure 3-5(a), (b) illustrates the simulated radiation patterns for both Co- and Cross-polar in the E- and H-plane at 10 GHz respectively. The simulated realized gain of the H-S lens antenna is 24.7 dBi, which is 10.5 dBi higher than the feeding source of APFA itself. It also verifies that the excellent focusing feature of the H-S lens that effectively convert a spherical wave emitted by the feeding source to the approximate plane wave. Thus, the high realized gain is achieved owing to the phase delay introduced by the dielectric perforation structure. Meanwhile, the cross-polar radiation patterns of both E- and H-plane show the cross-polarization level is very low, and is less than 25dB. Figure 3-5(c) shows the simulated realized gain and the side lobe levels for different frequencies. The ~3-dB fractional realized gain bandwidth is 43.9% from 8 to 12.5 GHz, indicating the intrinsic broadband response of H-S lens. The side lobe levels remain lower than -14 dB across the frequency band of 8-12.5 GHz. To further assess the focusing feature of the lens, the aperture phase distribution at a plane which is located at

the exit aperture of the H-S lens is respectively given in Figure 3-5(d). As expected, the phase is uniform across the exit aperture plane of the H-S lens, which further demonstrate the high realized gain owing to the phase transformation function (spherical wave to plane wave) of the H-S lens.
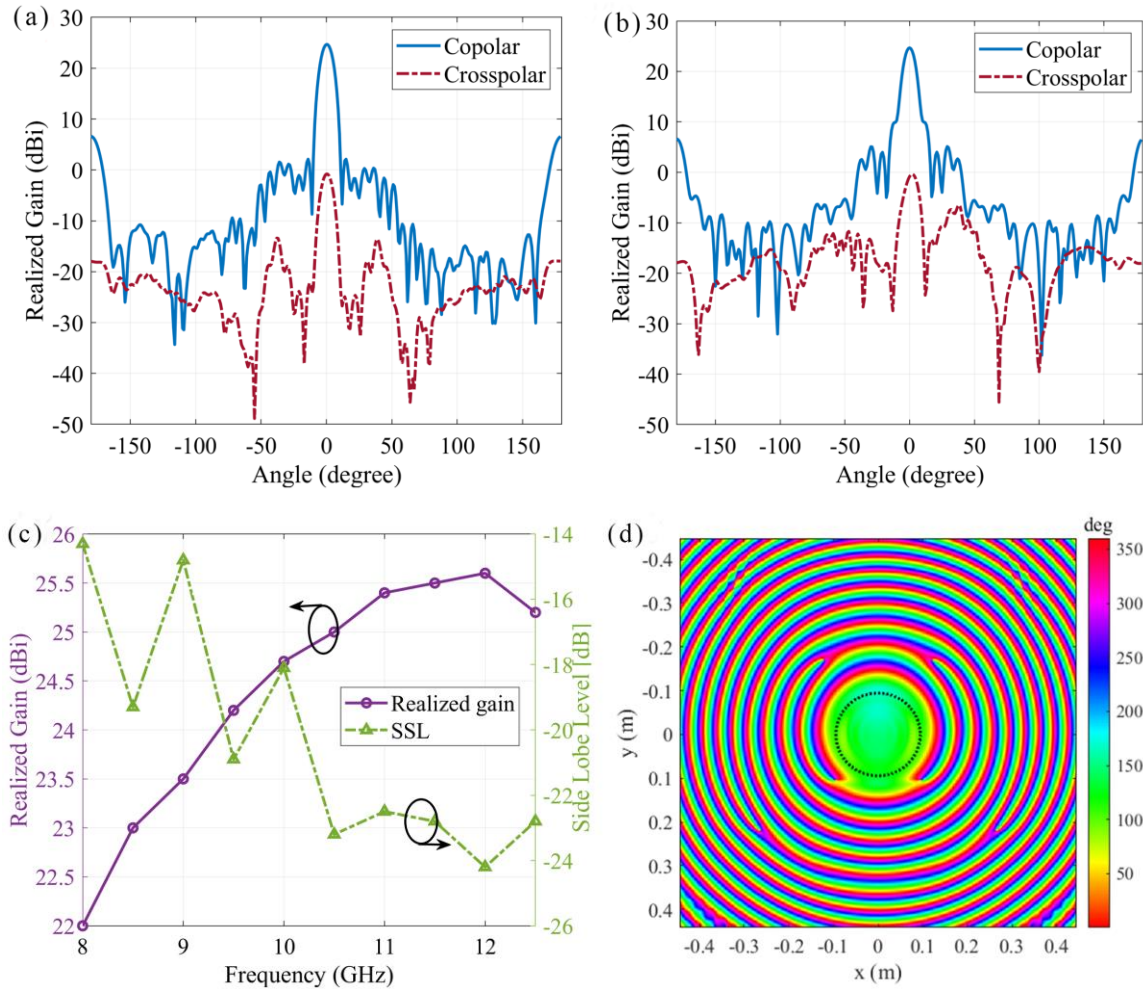
Figure 3-5 3-D Simulated co- and cross-polar radiation patterns in E-plane and H-plane respectively at 10GHz. (a) E-plane. (b) H-plane. (c) Realized gain and Side lobe level. (d) The aperture phase distribution at a plane which is located at the exit aperture of the H-S lens. Noted that the black dot circle represents the actual physical aperture (0.189m diameter) of H-S lens.

3.4 Prototype fabrication

The 3-D printed planar H-S lens is built based on the fused deposition modeling (FDM) that is an additive manufacturing process. In FDM 3-D printer, the H-S lens

model is constructed layer by layer by heating and extruding thermoplastic polymers in a filament form in a pre-determined path. Figure 3-6 shows the fabricated prototype of the proposed dielectric H-S lens, which is obtained by polylactic acid (PLA) plastic material.

In our case, the dimensional accuracy of the FDM 3D printer is quite limited, which requires the minimum wall thickness of ~0.8mm. In order to prevent printed lens models from falling apart, we add the very thin supporting layer structures around the lens. It should be noted that the actual overall dimensions of the designed H-S lens are $191 \times 191 \times 36$ mm, which is slightly larger than simulated one.
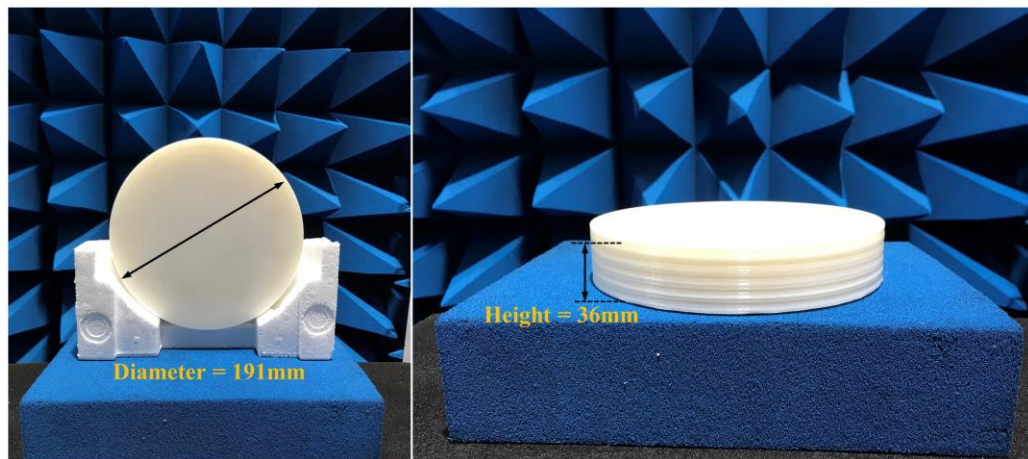
Figure 3-6 Photograph of the fabricated prototype of the proposed H-S lens of 191 mm diameter and 36mm height.

3.5 Experimental results and discussion

Here, a low-loss and lightweight foam-based structure is designed to support the H-S lens and APFA. Although an approximation distance between H-S lens and APFA has been given in section 3.1, it still needs to be adjusted to obtain the optimal value. The whole of the H-S lens antenna is used as the transmitting antenna and is placed on a rotating platform, as shown in Figure 3-7. The measurement process is performed inside a far-field anechoic chamber using the gain transfer method and the Flann standard gain horn at X-band (Model 16240-20). Both the H-S lens antenna and horn antenna is connected to the Anritsu MS46322B vector network analyzer. By using the control

application under LabVIEW environment, automatic measurements are carried out to characterize the H-S lens antenna performance from 8.2 to 12.5 GHz.
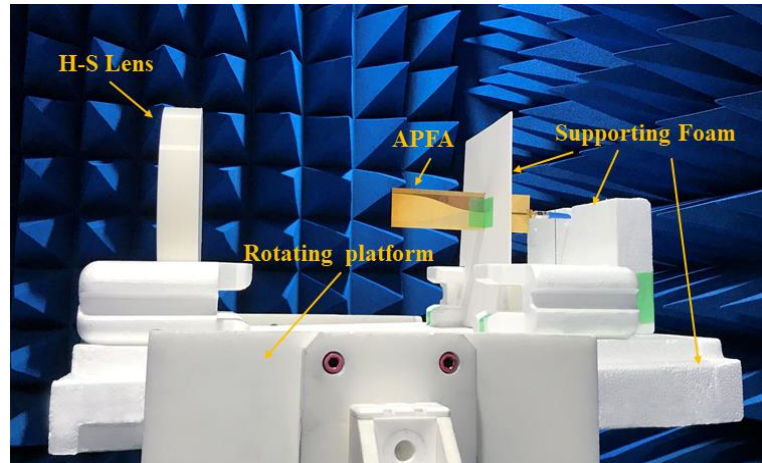
Figure 3-7 Photograph of lens measurement setup in anechoic chamber.

Figure 3-8 illustrates the simulated and measured radiation patterns for both the Co-Pol and Cr-Pol in E-plane and H-plane respectively at 10GHz. In general, there is a good consistency between the simulation and measurement results in terms of realized gain, side lobe levels and 3-dB beamwidth as shown in Table 3-2, which validates the discretization process of H-S lens. The measured sidelobe levels are −17.4 and −16.7 dB, and the 3-dB beamwidths are the same (9 degree) for the E-plane and H-plane, respectively. Furthermore, the measured cross-polar levels of both E- and H-plane still remains at a low level (<-21 dB).
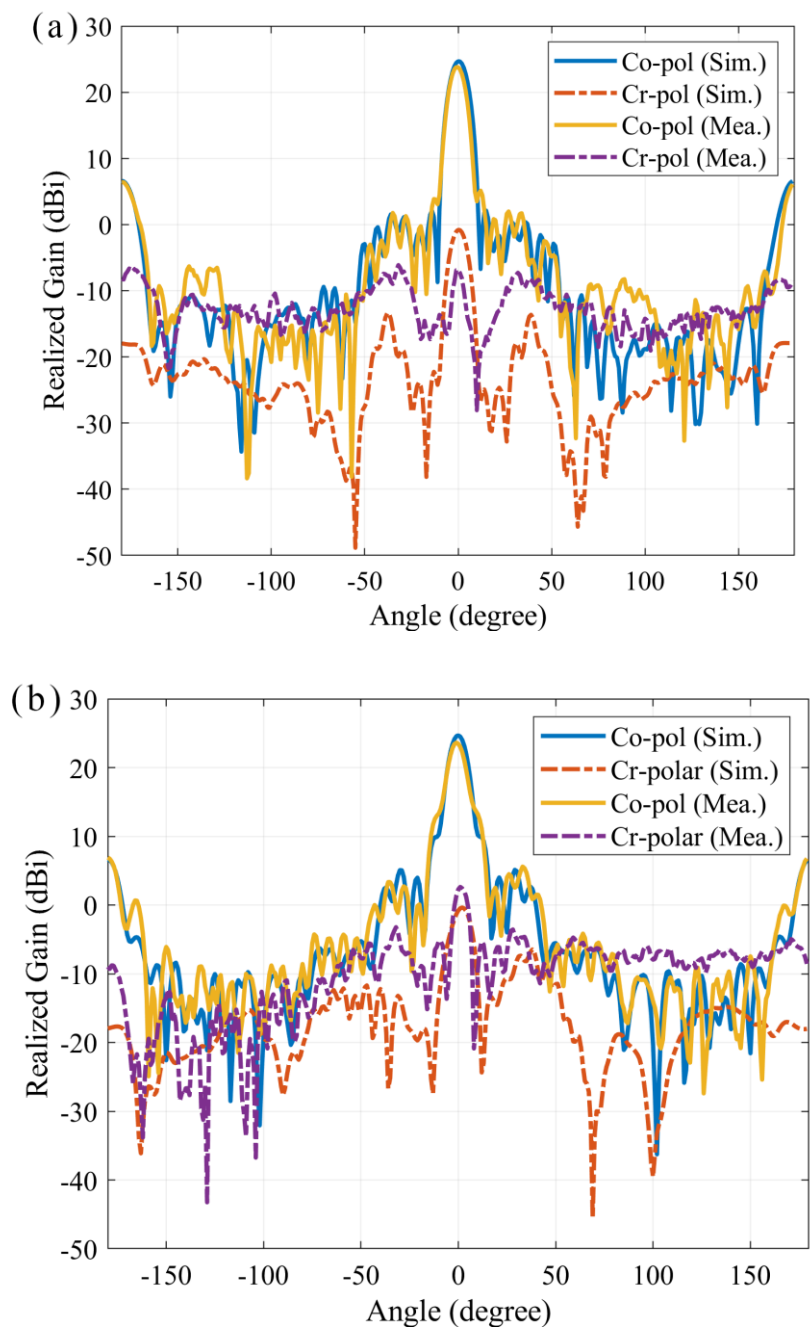
Figure 3-8 Simulated and measured radiation patterns of the proposed H-S lens antenna at 10 GHz. (a) E-plane. (b) H-plane.

Owing to the accuracy of additive manufacturing and the limit of antenna measurement condition, there are also some differences between the simulated and measured results as shown in Figure 3-8.

Table 3-2 Simulated and Measured Radiation Patterns Characteristic of H-S Lens at 10 GHz

		Simulated	Measured
Realized Gain (dBi)		24.7	23.8
3-dB Beamwidth (º)	E-plane	9.2	9
	H-plane	8.7	9
Cr-pol Levels (dB)	E-plane	-25.5	-29.7
	H-plane	-25.1	-21.0
Side Lobe Levels (dB)	E-plane	-18.1	-17.4
	H-plane	-18.0	-16.7

Another important parameter that measures the lens performance is the total radiation efficiency which is defined as follows:

$$\eta = \eta_{ape} \cdot \eta_{rad} \tag{3-1}$$

where $\eta_{ape} = D_a \lambda^2 / (4\pi A)$ is the aperture efficiency, D_a is the directivity of antenna, A is the physical aperture area of the lens and λ is the wavelength at the designed frequency. $\eta_{rad} = G_e / D_a$ is the radiation efficiency. G_e is the measured gain. Then the total radiation efficiency can be re-written as follows

$$\eta = G_e \lambda^2 / (4\pi A) \tag{3-2}$$

The simulated overall antenna efficiency is 75.3%, which corresponds to a 24.7dBi gain. In our case, the measured gain is 23.8dBi. Considering the thin supporting layer structures added around lens, the actual physical aperture area is a little larger than that in simulation. The measured overall antenna efficiency is 59.9%. The experimental and simulated realized gain and their corresponding total radiation efficiencies in the frequency range of 8.2-12.5 GHz are presented in Fig. 3-9, respectively. The measured 2-

dB fractional realized gain bandwidth is 41.6% from 8.2 to 12.5 GHz. The total radiation efficiency of H-S lens is above ~40% in the frequency range, and decreases as the frequency gradually increases. This shows that the proposed H-S lens itself has intrinsic broadband response.
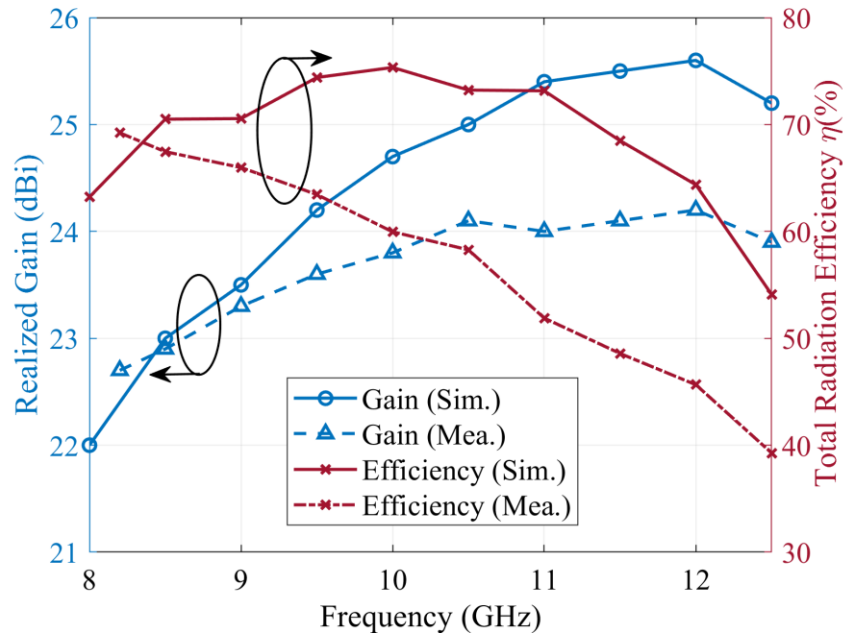
Figure 3-9 Simulated and experimental realized gain and corresponding total radiation efficiency of the H-S lens antenna.

3.6 2-D Beam-scanning by feed movement

All these previous studies about H-S lens are mainly focused on the typical case with blocky structure that the source feed can only be placed on the lens surface. The beam-steering ability of H-S lens concept has also not been investigated or mentioned. In this section, the functionality of 2-D beam-scanning for H-S lens was first explored by mechanically moving the waveguide. The whole of the H-S lens antenna is used as the transmitting antenna and is placed on a rotating platform, as shown in Figure 3-10.
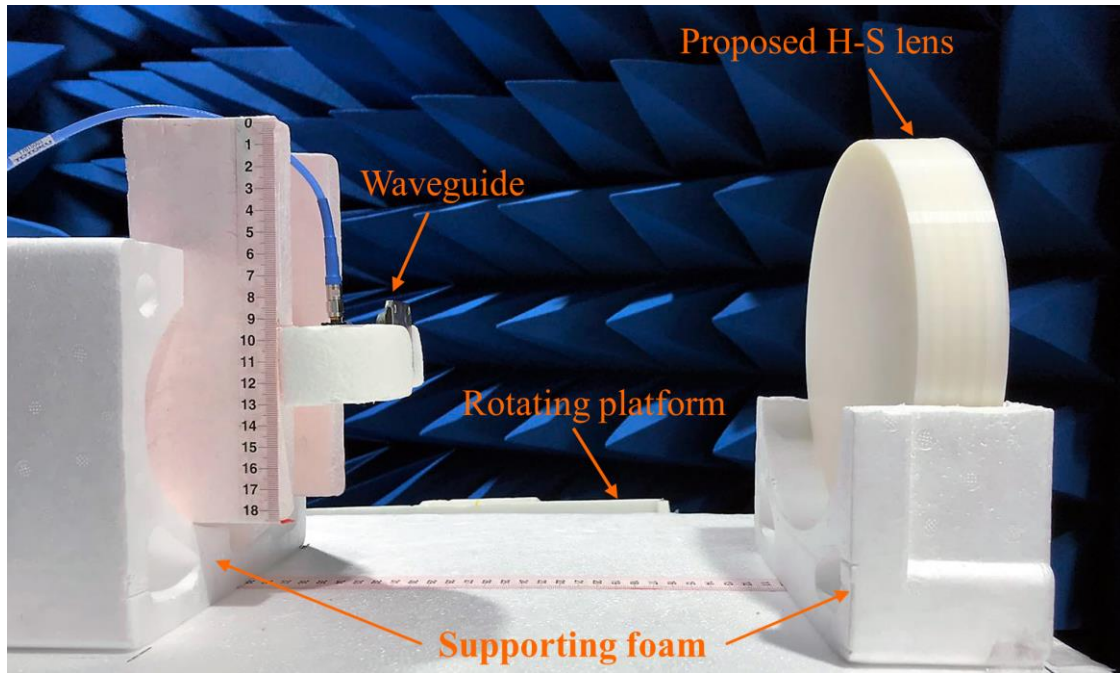
Figure 3-10 Photograph of the foam-based measurement setup in anechoic chamber.

Figure 3-11(a), (b) shows the simulated and measured radiation patterns for the WR-90 waveguide with and without the presence of the lens, for both the E-plane (yoz plane) and H-plane (xoz plane). The measured realized gain of the waveguide is about 5.8 dBi, and the realized gain of the lens antenna is about 18.9 dBi that is 13.1 dBi higher than the feed itself. It demonstrates the high realized gain can be achieved owing to the good phase transformation function of lens. Furthermore, the measured cross-polar levels of both E- and H-planes remain at a low level (less than –28 dB). The measured realized gain in the H-plane is only plotted as a function of the frequency for brevity, which demonstrates the broadband behavior of the proposed lens, as shown in Figure 3-11(c).
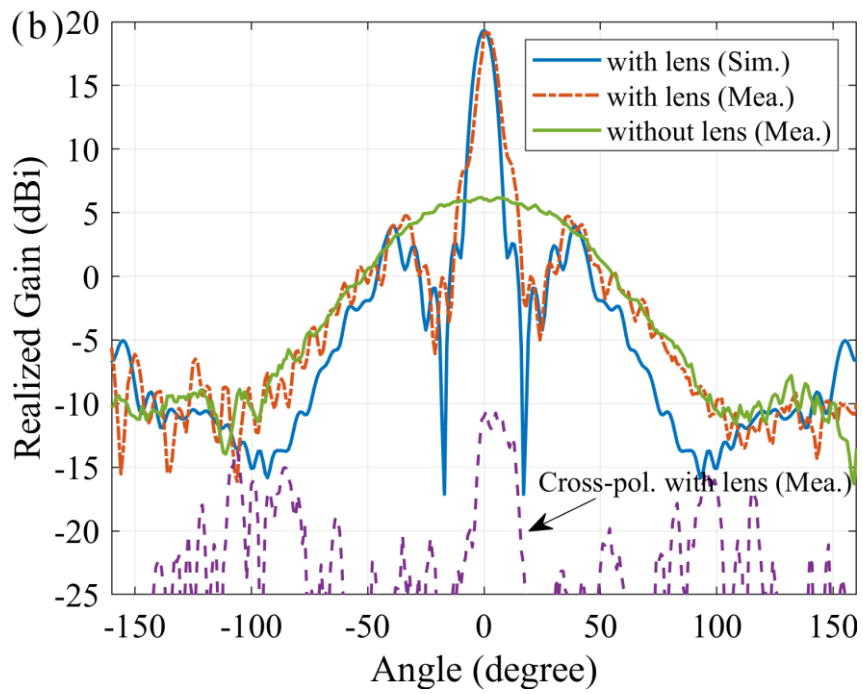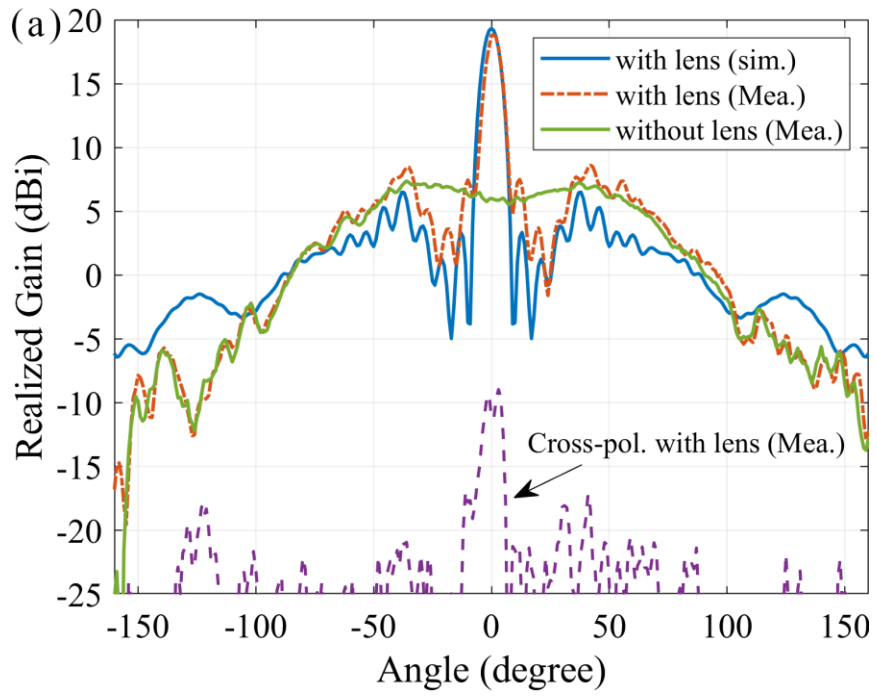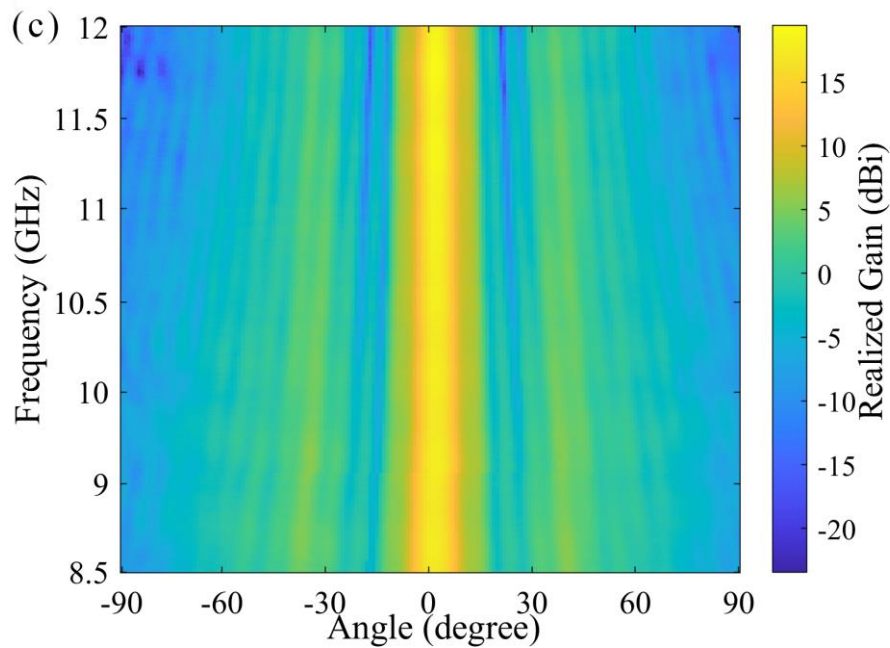
Figure 3-11 Simulated and measured radiation patterns of the proposed H-S lens antenna at 10 GHz. (a) E-plane. (b) H-plane. (c) Measured realized gain in the H-plane as a function of the frequency.

The waveguide was placed at the focal plane of the lens, and can be moved in x- and y-axis as shown in Figure 3-12(a) and 3-14(a), respectively. Figure 3-12(b)-(d) shows three examples of simulated 2-D electric field distribution for different feeding positions (x = 0, 30, −30 mm) along x direction. Similarly, three examples of simulated 2-D electric field distribution for different feeding positions (y = 0, 30, −30 mm) along y direction. It indicates that the waveguide placed at off-center position of lens leads to a steered beam. Considering the symmetric structure of lens, symmetric radiation patterns can be obtained for the corresponding symmetric feed positions with respect to the lens center.

Here, for the sake of brevity, the simulated and measured normalized H-plane radiation pattern of the lens antenna for different feeding positions at 10 GHz (x = 0, −25, −65, −95mm) are respectively illustrated in Figure 3-13(a)–(d). As the waveguide was move right along the x-axis, the high-gain radiation beam produced by lens was steered left accordingly.
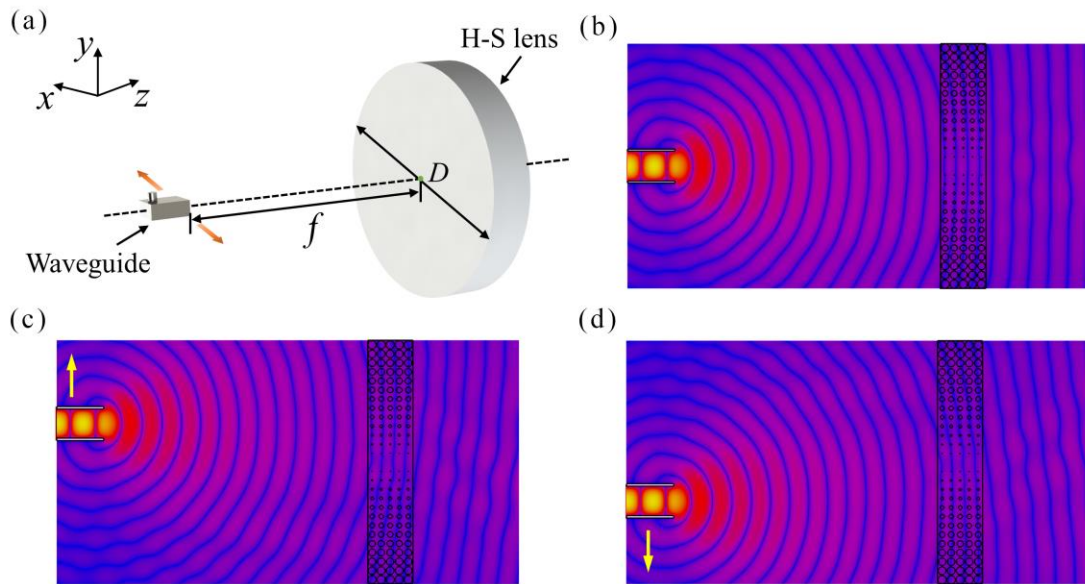
Figure 3-12 (a) 3-D model for H-S lens antenna. (b)-(d) Simulated 2-D electric field distribution for feeding position at x = 0, 30, -30 mm.
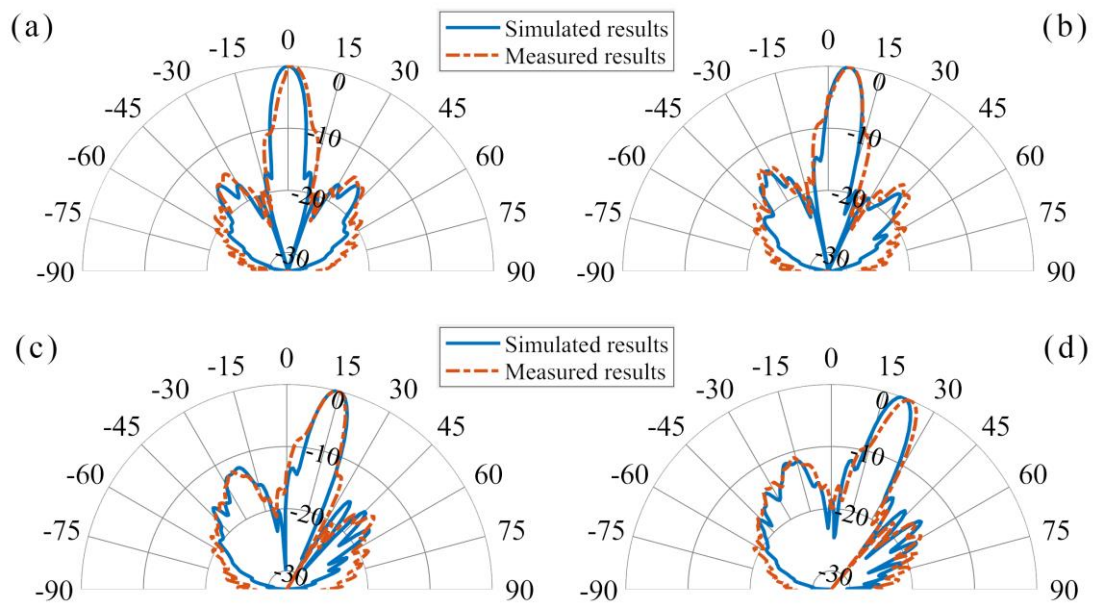
Figure 3-13 Simulated and measured normalized H-plane radiation pattern of the lens antenna at 10 GHz for different positions. (a) y = 30 mm. (b) y = −25 mm. (c) y = −65 mm. (d) y = −95 mm.

The same procedure is performed to obtain the simulated and measured normalized E-plane radiation pattern of lens antenna for different feeding positions at 10 GHz (y = 0, −25, −65, −95 mm), as shown in Figure 3-15(a)–(d). Similarly, as the

waveguide is move down along y-axis, the high-gain radiation beam produced by lens is steered up accordingly, which further indicates the proposed lens can perform 2-D beam steering very well by moving the feeding waveguide in the focal plane.
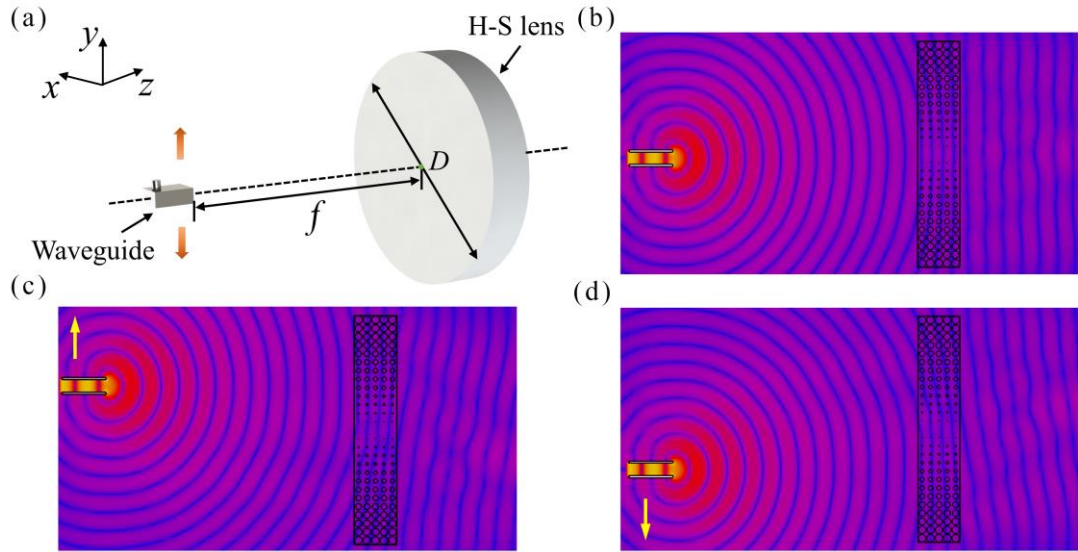
Figure 3-14 (a) 3-D model for H-S lens antenna. (b)-(d) Simulated 2-D electric field distribution for feeding position at y = 0, 30, -30 mm.
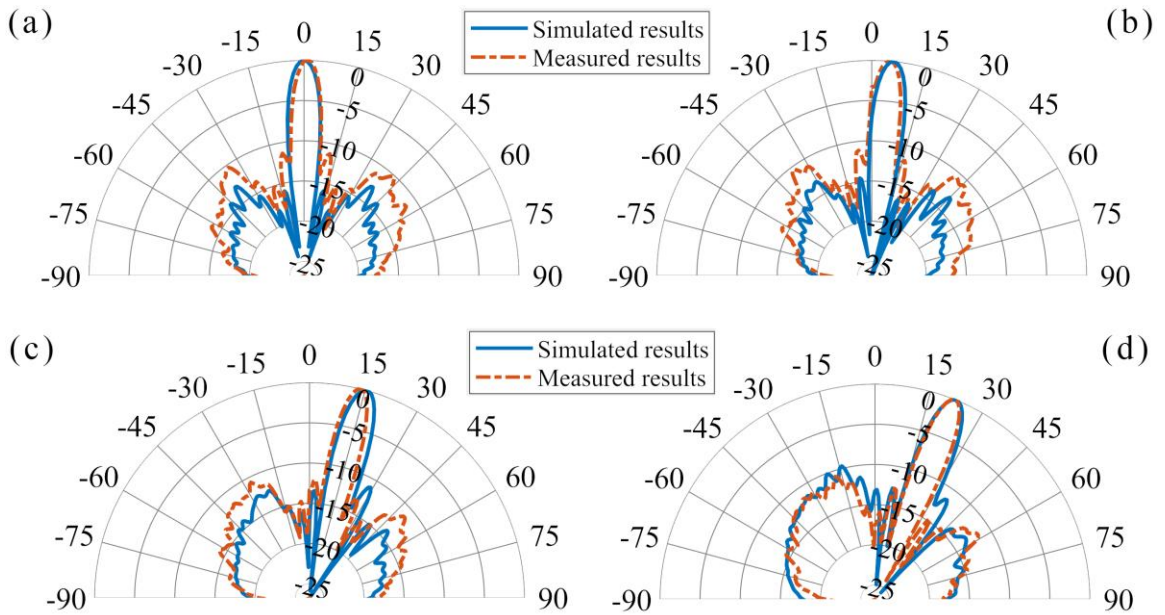
Figure 3-15 Simulated and measured normalized H-plane radiation pattern of the lens antenna at 10 GHz for different positions. (a) y = 30 mm. (b) y = −25 mm. (c) y = −65 mm. (d) y = −95 mm.

Figure 3-16(a) shows the simulated and measured peak gain versus steering angle in E-plane and H-plane, respectively. The maximum measured realized gain is 18.9 dBi. The small differences between measurement and simulation result occur due to uncertainties of measurement and limited manufacturing precision of 3-D FDM printing. Overall, the measured gain values are very close to the simulation results, indicating the good gain stability of lens with less than 1.2 dB variation among the effective beam-steering range (±20°).

In addition, the half-power beamwidth and side-lobe level (SLL) is shown in Fig. 10(b). The −3 dB beamwidth of beam with less than −10 dB SLL can be maintained well as the steering angle increases. Because an open-ended waveguide is used as the feeding source in our case, it has a certain effect on the maximum achievable gain, the SLL, steering angles and efficiency.
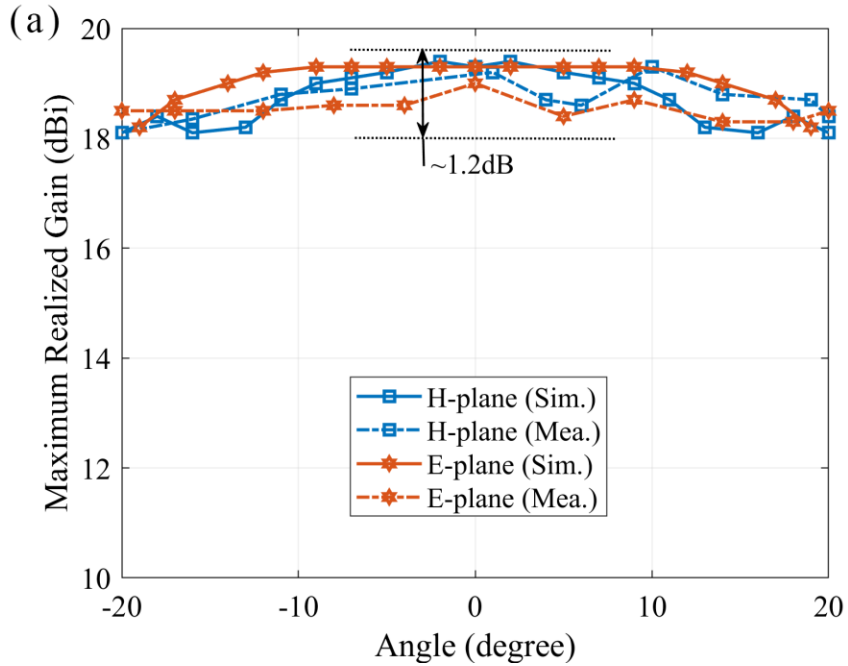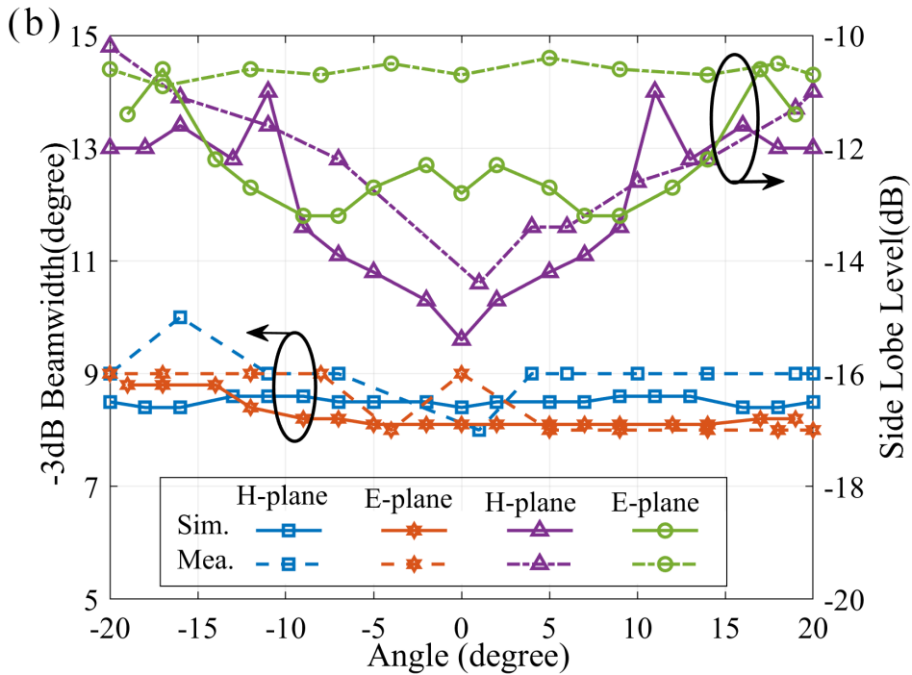
Figure 3-16 (a) Simulated and measured maximum realized gain versus steering angle. (b) −3 dB beamwidth of beam and SLL in E-plane and H-plane, respectively.

In our case, the efficiency of proposed lens system is mainly limited by the illumination of feeding source. Considering that the open-ended waveguide is utilized as feeding source, the aperture size of lens is much larger, resulting in low efficiency (~20%). It means that the proposed lens concept should be more effective if the optimization work for aperture size could be carried out. Despite the imperfections of the radiation performance with low efficiency, the simulation results are almost consistent with the measurement results, which revealing this new lens concept with unique low profile can be used in the 2-D beam-steering applications.

3.7 Summary

In this chapter, a new lens antenna type called hyperbolic secant (H-S) lens antenna with high gain and broadband characteristic was proposed for high directive antenna application based on ray tracing analysis and full-wave electromagnetic simulation. The attractiveness of this new lens is its intrinsic flat shape characteristic and extensibility for different antenna application scenarios, in addition to the advantages of

low-profile, lightweight, and high performance. Compared with conventional Luneburg, Maxwell fish-eye, and Eaton lens, the proposed lens has the unique flat shape characteristic, which provides great advantages in designing the low-profile planar lens antenna, avoiding using extremely complex conformal mapping methods. The perforated dielectric material of variable hole sizes is utilized to satisfy the required H-S refractive index distribution. A high gain and wideband printed antipodal fermi antenna as feeding source are employed in the proposed lens antenna prototype operating at 10 GHz. The simulated and experimental results showed good agreement, demonstrating 23.8 dBi realized gain at 10 GHz with 3-dB beamwidth of 9° and 2-dB fractional realized gain bandwidth of 41.6%. Besides, the total radiation efficiency is above ∼40% across all tested frequencies (8.2 GHz-12.5 GHz), which suggests the proposed H-S lens itself has intrinsic broadband response. Besides, the simplicity and low-cost fabrication of its lens design indicating great potentials in broadband high directive antenna applications.

Furthermore, the functionality of 2-D beam-scanning for H-S lens was first explored by mechanically moving the waveguide. The beam scanning capability in both the E-and H-plane was confirmed. It has been demonstrated that we can achieve 2-D beam steering in both the E-and H-plane among the effective beam-steering range (±20°) with around 18.9 dBi of realized gain with less than ∼1.2 dB variation and low side-lobe. This proposed lens concept could be also a potential alternative design for the existing planar GRIN lens antenna configurations, avoiding using complex conformal mapping methods.

CHAPTER 4

Performance Analysis for Beam-switching Concept of Hyperbolic Secant Lens

4.1 Beam-switching concept for 1-D beam steerable lens antenna

As mentioned above, H-S lens has unique characteristics of self-focusing that the rays oscillate in a sinusoidal way along the optical axis (z-axis) as shown in Figure 4-1(a). The oscillation period of the rays inside lens is defined as pitch (p). Both the pitch and width (w) of lens can be also easily adjusted to achieve the focusing phenomenon on the lens surface as illustrated in Fig.4-1(b). Hence, it provides a potential way to apply this lens concept to design integrated lens antenna configurations by just selecting the appropriate the pitch and width of lens. The beam-switching integrated H-S lens antenna concept can be also achieved by switch to solve the drawbacks of mechanical beam scanning in Chapter 3.
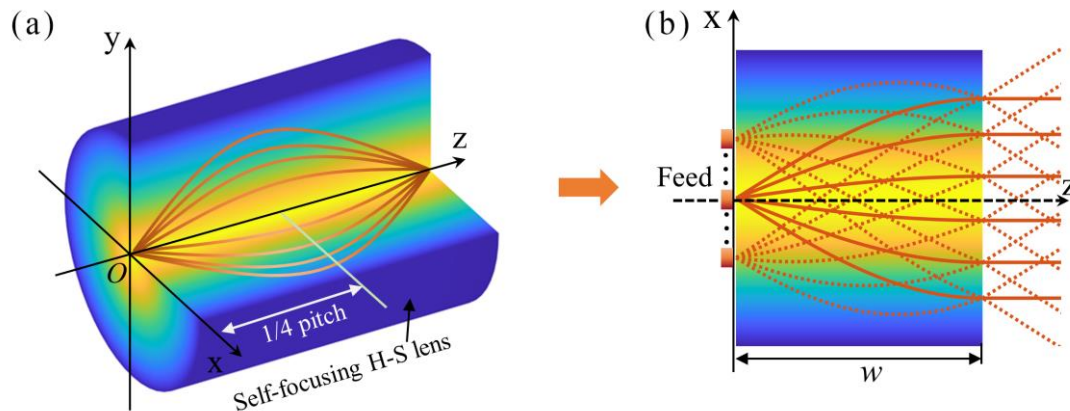
Figure 4-1 The unique self-focusing properties of H-S lens. (a) The rays oscillate in a sinusoidal way along the optical axis inside lens. (b) Schematic of integrated lens antennas configurations with appropriate the pitch and width.

The schematic view of proposed lens antenna excited by five rectangular microstrip patch antennas placed at the focal plane of lens is shown in Figure 4-2. Different beam steering angles can be achieved by simply switching on or off different

patch antennas. It should be noted that the patch spacing (d) is equal to 21 mm for reducing the mutual coupling (MC) between two microstrip patch antenna elements.
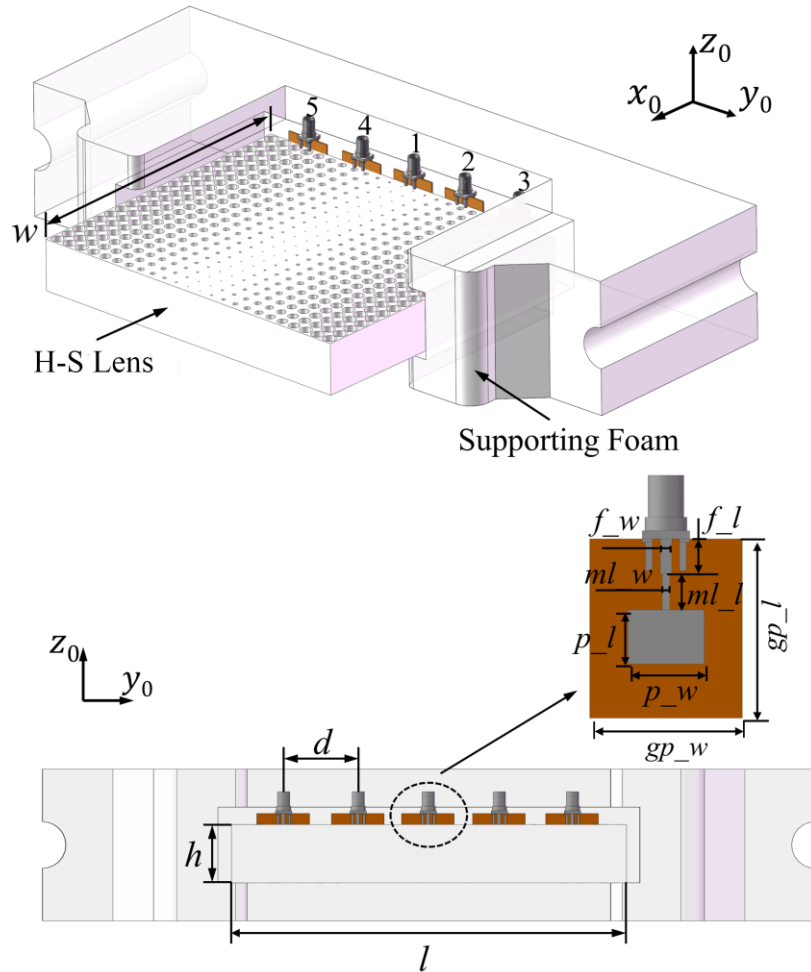
Figure 4-2 Schematic of proposed H-S lens antenna excited by five rectangular microstrip patch antennas in a 3-D model. (a) Perspective view. (b) Front view.

Table 4-1 lists the specific design parameters of lens antenna structure. The patch antenna is etched on the dielectric substrate with a relative permittivity of 2.55, loss tangent 0.001 and a thickness of 0.6 mm. And the polarization of the patch antenna is linear in z_0-axis direction. The lens focuses the radiation of patch antennas, which allows for beam-steering in the x_0-o-y_0 plane. Each position on the focal plane of lens corresponds to the radiation in one defined direction. In our case, the pitch, length, width and thickness of proposed lens is 0.25, 168.8 mm, 147.8 mm and 25 mm respectively.

Table 4-1 Geometry dimensions of H-S lens antenna structure

Element	Parameter	Values (mm)
Lens	Length l	168.8
	Thickness h	25
	Width w	147.8
Patch	Patch_length p_l	8.56
	Patch_width p_w	11.25
	Patch_spacing d	21
Feed line	Feed_line_length f_l	5.16
	Feed_line_width f_w	1.68
Ground plane	Group_plane_length gp_l	25.68
	Group_plane_width gp_w	22.50
Matching line	Matching_line_width ml_w	1.1
	Matching_line_length ml_l	5.35

Similarity, benefiting from the 3-D printing technology, the proposed planar H-S lens can be also easily fabricated by all-dielectric material with air-hole structure at a low-cost. Figure 4-3 illustrates the implemented design the procedure of H-S lens operating at 10 GHz. Using staircase approximation, the continuous relative permittivity profile of lens as shown in Figure 4-3(a) is discretized into 24 layers. In order to achieve the desired discrete relative permittivity distribution, the different sizes of perforation are utilized for simplicity based on the effective medium theory as shown in Figure 4-3(c). Considering that the SLA 3D printing is more accurate than FDM (fused deposition modeling), the perforation structure (21 × 24 holes) of lens in our case is fabricate by using SLA 3-D printing. The air hole sizes for different layers of lens are listed in Table 4-2. It is noted that only half of layers is shown in Table 4-2 owing to the axial symmetry of relative permittivity profile of lens.
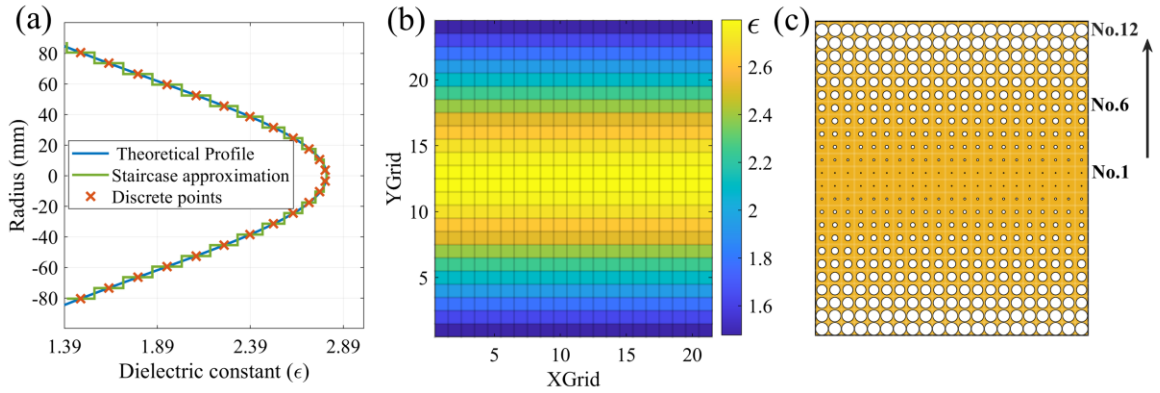
Figure 4-3 (a) Staircase approximation of continuous relative permittivity profile of H-S lens. (b) Discretization of 2-D relative permittivity profile (c) 2-D perforated structure of H-S lens (24 layers).

Table 4-2 The air hole sizes for different layers of H-S lens

Layer Number	Diameter of air hole (mm)
No.1	0.512
No.2	1.136
No.3	1.818
No.4	2.494
No.5	3.150
No.6	3.778
No.7	4.373
No.8	4.932
No.9	5.451
No.10	5.931
No.11	6.370
No.12	6.500

4.2 Ray tracing and beam-steering capability

To illustrate the beam-steering performance of ideal H-S lens, a ray tracing algorithm based on above-mentioned ray transfer matrices is applied. Considering that the proposed lens is axially symmetric, Figure 4-4(a), (d), (g) and (j) only give four examples of ray trajectory inside lens. The steering angles of beam is 0°, 10°, 20° and 35° respectively in these cases. Here, in order to further evaluate the steering capability of proposed lens with air-hole structure, a single patch antenna operating at 10 GHz is placed at the different positions of focal plane (x = 0mm, 10mm, 21mm, 40mm). The corresponding simulated 2-D electric field distribution is respectively shown in Figure 4-3(b), (e), (h) and (k) by using the electromagnetic field full-wave simulation in CST Microwave Studio. Obviously, the results of these two methods are in reasonable agreement, which indicates the good phase transform function of lens converting a spherical wave into a plane wave. Figure 4-3(c), (f), (i) and (l) illustrate the different 3-D radiation patterns in different directions can be realized by selecting different feed positions at the focal plane of lens. It should be noted that the loss tangent of lens material is not considered temporarily in this section.

However, it does not mean that the proposed lens can achieve the maximum steering angle of $\pm35^{o}$ in practical application of antenna engineering. For beam-steering application, the feeding source need to be displaced from the focal point on the central axis to produce an off-axis beam. But it leads to various types of lens aberration including spherical aberration, coma, astigmatism, curvature of field, and distortion. Among these aberrations, the coma aberration is the most undesirable effect that causes severe asymmetrical side lobe distortion [64].
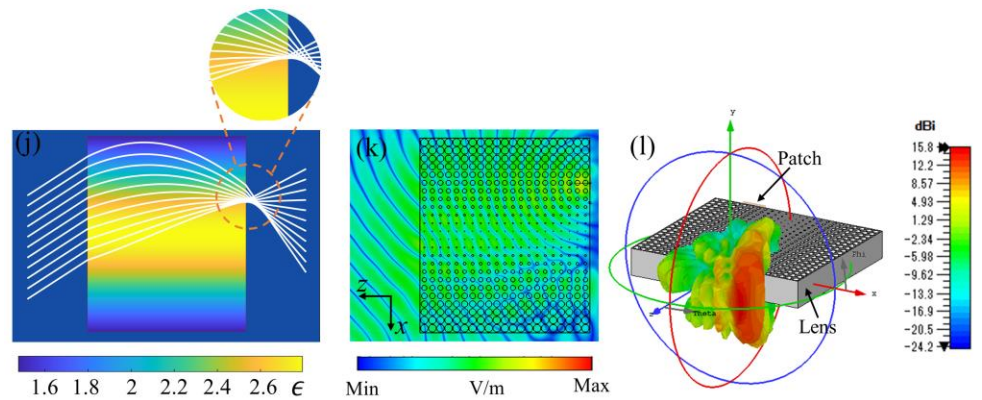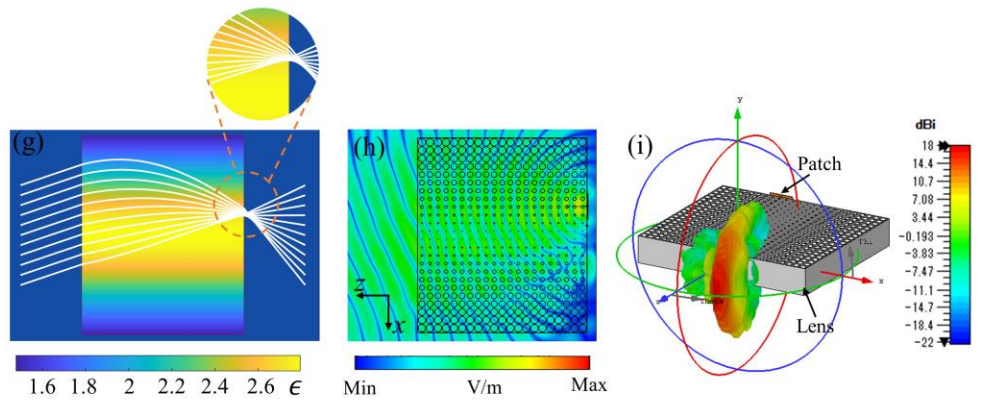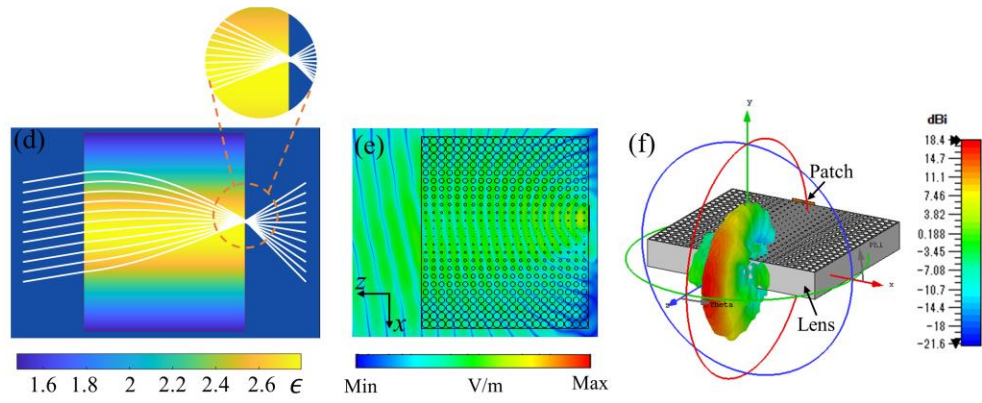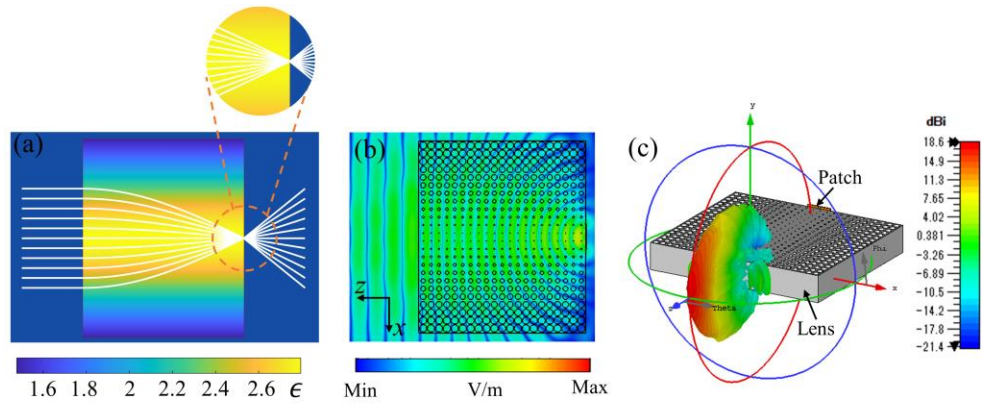
Figure 4-4 Ray tracing analysis of ideal H-S lens for different steering angles. (a) 0°. (d) 10°. (g) 20°. (j) 35°. Corresponding simulated 2-D electric field distribution for different feed positions. (b) x = 0 mm (e) x = 10 mm (h) x = 21 mm (k) x = 40 mm. The differ different 3-D radiation patterns in different directions (c) 0°. (f) 10°. (i) 20°. (l) 35°.

The design of proposed lens is based on above-mentioned ray tracing theory. The paraxial approximation is a key prerequisite in the design theory, which allows an important approximation: $\theta \approx \sin\theta \approx \tan\theta$. Thus, as can be seen from the Figure 4-5 (a), (d), (g) and (j), comatic aberration shows obvious increase as the off-axis angle of beam increases. It means that higher steering angles lead to higher phase error and deterioration of the corresponding radiated beam. Although the scan (gain) loss is about ~3dB with steering angel up to ±35°, the side-lobe level (SLL) is not much lower, as shown in Fig.4-5.
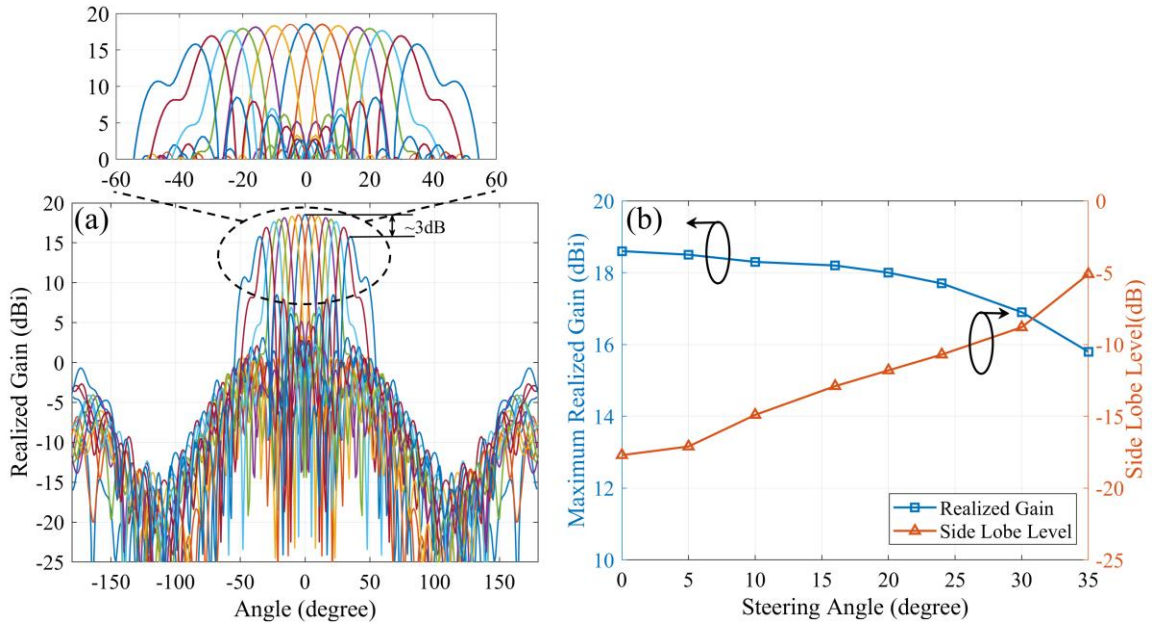
Figure 4-5 (a) Simulated H-plane (xoz plane) radiation patterns for different feeding source positions of proposed lens operating at 10 GHz. (b) Simulated maximum realized gain and SLL versus steering angle.

4.3 Prototype fabrications

A prototype of the proposed perforated H-S lens with a total of 21 × 24 holes (minimum hole diameter 0.51 mm) has been fabricated using SLA 3D printing (dimensional accuracy 0.1 mm). Here, the SLA resin (C-UV 9400E) is utilized to

construct the lens, which has a relative dielectric constant ~2.8, and loss tangent ~0.02[65]. Five patch antennas are glued to the rear surface of lens with equal distance of 21mm. Fig. 4-6 shows the fabricated prototype of the H-S lens antenna.
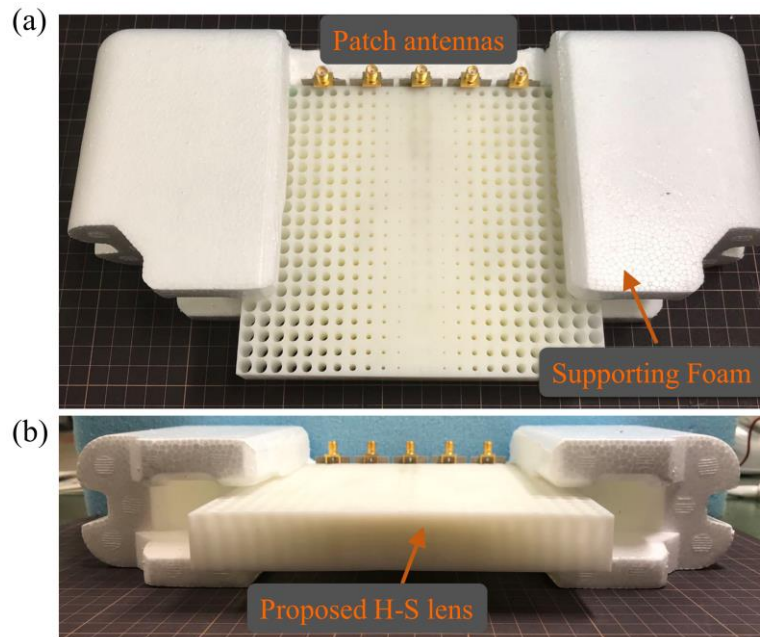
Figure 4-6 Photographs of the fabricated H-S lens antenna prototype. (a) Perspective view. (b) Front view.

4.4 Experimental results

The measured reflection coefficient magnitude for each port is given respectively in Figure 4-7(a). In our case, the common patch antennas operating at 10 GHz are utilized to be the feeding antenna, which has intrinsic limitations such as narrow bandwidth and low gain. Hence, the measured −10 dB impedance bandwidth is given instead of gain bandwidth. The measured −10 dB impedance bandwidth is about ~4%, which is limited by the feeding source (microstrip patch antenna). The frequency shift can be observed from the measured results, which could be attributed mainly to the presence of the perforated lens structure. It means that the certain amount of the frequency shift should be related to the equivalent permittivity for different air hole sizes where the patch antenna is placed. Besides, because of the limitation of 3-D printing, the phenomenon of warping or shrinkage would be observed that leads to unsmooth surface. The air gaps

between patch antenna and lens caused by the unsmooth lens surface and gluing process a small impact on the reflection coefficient magnitude. For coupling between these patch antennas, the coupling coefficients magnitude are shown in Figure 4-7(b). The suitable patch spacing (d = 21 mm) is selected to make the coupling coefficients magnitude less than −30dB.
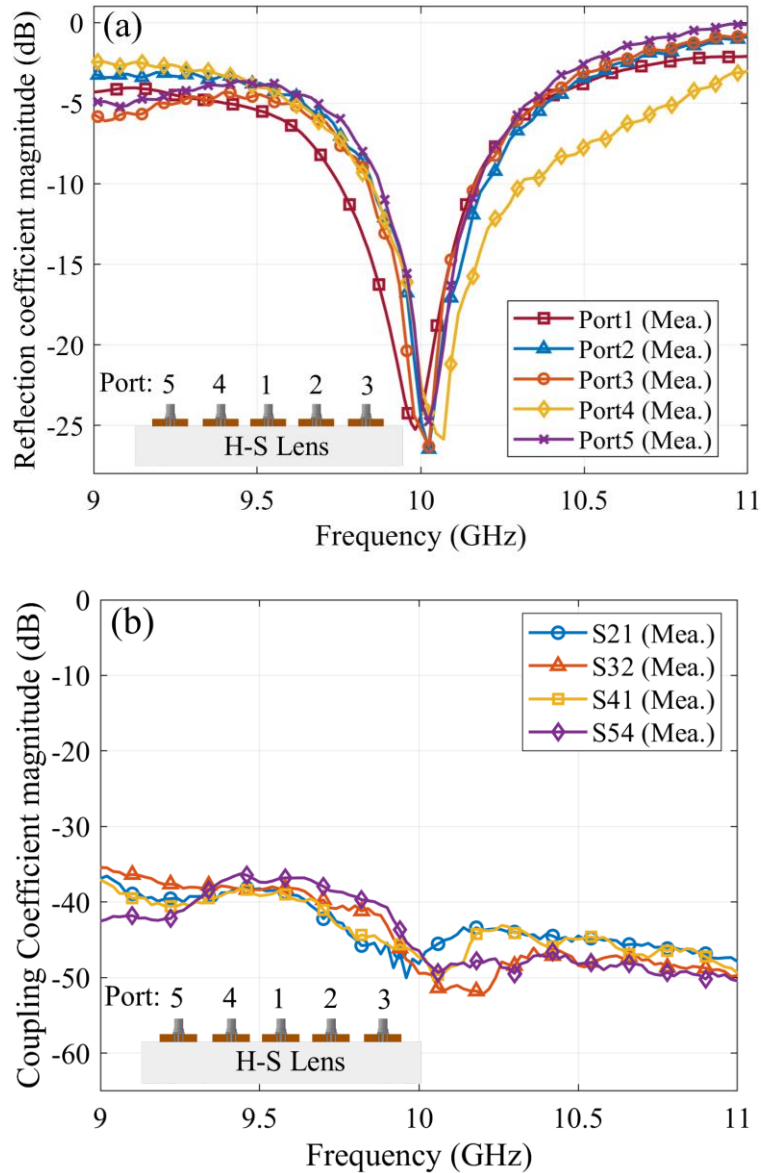
Figure 4-7 (a) Measured reflection coefficient magnitude of proposed lens antenna for each port.
(b) Measured coupling coefficients magnitude.

76

In our case, the measured center frequency of 10GHz is used for the experimental characterization of the radiation performances of proposed lens antenna. Considering that the proposed lens is axially symmetric, the measured normalized H-plane radiation pattern of the lens antenna at three feeding status are respectively illustrated for brevity in Figure 4-8, which indicate that we can achieve beam-steering capabilities from -20° to +20° with around 13.2 dBi of realized gain and side-lobe levels (less than -11.5dB), and up to potential steering angles (±30°) with around 10 dBi of gain, by simply switching on or off different patch antennas. It is to be noted that the values of realized gain, HPBW, SLL and steering angles for different feeding status are all measured results. The complete set of measured H-plane radiation patterns for five different ports is shown in Figure 4-9.

Realized Gian:~10.1dBi

HPBW:~10°

SLL:-6.51dB

Steering Angle:-35°

(c)
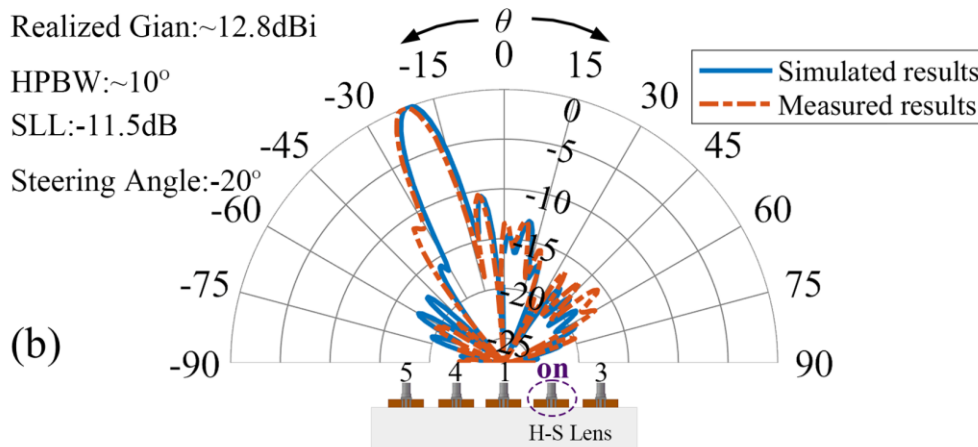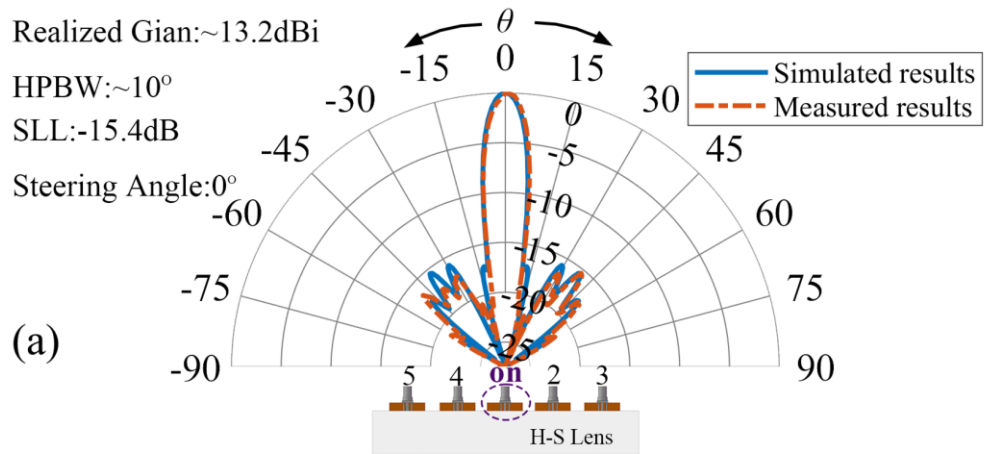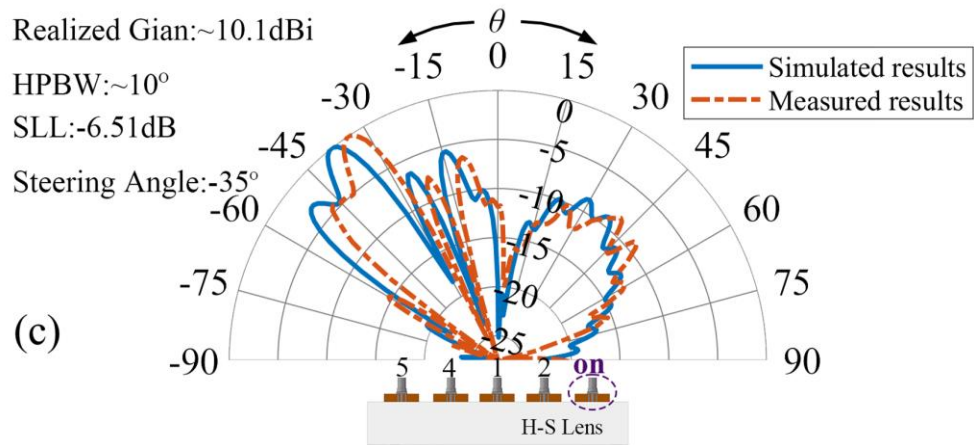
Figure 4-8 Comparison between simulated and measured normalized H-plane radiation patterns at 10 GHz for different feeding status. (a) Port 1 on. (b) Port 2 on. (c) Port 3 on. Noted that the values of realized gain, HPBW, SLL and steering angles for different feed feeding status are all measured results.
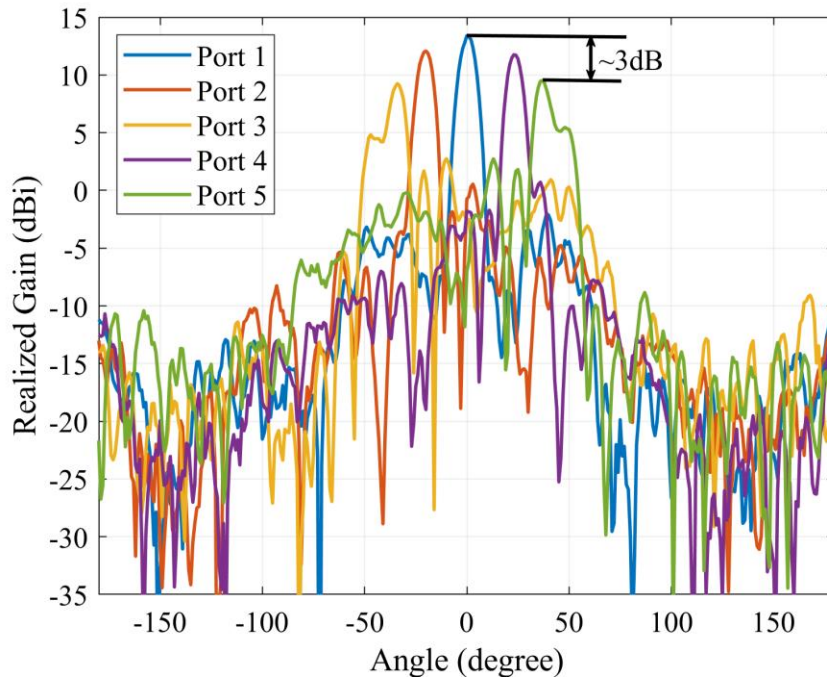
Figure 4-9 Complete set of measured H-plane radiation patterns at 10 GHz for different port status.

4.5 Limitation and discussion

When the steering angel is up to ±35º, the side-lobe level deteriorates further, and could be considered not acceptable (-6.51dB). This phenomenon occurs mainly due to the intrinsic phase error of lens (comatic aberration) resulting from displacement of the feeding source from the focal point on the central axis, as described in Section 2.3. Moreover, although the SLA 3D printing is more accurate than FDM (fused deposition modeling), the loss tangent of SLA resin used in our case is higher compared to the commonly used materials such as PLA (~0.011 at 10GHz) for FDM. Considering the loss tangent of SLA resin, the measured maximum realized gains with different steering angles are much lower than their simulated ones with lossless material (simulation in Section 2.3). Here, for the sake of brevity, the performance degradation for only feeding port 1 in the realized gain, total radiation efficiency, and SLL due to the high loss tangent is shown in Fig.11(a), and (b) respectively. It means that the performance of proposed lens antenna can be further improved by using other materials with lower loss tangent. Besides, the total radiation efficiency is calculated by the following equation

$$\eta = G_e \lambda^2 / \left(4\pi A\right) \tag{4-1}$$

where G_e is the realized gain, A is the physical aperture size of the lens and λ is the wavelength at the designed frequency. The physical aperture size of proposed lens is little larger, considering that the common patch antenna at 10GHz is utilized as feeding antenna. The aperture size can be further optimized to get good radiation efficiency. If the feed antenna with a higher directivity, the unwanted backside radiations would be suppressed, which can also improve the radiation performance.

Furthermore, the radiation performance of the lens system is both determined by the lens and the feeding antenna. The common patch antenna is utilized as feeding source in our cases, which has some drawbacks such as narrow-band. Thus, the proposed beam-switching lens antenna is also narrow-band. Despite the imperfections of the radiation performance (e.g., high side-lobe levels) with high steering angles and above-mentioned limitations, the simulation results are almost consistent with the measurement results considering uncertainties due to fabrication and measurement, as shown in Fig.9. This

proposed lens concept could be applied in the beam-steering applications for allowing a low-cost, low-profile and easy-to-fabricate beam-switching planar array antenna for microwave communication systems.
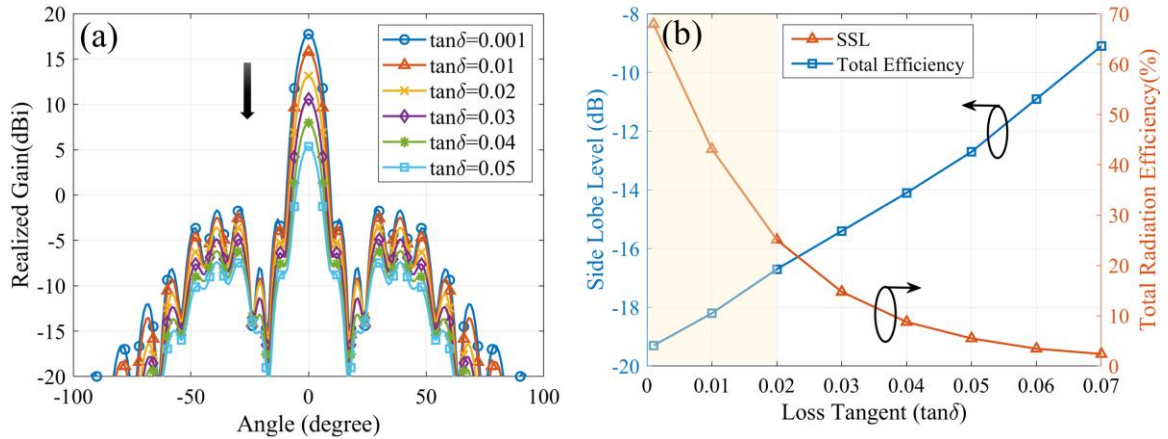
Figure 4-10 The performance degradation for feeding port 1 in the gain, total efficiency, and SLL due to the loss of material. (a) Simulated H-plane radiation pattern at 10 GHz versus loss tangent (b) SLL and total radiation efficiency versus loss tangent respectively.

4.6 Summary

In this chapter, a beam-switching planar H-S lens antenna concept achieved by switch was proposed to solve the drawbacks of mechanical beam scanning in Chapter 3. The performance of this all-dielectric planar H-S lens for 1-D beam-steering application was first investigated. This new lens concept has its intrinsic flat shape characteristic, which allows for a simple low-cost planar feed technology.

Based on ray tracing analysis and full-wave electromagnetic simulation, the performance of proposed lens prototype excited by five rectangular microstrip patch has been evaluated at 10 GHz. The simulated and measured results showed good agreement, demonstrating that we can achieve beam-steering capabilities in H planes from −20° to +20° with around 13.2 dBi of realized gain and SLL (less than −11.5dB), and up to ±30° with around 10 dBi of realized gain. Moreover, higher steering angles lead to higher phase error resulting from comatic aberration and deterioration of the corresponding

radiated beam. Most importantly, the realized gain, efficiency and SLL can be further improved to get better radiation performances by using other 3-D printing materials with lower loss tangent or more advanced manufacturing technology. Due to its intrinsic flat shape characteristic, this proposed lens concept could be a potential alternative design for developing a low-cost, low profile and easy-to-fabricate beam-switching array antenna for microwave communication applications.

CHAPTER 5

Single-pixel Scanning Micro- and Millimeter Wave Imaging with Surface Focusing

5.1 Single-pixel scanning imaging concept by using H-S lens

As one of the most critical devices in quasi optical imaging system, lens is particularly expected to achieve high resolution focusing with large numerical aperture (NA) and broadband bandwidth. There have been several well-known types of lenses, such as solid immersion lens[66, 67, 68, 69], super-oscillation lens[70, 71] and meta-lens[72, 73, 74, 75]. Although high resolution focusing can be achieved by these lens type, the problem of small NA and narrow bandwidth still exists. Most importantly, the related research of these lens mainly focuses on optical imaging applications. Considering the requirements of manufacturing materials and fabrication process in microwave engineering, it is still a great challenge to apply these optical lens concepts in the microwave imaging system. As mentioned above, the proposed H-S lens can focus wave at the central axis of the lens periodically as shown in Figure 5-1(a) has received increasing attention not only in the field of optics but also in microwave engineering. Once the oscillation period (P) called pitch is determined, various interesting phenomena such as converging and point to point imaging can be observed by choosing the appropriate length of lens. Moreover, it has the property of being spherical aberrations free. The off-center rays have the same focusing behavior as paraxial rays, which enables to focus rays to the smallest possible spot in subwavelength scale. For the case of $P = 0.5$, if a point source is placed at the center point of lens front surface, the rays intersect perfectly at a focal point on the rear surface of lens as shown in Figure 5-1(c).

In [76], a planar binary H-S lens to generate a near-surface focal spot with full-width half-maximum (FWHM) of 0.102λ was reported. Then, a nanoslit structure was utilized in a silicon-based planar H-S micro-lens in [77], which further improves the resolution to 0.043λ. The tight focusing of a second order cylindrical vector beams by a H-S lens was investigated in [78]. The diffraction limit in this case is FWHM = 0.154λ. Furthermore, the frequency response and polarization dependence photonic crystal H-S

lens in hexagonal and rectangular lattices was explored in [79] to evaluate the possibility of transverse focusing application in optical fiber. However, all these previous studies mainly focused on the focusing property for typical case ($P = 0.25$) of 2-D planar H-S lens, which are only analyzed and validated by full wave numerical simulation. There is not much information about how to put this lens concept into practice, not to mention the practical imaging application. But in [80, 81, 82], it was proved that an all-dielectric perforation structure can offer a potential technique for fabricating the H-S lens in microwave frequency range. Moreover, the possibility of subwavelength microwave imaging by using 2-D planar H-S Lens ($P = 0.25$) with FWHM around 0.2λ as well as large NA of 2.04 at frequency range of 7–14 GHz was indirectly demonstrated in [81].
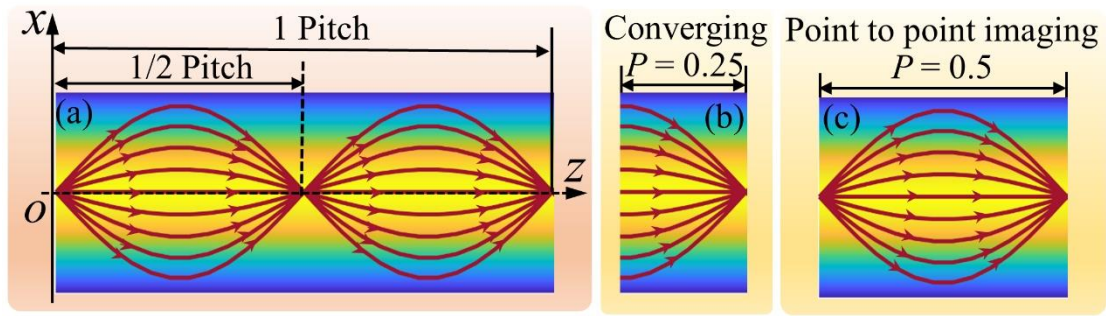
Figure 5-1 (a) The H-S Lens with unique propagation characteristics of self-focusing. Special cases for various interesting phenomena such as (b) converging and (c) point to point imaging with different pitch.

But, despite all this, this unique characteristic of surface focusing provides a potential way to ensure a higher numerical aperture, which produces a more highly resolved image. The purpose of this letter is to apply surface focusing H-S lens with a compact structure, simple fabrication process and cost-effectiveness into a single-pixel scanning near-field microwave imaging system. In order to create a 2-D image, H-S lens equipped with a single receiving antenna need to be moved linearly along the x- and the y- axis to scan across the surface of imaging object, as shown in Figure 5-2.
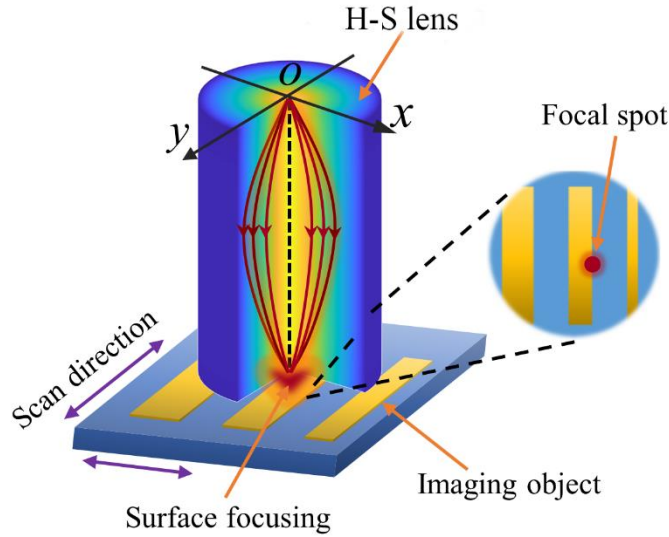
Figure 5-2 The schematic view of surface focusing H-S Lens ($P = 0.5$) for single-pixel scanning imaging.

5.2 Realization of H-S lens for micro-/millimeter-wave imaging

There are various manufacturing technologies such as foam pressing[83] , PCB milling[84, 85, 86] and metamaterials[87, 88, 89, 90]to fabricate GRIN lens. However, compared to the 3-D printing, these manufacturing techniques need complicated and expensive special fabrication process. Here, based on easily accessible 3-D printing, two fabrication processes using the internal perforation structure of various air-hole sizes and different infill ratios of material is utilized to achieve intended refractive index profile of H-S lens for microwave and millimeter-wave imaging, respectively. Polylactic acid (PLA) plastic material is also utilized in this case. The specific design procedure of two fabrication processes mentioned above are as follows:

    1)   Perforation structure for microwave imaging at X-band

The pitch, diameter, and length of designed H-S lens operating at X-band is 0.5, 70mm, and 133mm respectively. Figure 5-3(a)-(d) illustrates the design steps of lens operating at 10 GHz. The 2-D continuous relative permittivity distribution of lens needs to be discretized first. Here, the unit-cell element is a cube with circular air-hole, which has a size of 7 mm×7 mm. After discretizing, the corresponding grid sizes is 19×10. The different sizes of air-hole can be utilized to obtain the intended discrete effective

permittivity (ε_{peff}), as shown in Figure 5-3(c) In order to generate the cylindrical H-S lens, the discrete 2-D air-hole structure need to be rotated around the central axis

2) Infill structure for Millimeter-wave Imaging at Ka-band

Considering the practical dimensional accuracy of the FDM (fused deposition modeling) 3D printer, the air-hole structure cannot be fabricated in infinitely small size, which limits its imaging application in the high frequency. However, by controlling the infill ratio of PLA (PLA volume percentages), the functionality of the proposed lens concept can be easily expanded to higher frequency bands such as millimeter wave. The relationship between the effective permittivity (ε_{ieff}) and infill ratio (v_{ir}) is approximately linear, which can be determined by the equation 2-26.

Here, the pitch, diameter, and length of designed H-S lens operating at Ka-band is 0.5, 27mm, and 50mm respectively. Unlike the above-mentioned grid discretization, the 2-D continuous relative permittivity distribution of lens needs to be discretized into 9 layers correspondingly. The different infill ratios of PLA are utilized to achieve the intended discrete permittivity distribution of each layer, as shown in Figure 5-3(g). It should be noted that considering the axial symmetry of relative permittivity distribution of H-S lens, Table I only lists the air-hole sizes and infill ratios from layer No.1 to layer No.5.

Table 5-1 The Air-hole sizes and Infill Ratios with Corresponding Layer

X-band			Ka-band		
Layer (No.)	Air-hole diameter (mm)	ε_{peff}	Layer (No.)	Infill ratio (%)	ε_{ieff}
1	0.571	2.762	1	98.6	2.775
2	1.250	2.620	2	93.4	2.681
3	1.947	2.362	3	79.1	2.423
4	2.574	2.035	4	58.9	2.061
5	3.108	1.685	5	36.9	1.665

(a)

(e)

Grid Discretization

Layer Discretization

(b)

(f)

Perforation

No.1
No.2
No.3
No.4
No.5

Infill

No.1
No.2
No.3
No.4
No.5

(c)

(g)

Designed lens at X-band

Designed lens at Ka-band

(d)

(h)
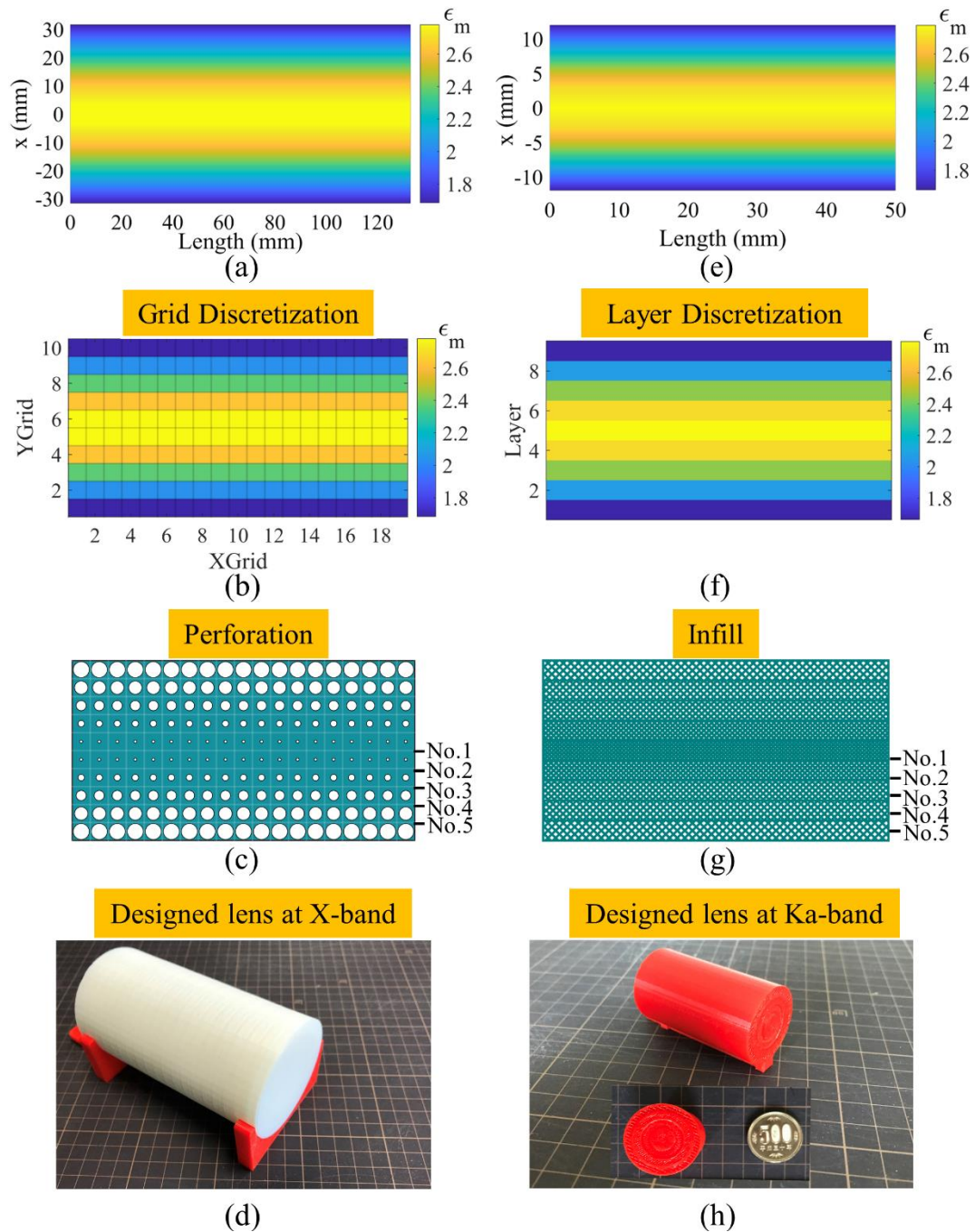
Figure 5-3 The design procedure of H-S lens operating at X-band with perforation structure. (d) The fabricated prototype of designed lens at X-band. (e)-(g) The design procedure of H-S lens operating at ka-band with different infill ratios. (h) The fabricated prototype of designed lens at Ka-band.

5.3 Imaging resolution and surface focusing analysis

The numerical aperture (NA) of a lens is the most important design criteria in defining the imaging resolution characteristics for the focusing system, which depends on the refractive index of surrounding medium and the sine of the maximum ray angle. There are several definitions of the resolution criteria such as Rayleigh resolution limit of $0.61\lambda / NA$ and Abbe diffraction limit of $0.5\lambda / NA$. (λ is the wavelength). However, a more practical criterion that is adopted instead of the Abbe and Rayleigh criterion is the full width at half maximum (FWHM) of focal spot intensity, which is defined as below [91]

$$\text{FWHM} = 0.51\lambda / \text{NA} \qquad (5\text{-}1)$$

Obviously, higher values of numerical aperture mean the better spatial resolution. The general form of numerical aperture of H-S lens can be derived from the ray equation in the gradient-index medium, and be determined using the following expression [92]

$$\text{NA} = \sin\theta_m = \sqrt{n^2(x_0) - n^2(r)} \qquad (5\text{-}2)$$

where $\theta m \, \theta_m$ is the maximum cone angle at which a ray can be accepted by the aperture of lens. $x0 \, x_0$ are the initial position of the ray in the aperture of lens. $r \, r$ is the radius of lens.

Then, the FWHM of focal spot at the rear surface of

$$ML_{\text{FWHM}} = \frac{0.51\lambda}{n_0\sqrt{1 - \text{sech}^2(2\pi Pr/L)}} \qquad (5\text{-}3)$$

Here, for the designed lens operating at X-band, $P = 0.5$, $L = 133$ mm and $r = 35$ mm. Equation 5-3 then gives a maximum NA of 1.136, which corresponds to the theoretical imaging resolution limit of 0.45λ. Meanwhile, the theoretical maximum NA and FWHM for the designed lens operating at Ka-band ($P = 0.5$, $L = 50$ mm and $r = 13.5$ mm) is 1.155 and 0.44λ respectively. Obviously, in both cases, the theoretical imaging resolution limit of designed lens is around 0.45λ.

To illustrate focusing performance, a ray tracing procedure (MATLAB source code provided in appendix) to verify the proposed lens design is performed based on the 2-by-2 ray transfer matrix (ABCD) theory [82]. Here, for the sake of brevity, the ray trajectory of proposed lens design for X-band is only shown in Figure 5-4. As expected, the rays start from the center point of lens front surface, and eventually intersect perfectly at a focal point on the rear surface of lens. The same ray tracing procedure of lens design for Ka-band can be performed to get the same results by using above-mentioned MATLAB code.
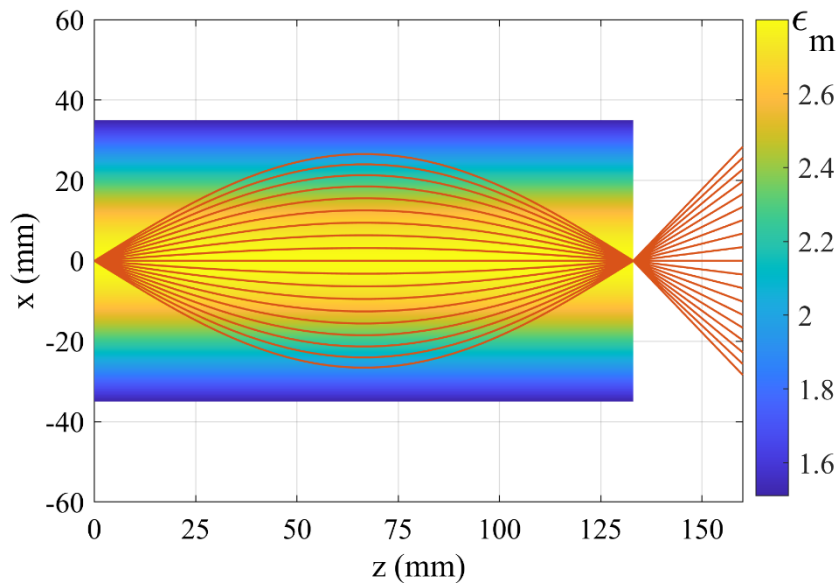
Figure 5-4 The ray tracing analysis of proposed H-S lens design for X-band based on the 2-by-2 ray transfer matrix (ABCD) theory.

Moreover, the high-resolution focusing performances of proposed cylindrical H-S lens from 8.2 to 12.5 GHz is presented in Figure 5-5(a)-(i). The WR-90 waveguide operating at X-band with polarization along the y-axis was placed at the center point of lens as a feed source. By using the full-wave electromagnetic simulation, the 2-D electric field distribution at yoz plane from 8.2 to 12.5 GHz inside lens is given in Figure 5-5(a), (b) and (c), respectively. After propagating through lens, the electromagnetic waves are well concentrated to a focusing spot on the rear surface of lens. Obviously, the results of these two methods are in reasonable agreement, which indicates that the proposed lens

design at X-band can be a good phase transformer to convert a diverging spherical wave into a converging spherical wave.

(a)

(d)

(e)

(b)

(f)

(g)
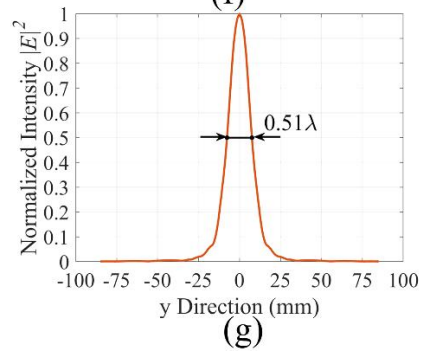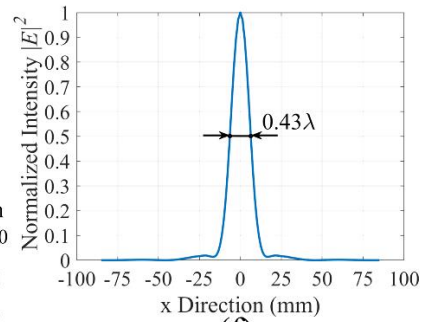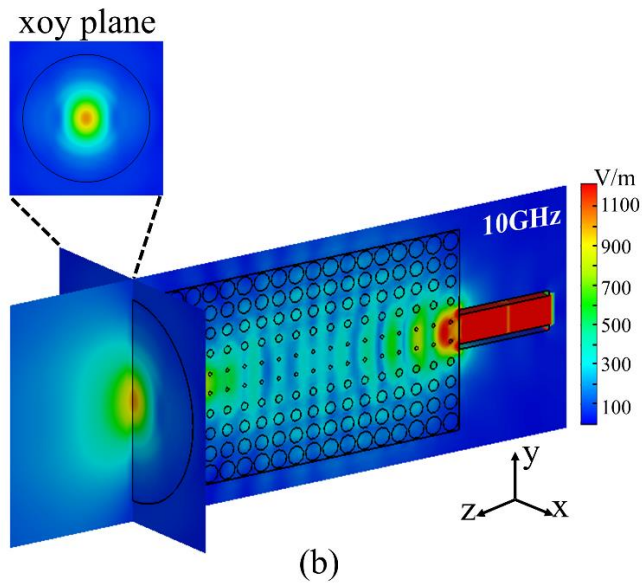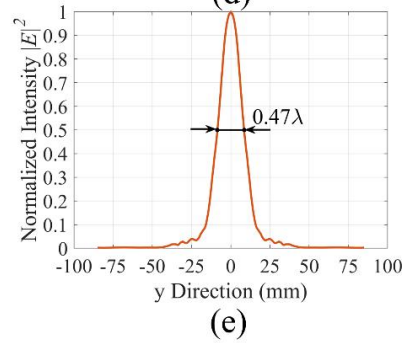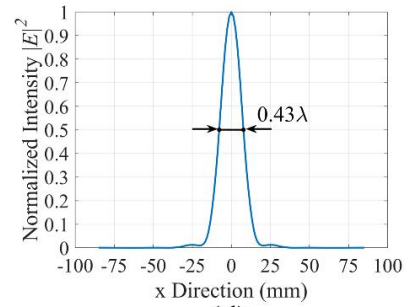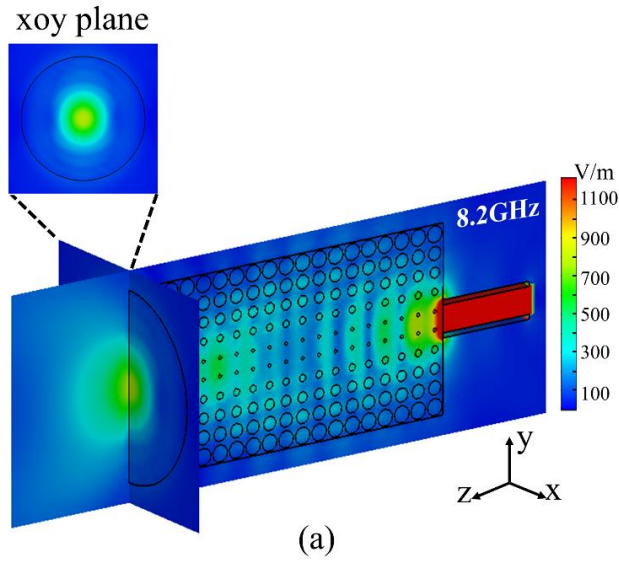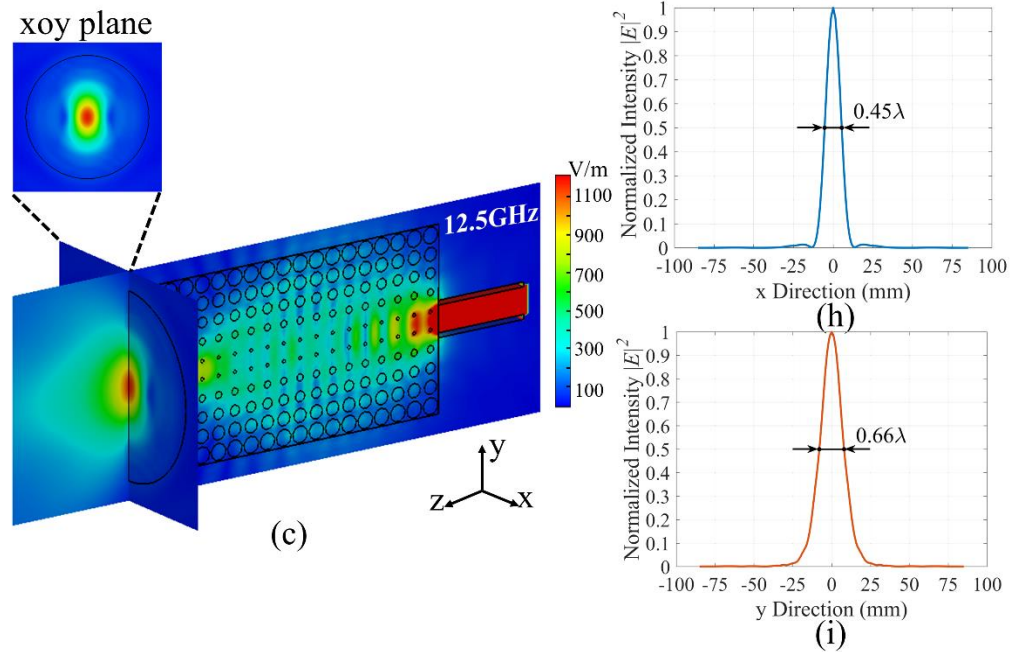
Figure 5-5 The high-resolution focusing performances of proposed H-S lens at X-band. (a-c) Simulated 2-D electric field distribution at 8.2 GHz, 10 GHz and 12.5 GHz respectively with waveguide operating at X band with polarization along the y-axis as source feed. (d)-(i) normalized electric intensity $|E|^2$ profiles along x- and y- direction at the focusing plane (xoy plane) at 8.2 GHz, 10 GHz and 12.5 GHz respectively.

In order to quantitatively analyze the focusing performance of the proposed lens design, the normalized electric intensity $|E|^2$ profiles along x- and y- direction at the focusing plane (xoy plane) from 8.2 to 12.5 GHz are shown in Figure 5-5(d)-(i), respectively. The values of FWHM for the normalized electric intensity profile along x-direction are all around 0.45λ. Although the values of FWHM for the electric intensity profile along y- direction tend to increase as the frequency increases, the variation is not very large (less than 0.15λ) considering open-ended waveguide as the feeding source.

Besides, the simulation model of Mikaelian lens operating at Ka-band is composed of five concentric circular cylinders with radially-varied permittivity of 1.665, 2.061, 2.423, 2.681 and 2.775. The same procedure is performed to obtain the simulated 2-D electric field distribution at yoz plane from 26.5 to 40 GHz, as shown in Figure 5-6(a)–(c). Similarly, the electromagnetic waves can be also concentrated to a focusing spot on the rear surface of lens, which further indicates the proposed lens concept can be

90

applied in higher frequency bands very well. As depicted in Figure 5-6(d)-(i), the values of FWHM for the normalized electric intensity profile along x- and y- direction are all around 0.5λ.

(a)

(b)

(d)

(e)

(f)

(g)
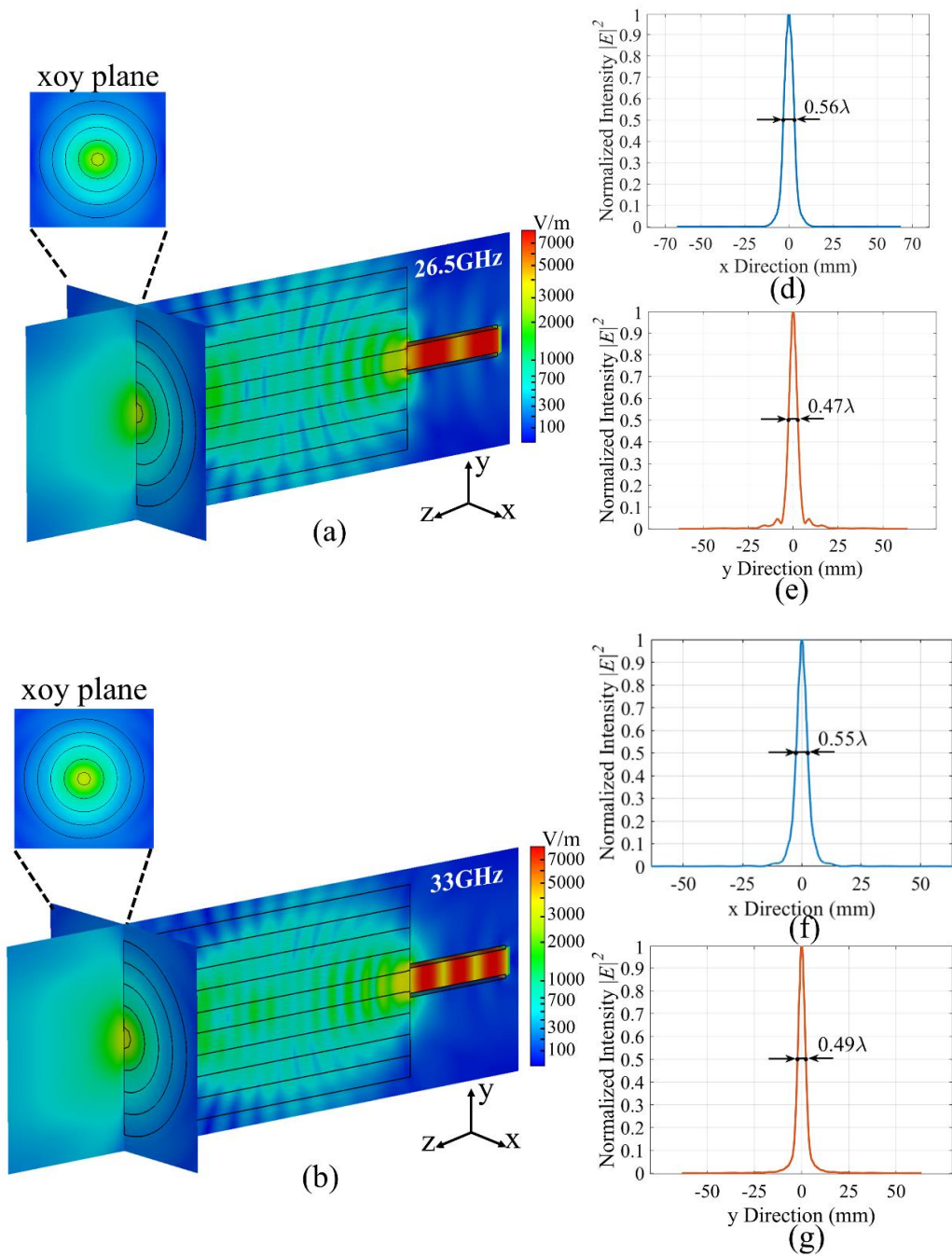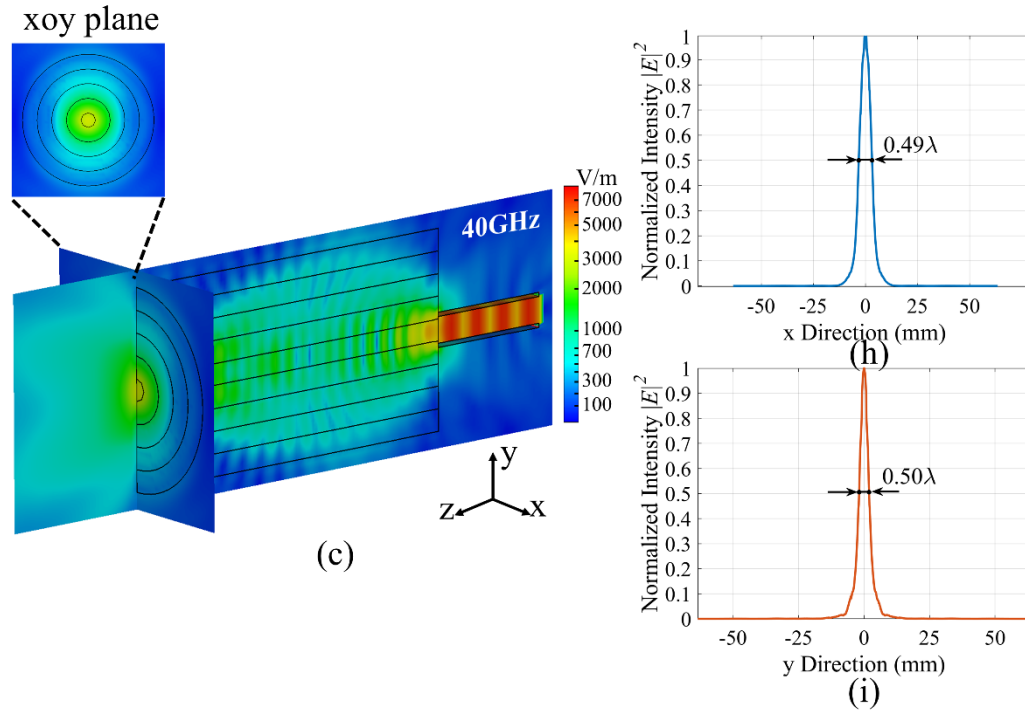
Figure 5-6 The high-resolution focusing performances of proposed H-S lens at Ka-band. (a-c) Simulated 2-D electric field distribution at 26.5GHz, 33GHz and 40GHz respectively with waveguide operating at Ka band with polarization along the y-axis as source feed. (d)-(i) normalized electric intensity $|E|^2$ profiles along x- and y- direction at the focusing plane (xoy plane) at 26.5GHz, 33GHz and 40GHz respectively.

Due to the limited number of discrete concentric circular cylinders in the simulation model, the small differences between theoretical and simulated FWHM occur. Overall, the designed H-S lens operating at these two frequency bands can achieve subwavelength imaging resolution of ~0.5λ.

5.4 Spatial resolution performance of designed H-S lens operating at X-band

Figure 5-7 illustrates the schematic 3D view of the proposed single-pixel scanning micro-/millimeter-wave imaging measurement setups. It consists of four main parts, the designed cylindrical Mikaelian lens, standard waveguide, vector network analyzers (VNA), 2-D linear guide rail. The spatial resolution imaging experiment was performed by the time domain measurement method. The standard waveguide operating at X- and Ka-band not only serves as a microwave transmitter (Tx) but also works as a receiver

(Rx). The imaging object is fixed on the 2-D linear guide rail, and is moved in the horizontal and vertical direction step by step. The measured echoed signals for each of the reflecting points (or pixels) at the imaging object can be recorded by VNA, which form a 2-D image.
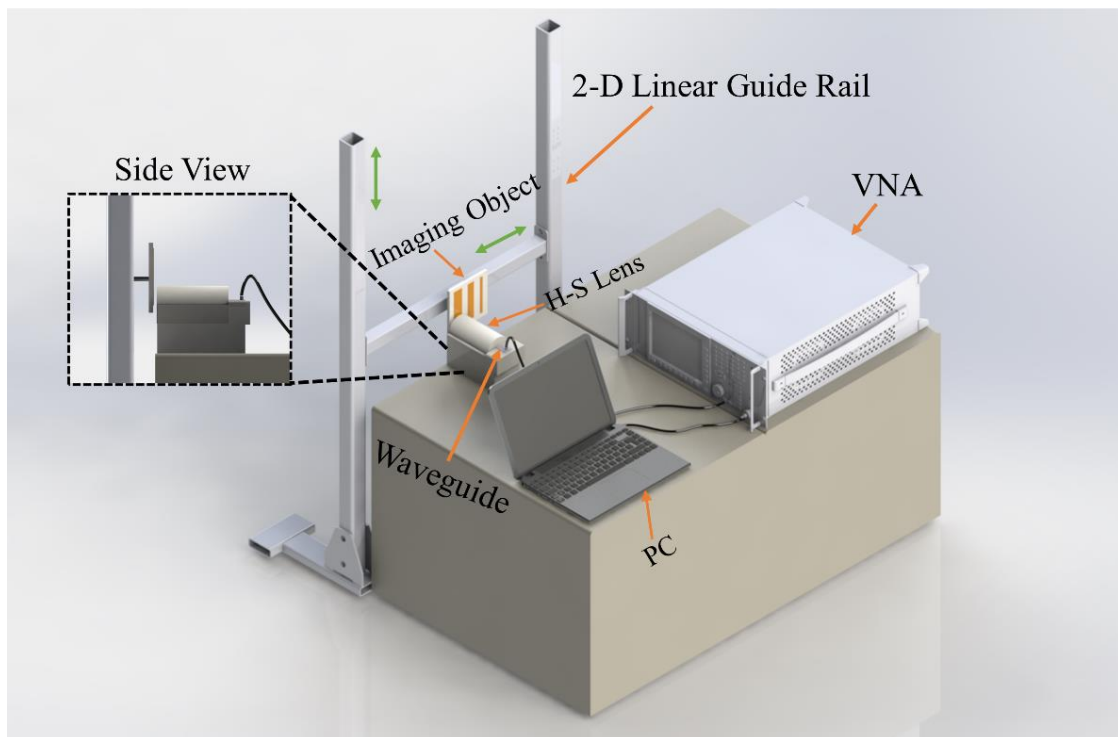
Figure 5-7 3-D perspective view of proposed single-pixel scanning micro-/millimeter-wave imaging measurement setups.

Here, for the sake of brevity, Figure 5-8 just shows the foam-based measurement setup for single-pixel scanning microwave imaging. The designed lens prototype operating at X-band is utilized. While not blocking the movement of the 2-D linear guide rail, the actual distance between the imaging target and the lens is required to be kept as small as possible. Noted that the measurement setup for millimeter-wave imaging by using lens prototype operating at Ka-band are similar to this one.
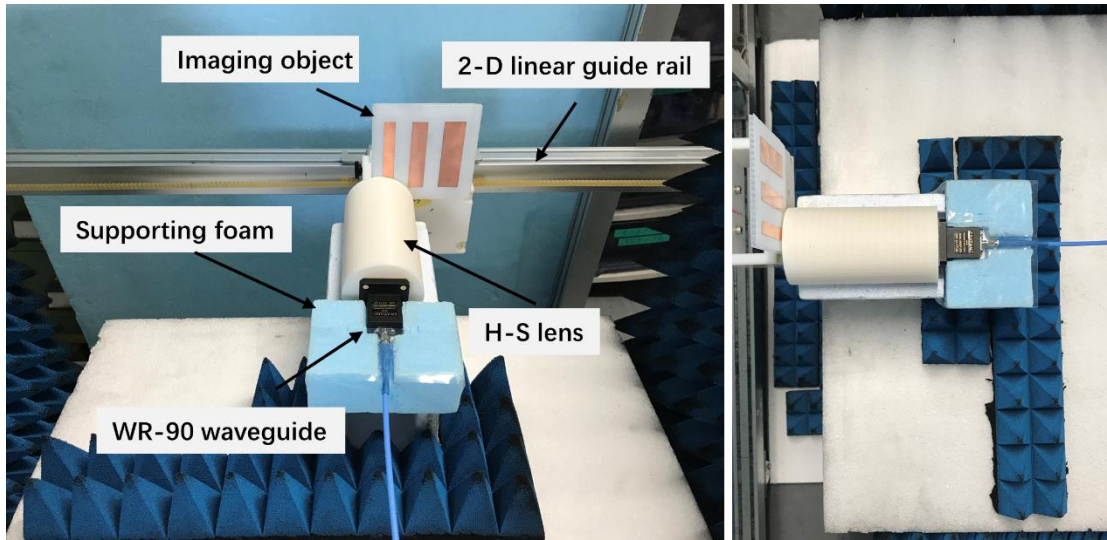
Figure 5-8 Photograph of single-pixel scanning microwave imaging measurement setup by using H-S lens prototype operating at Ka-band.

The imaging object consists of plastic bottom plate and three copper sheets with different physical widths of 10 mm, 15 mm and 20 mm, as shown in Figure 5-9(a). The size of the entire scanning area is 102 mm×102 mm. In our case, the distance of each movement for 2-D linear guide rail is set to 2 mm. In other words, the actual physical distance represented by one pixel is 2mm. Considering the proposed H-S lens operating at the design frequency of 10GHz, the magnitude of the reflection coefficient at this frequency is used for the experimental characterization of the imaging resolution. Figure 5-9 (b) shows the measured magnitude of the reflection coefficient for the imaging object at 10 GHz. Because of a very small focal spot with the theoretical FWHM of 0.45λ at the rear surface of lens, only a small area is illuminated at each measurement point. So, the three copper sheets can be clearly distinguished. Moreover, the measured width of three copper sheets is about 7, 8 and 10 pixels respectively, as illustrated in Figure 5-9 (b). It means that a spatial resolution of ~0.5λ (~15 mm) is achievable with this measurement setup.
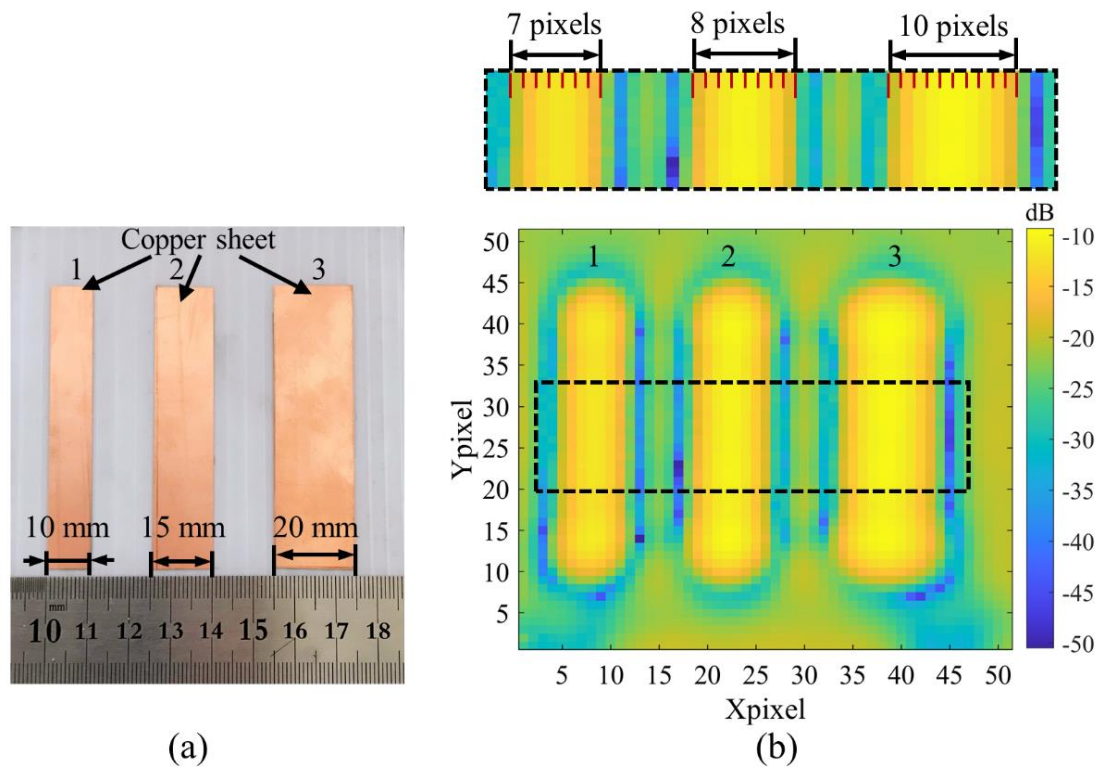
Figure 5-9 (a). The imaging object with different widths (10, 15, 20 mm) of copper sheets and plastic bottom plate. (b). The magnitude of the reflection coefficient for three copper sheets at 10 GHz with width of 7, 8 and 10 pixels (left to right) respectively. Noted that the actual physical distance represented by one pixel is 2mm in this case.

The complete set of measured magnitude of the reflection coefficient at 8.5GHz, 9 GHz, 10 GHz, 11 GHz,12 GHz and 12.5 GHz is presented in Figure 5-10. It can be observed that three copper sheets can be still clearly distinguished, which further demonstrates the certain broadband behavior of the designed lens prototype. Due to the small distance between copper sheets and the effect of plastic bottom plate, the unwanted noise signal can be clearly seen around the imaging object, which causes the slight quality degradation in imaging.
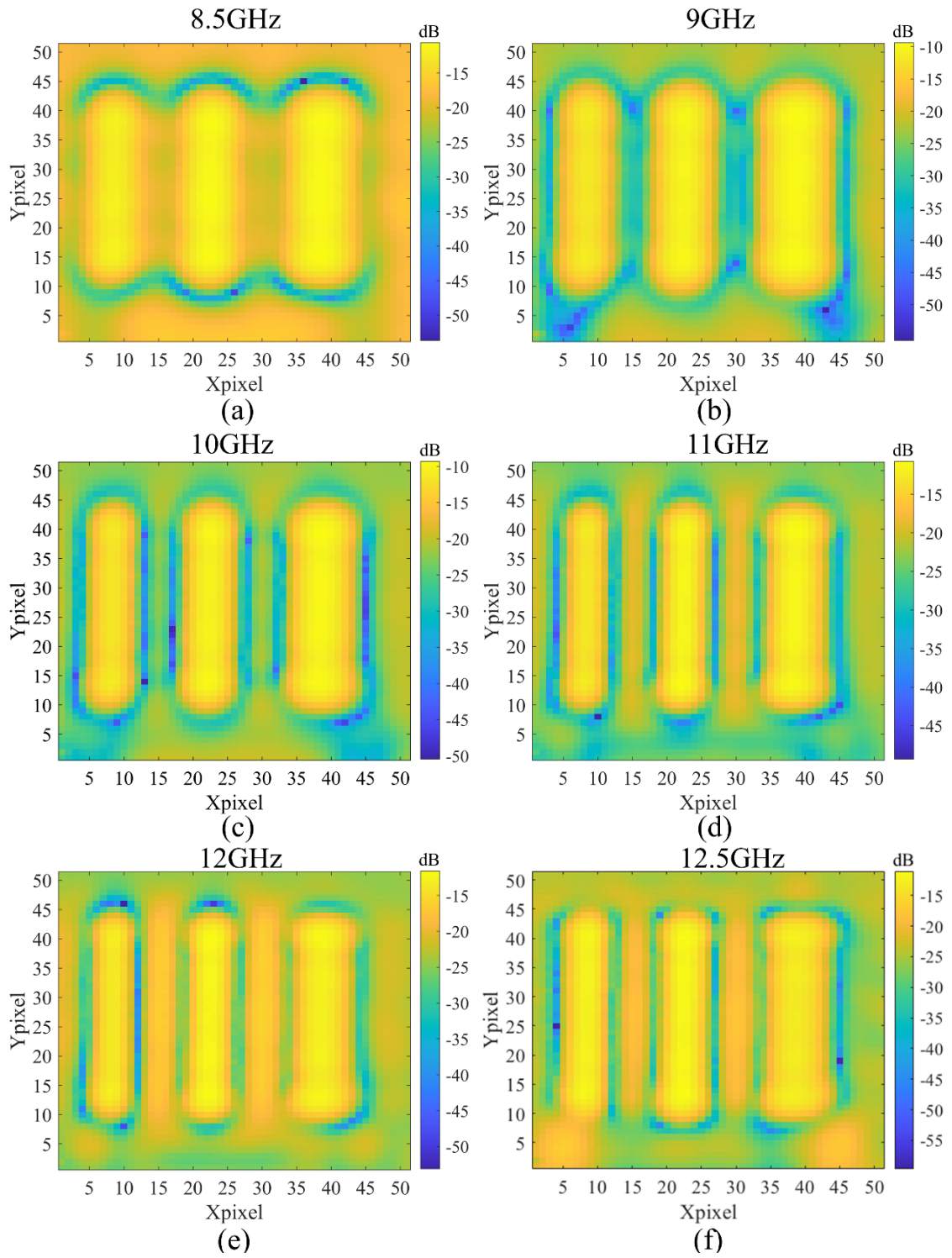
Figure 5-10 The complete set of measured magnitude of the reflection coefficient for three copper sheets at 8.5 GHz, 9 GHz, 10 GHz, 11 GHz,12 GHz and 12.5 GHz respectively.

5.5   Spatial resolution performance of designed H-S lens operating at Ka-band

As the size of the imaging target is further reduced, the effects of unwanted noise caused by small distance between copper sheets and plastic bottom plate on the imaging cannot be ignored. In order to eliminate its interference on high frequency imaging as much as possible, foam absorber material is utilized instead of plastic bottom plate in the spatial resolution imaging experiment at Ka-band. Figure 5-11(a) shows the photograph of imaging object with two copper sheets with different physical widths of 5 mm and 10mm. Here, the size of the entire scanning area is 31 mm×31 mm. The distance of each movement for 2-D linear guide rail is set to 1mm. Similarly, after the electromagnetic waves pass through the designed lens at Ka-band, it can be also concentrated to a subwavelength focusing spot on the imaging object. As illustrated in Figure 5-11 (b), the two copper sheets with measured width of ~6 and ~11pixels are clearly distinguished at the design frequency of 30 GHz, which indicates the spatial resolution of ~0.5λ (~6 mm) for designed lens prototype can be also achieved.

(a)   (b)
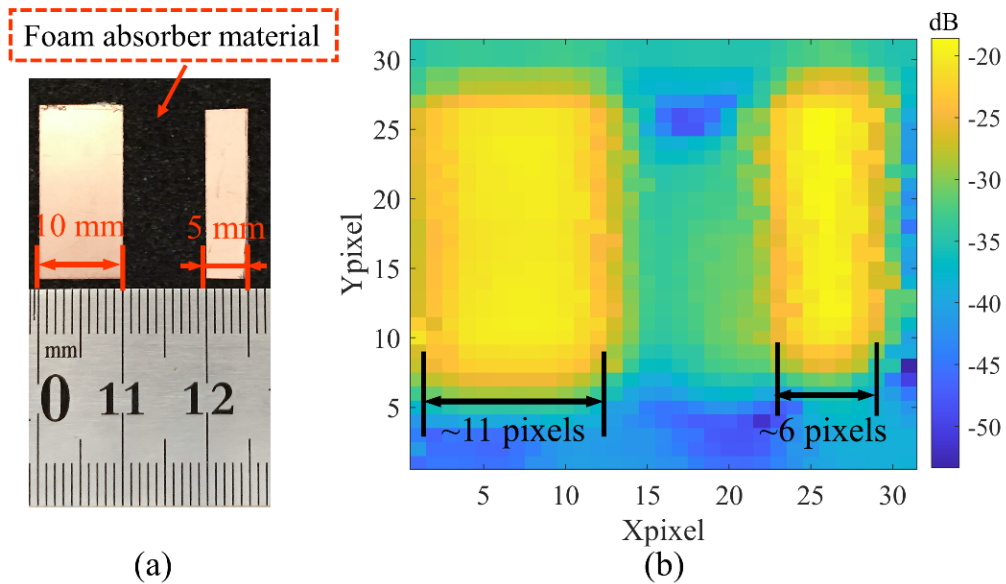
Figure 5-11 (a). The imaging object with different widths (5, 10 mm) of copper sheets. (b). The magnitude of the reflection coefficient for two copper sheets at 30 GHz with width of 6 and 11 pixels respectively. Noted that the actual physical distance represented by one pixel is 1mm in this case.

In addition, owing to the existence of foam absorber material, the interference of unwanted noise signal between two copper sheets is effectively eliminated. The complete set of measured magnitude of the reflection coefficient at 27 GHz, 30 GHz, 33 GHz, 36 GHz, 38 GHz and 40 GHz is respectively given in Figure 5-12. Two copper sheets can be still clearly distinguished at these frequencies, which further demonstrates the proposed lens concept can be applied in higher frequency bands very well. Most importantly, the broadband behavior of the proposed lens can be also maintained.
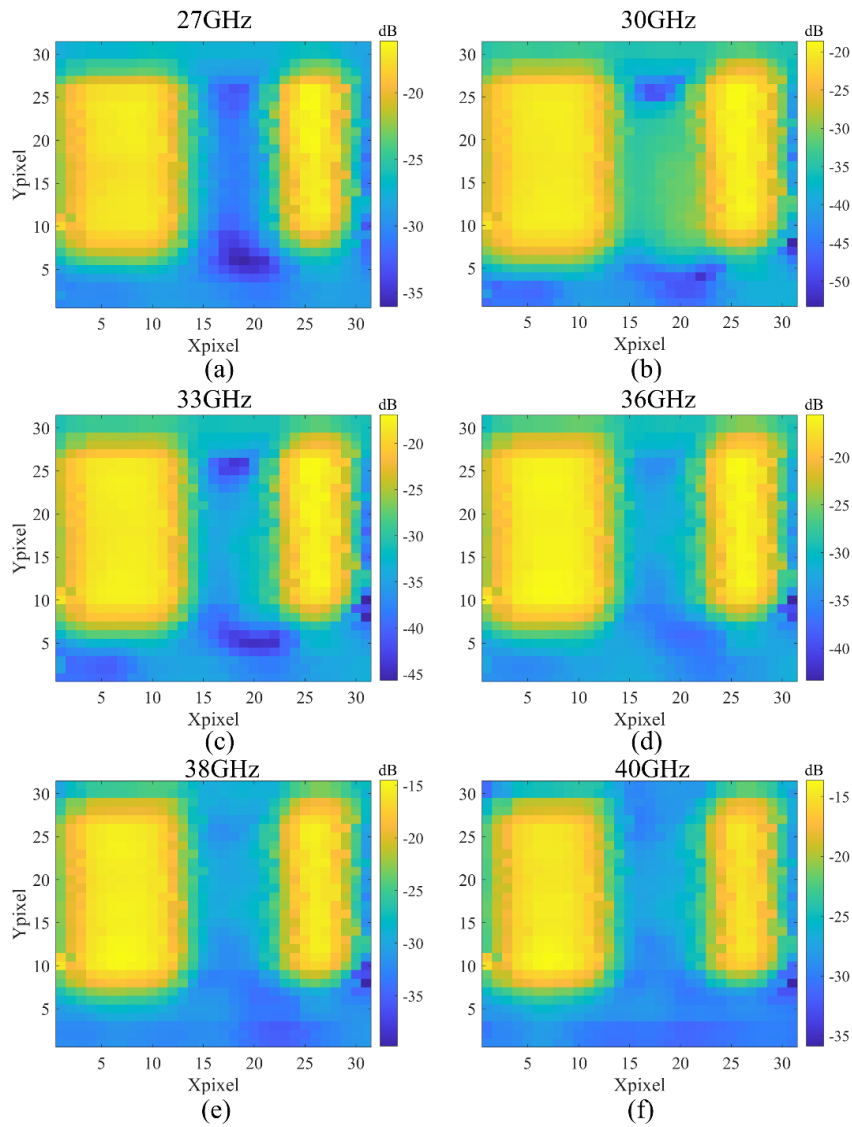
Figure 5-12 The complete set of measured magnitude of the reflection coefficient for three copper sheets at 8.5 GHz, 9 GHz, 10 GHz, 11 GHz,12 GHz and 40 GHz respectively.

5.6 Target Imaging of Letters

To verify the effect of the object's shape and orientation on the imaging system, a Japanese romaji word "TOHOKU" engraved in two single-sided copper clad laminates is utilized, as shown in Figure 5-13 (a) and (b). The linewidth of each letter of the word "TOHOKU" is slightly less than 15 mm. Here, the measured magnitude of the reflection coefficient for the word "TOHOKU" at 8.5 GHz, 10 GHz and 12.5 GHz is measured by using designed lens prototype operating at X-band, as shown in Figure 5-13 (c)-(h). Although the scanning image of "TOHOKU" can be recognized, it suffers from some degree of distortion.
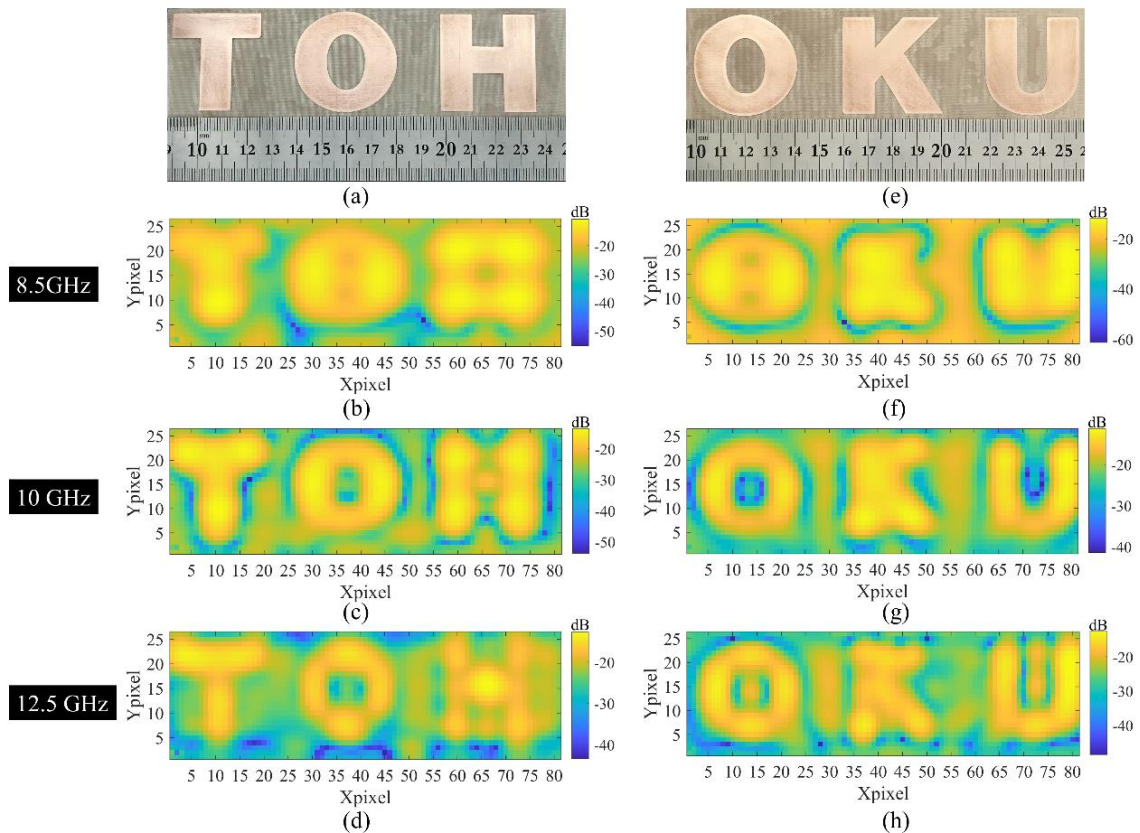
Figure 5-13 (a)-(b). A Japanese romaji word "TOHOKU" engraved in two single-sided copper clad laminate. (c)-(h). The measured magnitude of the reflection coefficient for the word "TOHOKU" at 8.5 GHz, 10 GHz and 12.5 GHz by using designed lens prototype operating at X--band. Noted that the actual physical distance represented by one pixel is 2 mm in this case.

This is mainly attributed to the limited spatial resolution of ~0.5λ (~15 mm) for the lens prototype operating at X-band. Especially, it's different to identify the letters with complex shapes such as "H" and "K". In addition, because of the single-polarization standard waveguide as the microwave receiver, the orientation information of each letter cannot be recorded. which further increases image distortion. However, this phenomenon provides the possibility to enhance the image quality by using multi-polarization information when the size of imaging target is comparable to the spatial resolution.

Figure 5-14 illustrates the measured magnitude of the reflection coefficient for the word "TOHOKU" at 27 GHz, 33 GHz and 40 GHz by using designed lens prototype operating at Ka-band. As mentioned in Section III-C, the spatial resolution of ~0.5λ (~6 mm) for designed lens prototype at the design frequency of 30 GHz can be achieved, which is much smaller than the linewidth of ~15 mm for each letter of the word "TOHOKU". Obviously, as demonstrated in Fig.13 (c)-(h), each letter of the word "TOHOKU" can be recognized perfectly in the scanning image. Although the single-polarization standard waveguide is also utilized as the receiver, the complex shape and different orientation of letters do not have negative effects on imaging quality in this case. It also proves that the a smaller focusing spot size is key to achieve high quality imaging. Overall, the proposed H-S lens prototype exhibits excellent imaging performance with high resolution. The functionality of this lens concept can be also easily expanded to higher frequency bands.
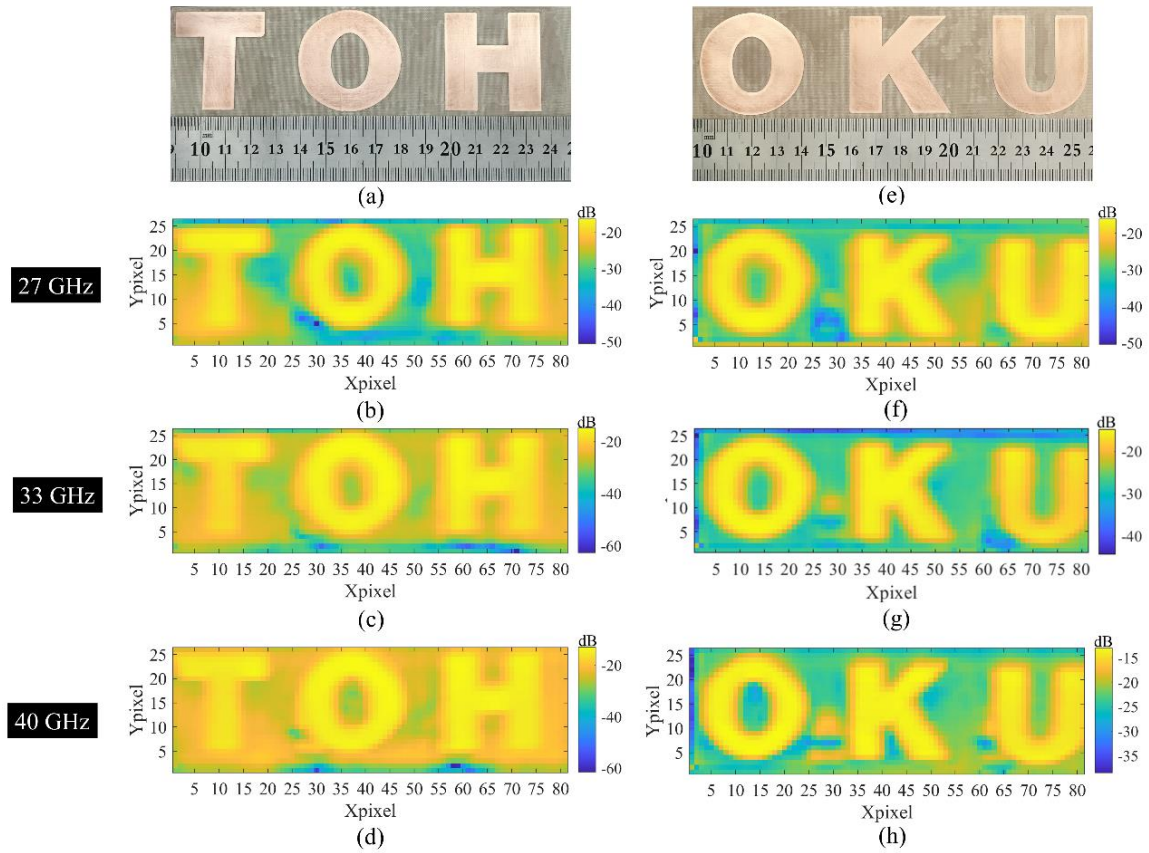
Figure 5-14 (a)-(b). A Japanese romaji word "TOHOKU" engraved in two single-sided copper clad laminate. (c)-(d). The measured magnitude of the reflection coefficient for the word "TOHOKU" at 27 GHz, 33 GHz and 40 GHz by using designed lens prototype operating at Ka-band. Noted that the actual physical distance represented by one pixel is 2 mm in this case.

5.7   Limitation and prospect

As mentioned in Section 5.4, the 2-D image was obtained by moving the imaging object in the horizontal and vertical direction step by step based on time domain measurement method. It means that the scanning imaging speed is very slow, which limits its application in high-speed imaging system. In addition, in order to guarantee the sub-wavelength imaging resolution with surface focusing, the distance between the imaging target and the lens is required to be kept as small as possible. This limits its application in non-contact imaging system. In the following, the possible solutions or ideas to solve these two problems are briefly discussed.

Because the physical aperture of the proposed H-S imaging lens is relatively small, the concept of lens array may provide a possible way to solve the imaging speed problem. Moreover, considering the requirement of the number of imaging sampling points, the method using single waveguide as receiving antenna needs to be changed. As shown in Figure 5-15, The excellent focusing feature can be still obtained reasonably well in a limited range of angles off-axis. In other words, a small array of receiving antenna could be utilized to solve the under-sampling problem. So, the distance between receiving antennas is very critical parameter that should be determined carefully by using the ray tracing method.
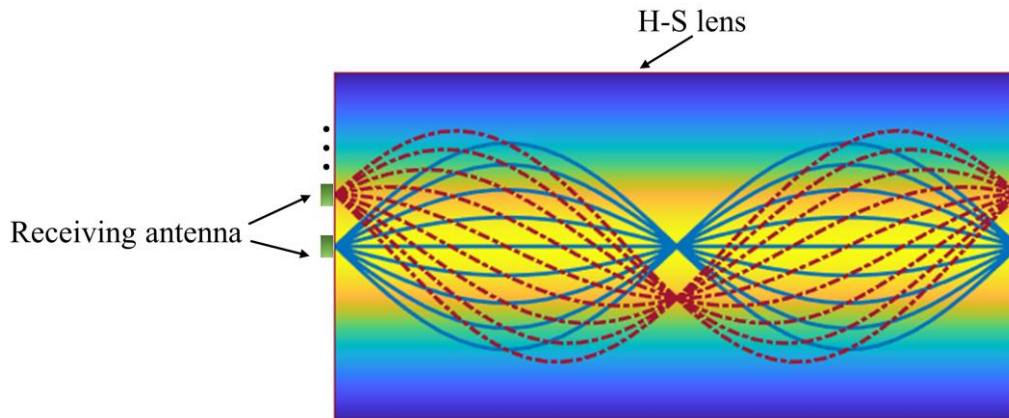
Figure 5-15 The concept of a small array of receiving antenna for H-S imaging lens

For the problem of non-contact imaging, a compound H-S Lens with achromatic characteristic could provide a potential way to solve it as shown in Figure 5-16. This compound H-S lens consists of two lenses. Lens 1 is utilized to achieve the function of converting a spherical wave emitting from a point source into a plane wave. Then, after passing through lens 2, it will be focused on the outside of the lens. However, there is a very important problem to be solved in this compound H-S lens concept. It suffers from obvious spherical aberration, which in turn limits the subwavelength characteristic of focusing. If the refractive index profile of lens 2 could be adjusted to reduce spherical aberration, this compound H-S lens concept could be utilized in the non-contact imaging application.
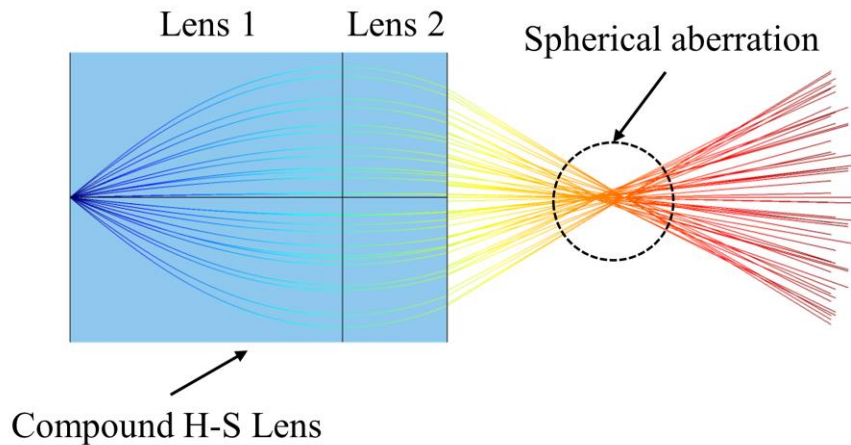
Figure 5-16 The concept of compound H-S lens concept for non-contact imaging application

5.8 Summary

In this chapter, an all-dielectric surface focusing H-S lens operating at 10GHz was proposed to achieve the high resolution focusing with theoretical FWHM around 0.45λ for the single-pixel scanning micro- and millimeter-wave imaging. The realization of proposed h-s lens employs the perforated structure with different air-hole sizes and infill structure with different infill ratios of PLA material by using easily accessible 3D printing technology at a very low cost. Combing ray-tracing analysis and full-wave electromagnetic simulation, the surface focusing properties of subwavelength spot size for designed lens has been validated at X- and Ka-band, revealing the advantage of broad bandwidth. Moreover, based on time domain measurement method, the spatial resolution imaging experiment was carried out to demonstrate the excellent imaging performance for the designed lens prototype with high resolution of $\sim 0.5\lambda$, which revealing great potential for high resolution micro- and millimeter-wave imaging applications. Besides, the functionality of the proposed lens concept can be further expanded to higher frequency bands such as THz by using advanced nanotechnology. The proposed H-S lens concept has great potential to obtain the accurate size and shape information of imaging target with small lens physical aperture.

CHAPTER 6

Conclusion

This thesis work was dedicated to the design, realization and experimental characterization of a high-performance all-dielectric perforated hyperbolic secant gradient index lens with unique structural extensibility for multi-purpose antenna applications. Benefitting from easily accessible 3-D printing, perforated structure with different air-hole sizes can be easily achieved to obtain the desired permittivity profile of GRIN lens, which also enable to maintain broad bandwidth property with simple fabrication process and cost-effectiveness. Furthermore, unlike other well-known GRIN lenses such as Luneburg lens and Maxwell fisheye lens, the proposed hyperbolic secant lens has a unique intrinsic flat shape characteristic. Extra methods or techniques such as TO and QCTO are not required to flatten the particular shape. Most importantly, the structural extensibility of proposed lens concept provides great potential for high directive antenna application, flexible beam-steering application and subwavelength imaging application, which is confirmed by both simulations and measurements in this thesis.

A detailed introduction on different types of lens antenna technologies such as space-fed and integrated fed systems compatible for the applications of wireless communications and imaging was presented in Chapter 1, which has helped identify the possibilities of the interdisciplinary research with optical lens and antenna engineering. It has also highlighted recent advances in lens antenna including traditional homogeneous lens antenna and GRIN lens antennas. Various manufacturing technologies for GRIN lens such as additive manufacturing (3-D printing), foam pressing, PCB milling and metamaterials with metallic resonant will be briefly introduced. Moreover, many GRIN lens antennas tend to be bulky, which require complex TO and QCTO methods to design

flat-shaped lens while maintaining the original electromagnetic performances. The motivation of proposing a new hyperbolic secant lens antenna was provided.

In Chapter 2, the design theory for proposed hyperbolic secant lens based on 2-by-2 ray matrix transfer analysis, and the unique structural extensibility of lens was discussed and explained in detail. The ray matrix transfer analysis provides a very useful analytical method for the study of beam scanning application for H-S lens in Chapter 4. Moreover, the related fabrication methods by using perforated and infill structure for 3-D printing was introduced, which provide a simple and economical way to fabricate H-S lens compared with other manufacturing technologies such as foam pressing, PCB milling and metamaterials with metallic resonant. Besides, in order to realize the broadband lens antenna, a printed antipodal fermi antenna (APFA) with corrugation structure operating at X-band with advantages of broad bandwidth, high gain, and lightweight was verified by full-wave simulation and experiment.

From Chapter 3 to Chapter 5, the multi-purpose antenna applications including high directive application, flexible beam scanning application and super-resolution near-field microwave imaging for proposed hyperbolic secant lens was presented in detail. Specifically speaking, inspired by optical fiber, a new lens antenna type called hyperbolic secant (H-S) lens antenna with high gain and broadband characteristic was proposed for high directive antenna application based on ray tracing analysis and full-wave electromagnetic simulation in Chapter 3. The attractiveness of this new lens is its intrinsic flat shape characteristic and extensibility for different antenna application scenarios, in addition to the advantages of low-profile, lightweight, and high performance. Compared with conventional Luneburg, Maxwell fish-eye, and Eaton lens, the proposed lens has the unique flat shape characteristic, which provides great advantages in designing the low-profile planar lens antenna, avoiding using extremely complex conformal mapping methods. The perforated dielectric material of variable hole sizes is utilized to satisfy the required H-S refractive index distribution. A high gain and wideband printed antipodal fermi antenna as feeding source are employed in the proposed lens antenna prototype operating at 10 GHz. The simulated and experimental results showed good agreement,

demonstrating 23.8 dBi realized gain at 10 GHz with 3-dB beamwidth of 9º and 2-dB fractional realized gain bandwidth of 41.6%. Besides, the total radiation efficiency is above ∼40% across all tested frequencies (8.2 GHz-12.5 GHz), which suggests the proposed H-S lens itself has intrinsic broadband response. Besides, the simplicity and low-cost fabrication of its lens design indicating great potentials in broadband high directive antenna applications.

In addition, the functionality of 2-D beam-scanning for H-S lens was first explored by mechanically moving the waveguide. The beam scanning capability in both the E-and H-plane was confirmed. It has been demonstrated that we can achieve 2-D beam steering in both the E-and H-plane among the effective beam-steering range (±20°) with around 18.9 dBi of realized gain with less than ∼1.2 dB variation and low side-lobe. This proposed lens concept could be also a potential alternative design for the existing planar GRIN lens antenna configurations, avoiding using complex conformal mapping method

In Chapter 4, a beam-switching planar H-S lens antenna concept achieved by switch was proposed to solve the drawbacks of mechanical beam scanning in Chapter 3. The performance of this all-dielectric planar H-S lens for 1-D beam-steering application was first investigated. This new lens concept has its intrinsic flat shape characteristic, which allows for a simple low-cost planar feed technology. Based on ray tracing analysis and full-wave electromagnetic simulation, the performance of proposed lens prototype excited by five rectangular microstrip patch has been evaluated at 10 GHz. The simulated and measured results showed good agreement, demonstrating that we can achieve beam-steering capabilities in H planes from −20° to +20° with around 13.2 dBi of realized gain and SLL (less than −11.5 dB), and up to ±30° with around 10 dBi of realized gain. Moreover, higher steering angles lead to higher phase error resulting from comatic aberration and deterioration of the corresponding radiated beam. Most importantly, the realized gain, efficiency and SLL can be further improved to get better radiation performances by using other 3-D printing materials with lower loss tangent or more advanced manufacturing technology. Due to its intrinsic flat shape characteristic, this

proposed lens concept could be a potential alternative design for developing a low-cost, low profile and easy-to-fabricate beam-switching array antenna for microwave communication applications.

In Chapter 5, the surface high-resolution focusing of proposed hyperbolic secant lens was utilized for the single-pixel scanning near-field microwave imaging. This lens type can achieve the high resolution focusing with theoretical FWHM around 0.45λ. The realization of proposed H-S lens employs the perforated structure with different air-hole sizes and infill structure with different infill ratios of PLA material by using easily accessible 3D printing technology at a very low cost. Combing ray-tracing analysis and full-wave electromagnetic simulation, the surface focusing properties of subwavelength spot size for designed lens has been validated at X- and Ka-band, revealing the advantage of broad bandwidth. Moreover, based on time domain measurement method, the spatial resolution imaging experiment was carried out to demonstrate the excellent imaging performance for the designed lens prototype with high resolution of $\sim 0.5\lambda$, which revealing great potential for high resolution micro- and millimeter-wave imaging applications. Besides, the functionality of the proposed lens concept can be further expanded to higher frequency bands such as THz by using advanced nanotechnology. The proposed H-S lens concept has great potential to obtain the accurate size and shape information of imaging target with small lens physical aperture.

In summary, challenges for designing high-performance all-dielectric perforated hyperbolic secant lens antenna with unique structural extensibility for multi-purpose antenna applications by using easily accessible 3D printing in a very low-cost were analyzed and addressed in this dissertation, which will greatly contribute in the field of the lens antenna with enhanced performance and expanded functionalities.

APPENDIX A
Associated Publications

Journal Papers:

1. Wenyi Shao, Hiroyasu Sato, Xiaotong Li, Kevin Kipruto Mutai, and Qiang Chen, "Perforated extensible 3-D hyperbolic secant lens antenna for directive antenna applications using additive manufacturing," *Opt. Express* vol. 29, no. 12, pp. 18932-18949, Jun. 2021.

2. **Wenyi Shao** and Qiang Chen, "Performance analysis of an all-dielectric planar Mikaelian lens antenna for 1-D beam-steering application," Opt. Express vol. 29, no. 18, pp. 29202-29214, Aug. 2021.

3. **Wenyi Shao** and Qiang Chen, "2-D Beam-Steerable Generalized Mikaelian Lens with Unique Flat-Shape Characteristic," *IEEE Antennas Wireless Propag. Lett.*, vol. 20, no. 10, pp. 2033-2037, Aug. 2021.

4. **Wenyi Shao** and Qiang Chen, "Single-pixel Scanning Micro-/Millimeter-wave Imaging with Subwavelength Resolution Using Surface Focusing Mikaelian Lens," *IEEE Trans. Antennas Propag.*, (Under review)

Conference Papers:

1. **Wenyi Shao** and Qiang Chen, "A Novel Planar Perforated Hyperbolic Secant Lens Antenna for Milli-Wave Applications," 2021 International Symposium on Antennas and Propagation (ISAP), 2021, pp. 1-2

APPENDIX B
Specific Design Files

1. The geometry size of the bottom of APFA.

APFA_Bottom

Drawing 1

A4

mm

Dimension labels visible in the drawing: 6.00, 0.80, 0.80, 160.00, 5.00, R20.00, 20.00, R20.00, 42.00
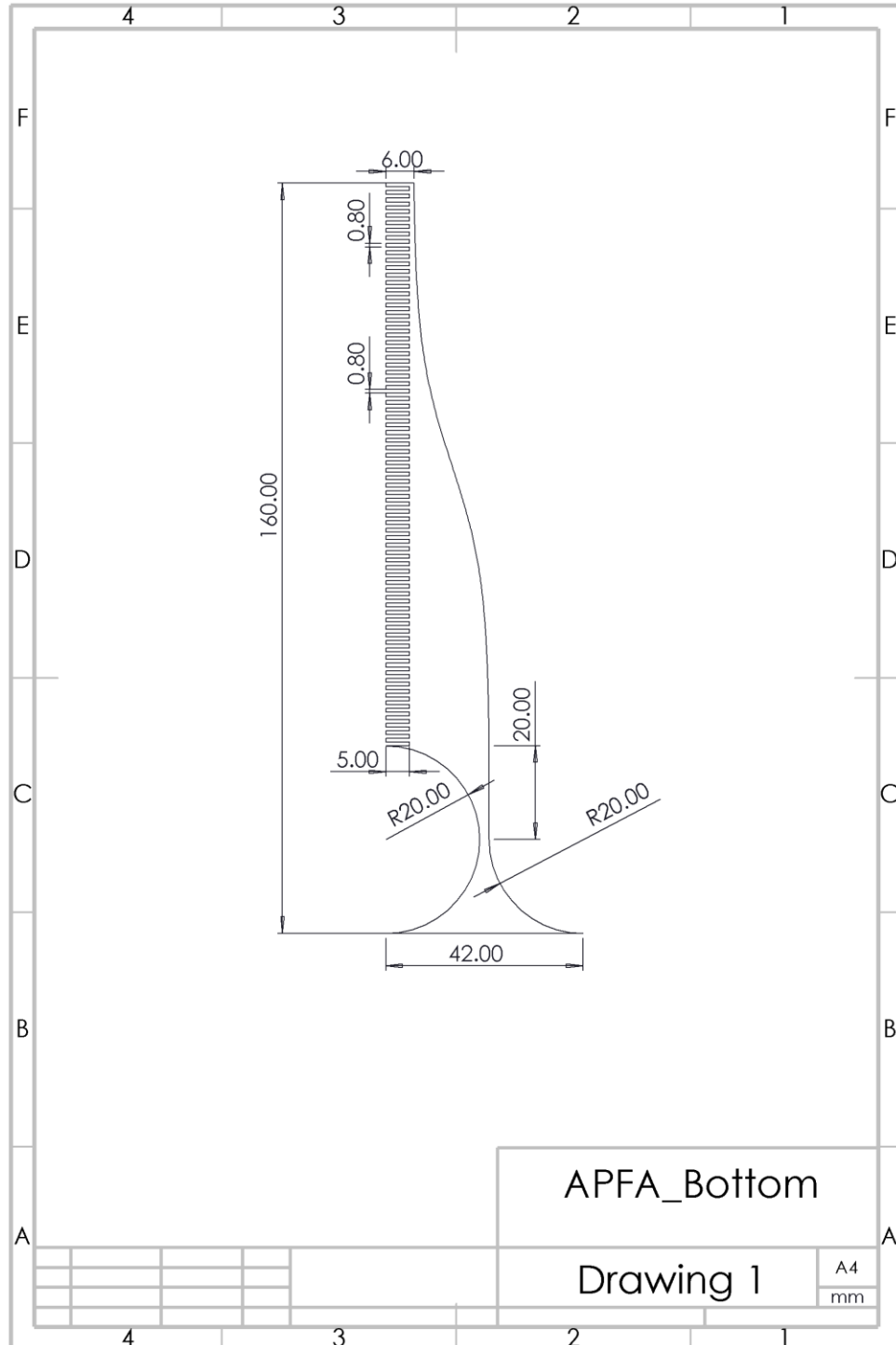
2. The geometry size of the top of APFA.

APFA_TOP

Drawing 1

A4

mm
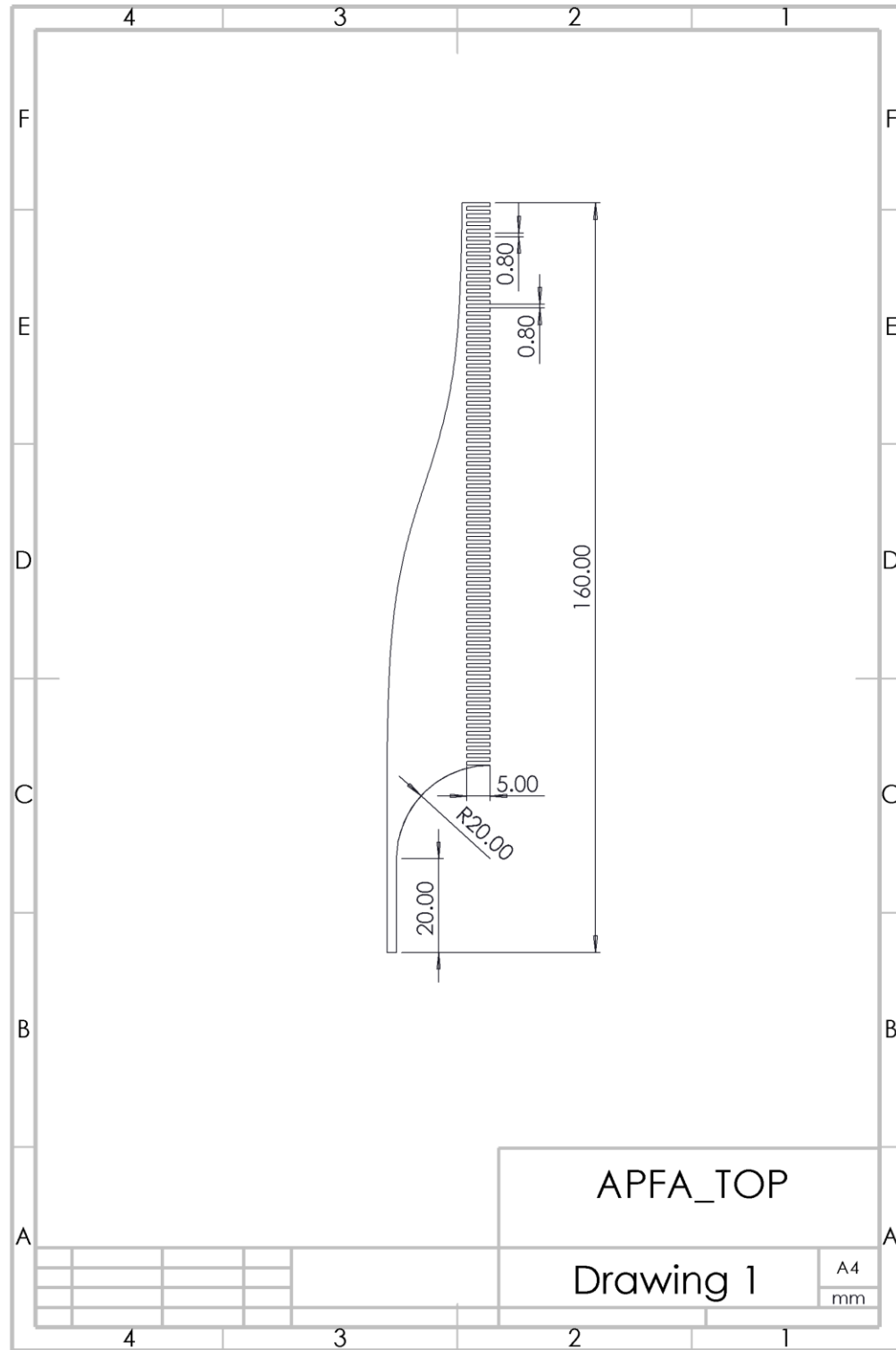
3. The geometry size of surface imaging Mikaelian lens at 10 GHz.

4. The geometry size of planar Mikaelian lens antenna for 1-D beam-steering.

5. The geometry size of planar Mikaelian lens antenna for directive antenna applications.
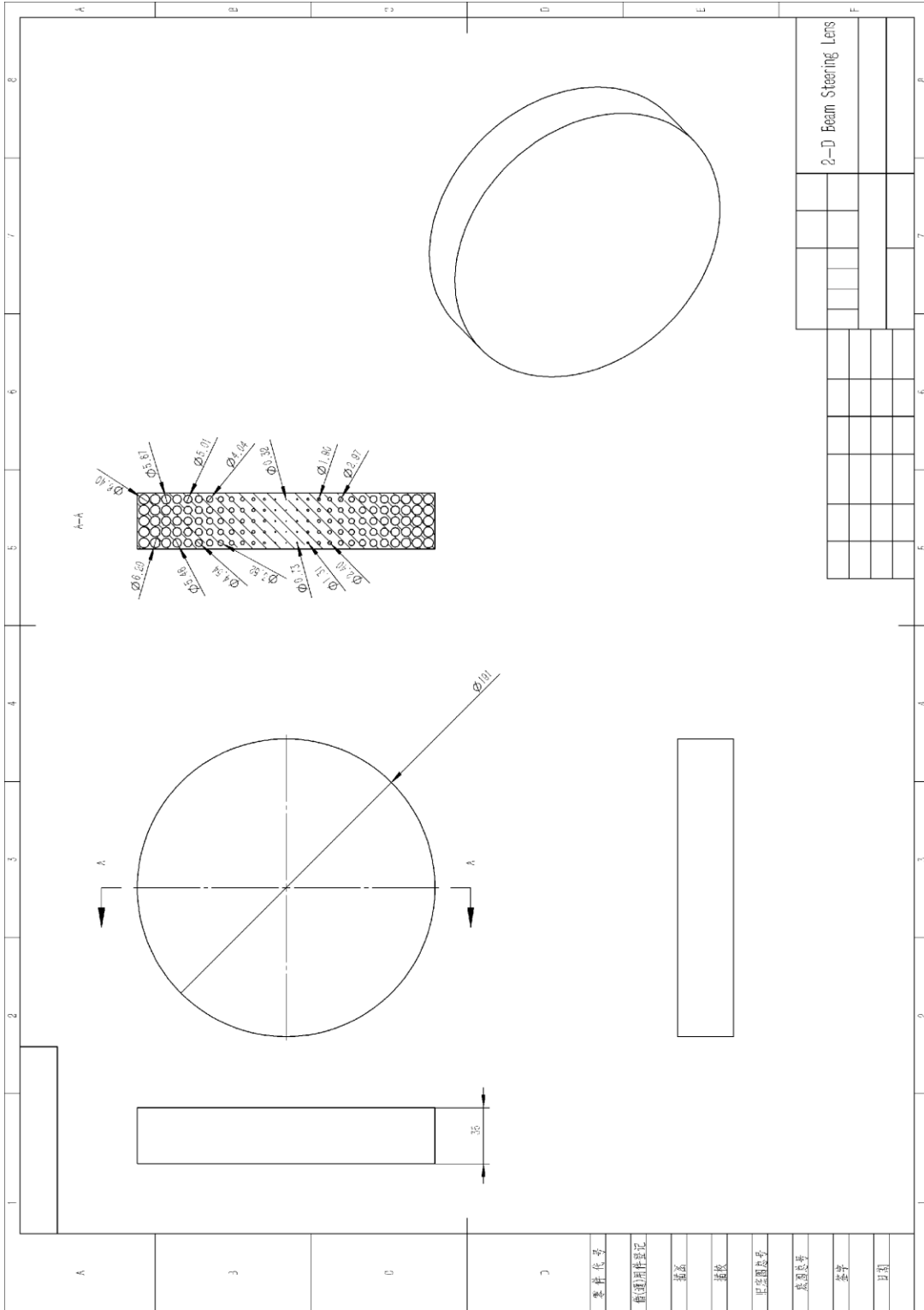
APPENDIX C
Fresnel Lens Designer

This appendix contains the demo of Fresnel Lens Designer and core source code. The following figure shows an example of design process of Fresnel Lens. The specific design parameters can be seen in the figure. Moreover, this demo can be also used to design other types of lenses. However, because of the limited time, some functions are not perfect enough.

APPENDIX D
Core Source Code for Designing the Fresnel lens

This appendix contains the core source code for designing the Fresnel lens.

% fresnel_zone.m

```
clc
clear

%Design style 1
N=2; %number of full-wave zones
P=4; %number of subzones
F=152.2e-3; %focal length
T=10;
t=3.66;    %length of base

%{
%Design style 2
N=11; %number of full-wave zones
P=6; %number of subzones
F=688.2e-3; %focal length
T=0;
t=3.7;    %length of base
%}

lamada=4e-3;
epsilon=2.34;
for n=1:N*P
r(n)=sqrt((n*lamada/P)^2+2*n*F*lamada/P);
R(n)=r(n)*1000;
end
d=1000*lamada/(P*(sqrt(epsilon)-1));
s=(P-1)*d;
T=t+s;
xmax_new=zone_above(d,P,N,R)
xmin_new=zone_below(d,P,N,R)

base(P,d,t,xmax_new,xmin_new)
```

% zone_above.m

```
function xmax_new=zone_above(d,P,N,R)
  dmax=[];
  hold on
  axis equal
for ii=1:N*P
  if ii==1
  plot([0+(ii-1)*d 0+(ii-1)*d],[0 R(ii)],'b')
  else
  plot([0+rem(1-ii,P)*d 0+rem(1-ii,P)*d],[R(ii-1) R(ii)],'b')
  end
  pause(0.5)
```

```matlab
  if ii==N*P
  continue
  else
  plot([0-d*rem(ii,P) 0+rem(1-ii,P)*d],[R(ii) R(ii)],'b')
  end
  pause(0.5)

 dmax=mod(ii,P)*d;
end
xmax_new=R(ii);
```

% zone_below.m

```matlab
function xmin_new=zone_below(d,P,N,R)
  dmax=[];
  hold on
  axis equal
for ii=1:N*P
  if ii==1
  plot([0+(ii-1)*d 0+(ii-1)*d],[0 0-R(ii)],'b')
  else
  plot([0+rem(1-ii,P)*d 0+rem(1-ii,P)*d],[0-R(ii-1) 0-R(ii)],'b')
  end
  pause(0.3)
  if ii==N*P
  continue
  else
  plot([0-d*rem(ii,P) 0+rem(1-ii,P)*d],[0-R(ii) 0-R(ii)],'b')
  end
  pause(0.3)

 dmax=mod(ii,P)*d;
end
xmin_new=(-1)*R(ii);
```

% base.m
```matlab
function base(P,d,t,xmax_new,xmin_new)
  plot([(1-P)*d (1-P)*d-t],[xmax_new,xmax_new],'b')
  plot([(1-P)*d-t (1-P)*d-t],[xmax_new,xmin_new],'b')
  plot([(1-P)*d-t (1-P)*d],[xmin_new,xmin_new],'b')
```

Ray Tracing for X-band H-S lens with Surface Focusing

This appendix contains the core source code for ray tracing in Chapter 5.

```matlab
clc
clear
close all

%Initial parameter setting
n_PLA = 1.6733;                         %The refractive index of PLA
material
pitch = 0.5;                            %The pitch of designed Mikaelian
lens operating at X-band
length = 133;                           %The length of designed Mikaelian
lens operating at X-band (Unit:mm).
diameter = 70;                          %The diameter of designed Mikaelian
lens operating at X-band (Unit:mm).
x_pos = 0;                              %The initial position of rays
(Unit:mm).

%The gradient of Mikaelian lens
gradient=2* pi * pitch / length;
alpha = gradient;

z_0 = linspace(0,length,140);
x_0=linspace(-diameter/2,diameter/2,140);
[Z_0,X_0] = meshgrid(z_0,x_0);
%The refractive index of Mikaelian lens
refractive_index_lens = n_PLA^2 ./cosh(alpha*X_0).^2;
%The permittivity of Mikaelian lens
permittivity_lens=refractive_index_lens.^2;

% Display matrix data of the permittivity of Mikaelian lens
[row_layer,column_layer] = size(permittivity_lens);
s=pcolor(Z_0,X_0,permittivity_lens);
shading interp;
xlabel('z (mm)')
ylabel('x (mm)')
hold on

% The launch angle range of rays
max_angle=n_PLA * sqrt(1 - cosh(diameter * pitch * pi / length)^(-2));
angles = linspace(-max_angle,max_angle,19);
angle_range = asin(sin(angles/n_PLA));

% The exit distance
z_end=linspace(length,length+30,10);
r_end=[];
```

```matlab
% Describe rays passing through Mikaelian lens
for angle_n = 1:19
    [z,x,p_end] = ray_transfer_matrix(n_PLA,gradient,length, x_pos,
angle_range(angle_n),40);
    x_end=p_end(1)+p_end(2)*(z_end-length);
    % the ray trajectory (z,x)
    z = [z, z_end];
    x = [x, x_end];
    plot(z,x,'Color','#D95319','LineWidth' ,1)
end

axis([0 160 -60 60])
ax = gca;
ax.FontName = 'Times New Roman';
ax.FontSize = 18;
grid on
box on




function [z, x_p,p_end]=ray_transfer_matrix(n_PLA,gradient,length, x_i,
theta_i, n_points)
% Return arrays describing rays passing through Mikaelian lens
z = linspace(0, length, n_points);
input_matrix = [x_i; n_PLA * cos(pi / 2 - theta_i)];
xp_z=[];
for i = 1:n_points
    % 2-by-2 ray transfer matrix (ABCD)  for rays propagation inside
Mikaelian lens .
    ABCD = [cos(gradient * z(i)), sin(gradient * z(i)) / gradient /
n_PLA;-n_PLA * gradient * sin(gradient * z(i)), cos(gradient * z(i))];

    xp_z = [xp_z,ABCD*input_matrix];
end
x_p=xp_z(1,:);
p_end=[xp_z(1,end);xp_z(2,end)];
end
```

REFERENCES

[1] S. Hähnle et al., "An Ultrawideband Leaky Lens Antenna for Broadband Spectroscopic Imaging Applications," in IEEE Transactions on Antennas and Propagation, vol. 68, no. 7, pp. 5675-5679, July 2020.

[2] Seokwon Yeom, Dong-Su Lee, YuShin Jang, Mun-Kyo Lee, and Sang-Won Jung, "Real-time concealed-object detection and recognition with passive millimeter wave imaging," Opt. Express 20, 9371-9381 (2012).

[3] S. Liao et al., "Passive Millimeter-Wave Dual-Polarization Imagers," in IEEE Transactions on Instrumentation and Measurement, vol. 61, no. 7, pp. 2042-2050, July 2012.

[4] X. Gao, L. Dai, S. Han, I Chin-Lin, and X Wang, "Reliable Beamspace Channel Estimation for Millimeter-Wave Massive MIMO Systems with Lens Antenna Array," IEEE Trans. Wireless Commun. 16(9), 6010–6021 (2017).

[5] M. Karabacak, H. Arslan and G. Mumcu, "Lens Antenna Subarrays in mmWave Hybrid MIMO Systems," in IEEE Access, vol. 8, pp. 216634-216644, 2020.

[6] M. Kokkonen, S. Myllymäki and H. Jantunen, "3×3 Dipole lens antenna at 300 GHz with different permittivity lenses," 2020 2nd 6G Wireless Summit (6G SUMMIT), 2020, pp. 1-4,.

[7] K. Medrar et al., "H-Band Substrate-Integrated Discrete-Lens Antenna for High Data Rate Communication Systems," in IEEE Transactions on Antennas and Propagation, vol. 69, no. 7, pp. 3677-3688, July 2021.

[8] N. Chudpooti, N. Duangrit, S. Chudpooti, P. Akkaraekthalin, I. D. Robertson and N. Somjit, "THz Photo-Polymeric Lens Antennas for Potential 6G Beamsteering Frontend," 2021 International Symposium on Antennas and Propagation (ISAP), 2021, pp. 1-2.

[9] M. K. Saleem, H. Vettikaladi, M. A. S. Alkanhal and M. Himdi, "Lens Antenna for Wide Angle Beam Scanning at 79 GHz for Automotive Short Range Radar

Applications," in IEEE Transactions on Antennas and Propagation, vol. 65, no. 4, pp. 2041-2046, April 2017

[10] B. Zhang et al., "A Two-Dimensional Multibeam Lens Antenna for Hydrologic Radar Application," in IEEE Antennas and Wireless Propagation Letters, vol. 18, no. 12, pp. 2488-2492, Dec. 2019.

[11] Z. Cai, Y. Zhou, Y. Qi, W. Zhuang and L. Deng, "A Millimeter Wave Dual-Lens Antenna for IoT-Based Smart Parking Radar System," in IEEE Internet of Things Journal, vol. 8, no. 1, pp. 418-427, 1 Jan.1, 2021.

[12] Y. J. Cho, G. Suk, B. Kim, D. K. Kim and C. Chae, "RF Lens-Embedded Antenna Array for mmWave MIMO: Design and Performance," in IEEE Communications Magazine, vol. 56, no. 7, pp. 42-48, July 2018.

[13] A. Artemenko, A. Mozharovskiy, A. Sevastyanov, V. Ssorin and R. Maslennikov, "Electronically beam steerable lens antenna for 71–76/81–86 GHz backhaul applications," 2015 IEEE MTT-S International Microwave Symposium, 2015, pp. 1-4.

[14] J. Ala-Laurinaho et al., "2-D Beam-Steerable Integrated Lens Antenna System for 5G E-Band Access and Backhaul," in IEEE Transactions on Microwave Theory and Techniques, vol. 64, no. 7, pp. 2244-2255, July 2016.

[15] H. Sato et al., "Development of 77 GHz millimeter wave passive imaging camera," SENSORS, 2009 IEEE, 2009, pp. 1632-1635.

[16] Yayun Cheng, Lingbo Qiao, Dong Zhu, Yingxin Wang, and Ziran Zhao, "Passive polarimetric imaging of millimeter and terahertz waves for personnel security screening," Opt. Lett. 46, 1233-1236 (2021).

[17] B. Schoenlinner, Xidong Wu, J. P. Ebling, G. V. Eleftheriades and G. M. Rebeiz, "Wide-scan spherical-lens antennas for automotive radars," in IEEE Transactions on Microwave Theory and Techniques, vol. 50, no. 9, pp. 2166-2175, Sept. 2002.

[18] J. R. Sanford, "Scattering by spherically stratified microwave lens antennas," in IEEE Transactions on Antennas and Propagation, vol. 42, no. 5, pp. 690-698, May 1994.

[19] Z. Briqech, A. Sebak and T. A. Denidni, "Wide-Scan MSC-AFTSA Array-Fed Grooved Spherical Lens Antenna for Millimeter-Wave MIMO Applications," in IEEE Transactions on Antennas and Propagation, vol. 64, no. 7, pp. 2971-2980, July 2016.

[20] Z. Sipus, N. Burum and I. Vilovic, "Analysis of Spherical Lens Antennas using Spectral Domain Approach," The Second European Conference on Antennas and Propagation, EuCAP 2007, 2007, pp. 1-5.

[21] K. X. Wang and H. Wong, "Design of a Wideband Circularly Polarized Millimeter-Wave Antenna with an Extended Hemispherical Lens," in IEEE Transactions on Antennas and Propagation, vol. 66, no. 8, pp. 4303-4308, Aug. 2018.

[22] Improvement of the Scanning Performance of the Extended Hemispherical Integrated Lens Antenna Using a Double Lens Focusing System," in IEEE Transactions on Antennas and Propagation, vol. 64, no. 8, pp. 3698-3702, Aug. 2016.

[23] A. Karttunen, J. Ala-Laurinaho, R. Sauleau and A. V. Räisänen, "Extended hemispherical integrated lens antenna with feeds on a spherical surface," 2013 7th European Conference on Antennas and Propagation (EuCAP), 2013, pp. 2539-2543.

[24] D. F. Filipovic, S. S. Gearhart and G. M. Rebeiz, "Double-slot antennas on extended hemispherical and elliptical silicon dielectric lenses," in IEEE Transactions on Microwave Theory and Techniques, vol. 41, no. 10, pp. 1738-1749, Oct. 1993.

[25] A. Bisognin et al., "A 120 GHz 3D-printed plastic elliptical lens antenna with an IPD patch antenna source," 2014 IEEE International Conference on Ultra-WideBand (ICUWB), 2014, pp. 171-174.

[26] L. Xue and V. Fusco, "Patch Fed Planar Dielectric Slab Extended Hemi-Elliptical Lens Antenna," in IEEE Transactions on Antennas and Propagation, vol. 56, no. 3, pp. 661-666, March 2008.

[27] A. Papathanasopoulos, Y. Rahmat-Samii, N. C. Garcia and J. D. Chisum, "A Novel Collapsible Flat-Layered Metamaterial Gradient-Refractive-Index Lens Antenna," in IEEE Transactions on Antennas and Propagation, vol. 68, no. 3, pp. 1312-1321, March 2020.

[28] J. R. Costa, E. B. Lima and C. A. Fernandes, "Compact Beam-Steerable Lens Antenna for 60-GHz Wireless Communications," in IEEE Transactions on Antennas and Propagation, vol. 57, no. 10, pp. 2926-2933, Oct. 2009.

[29] Ma, H., Cui, T. Three-dimensional broadband and broad-angle transformation-optics lens. Nat Commun 1, 124 (2010).

[30] B. Fuchs, L. Le Coq, O. Lafond, S. Rondineau and M. Himdi, "Design Optimization of Multishell Luneburg Lenses," in IEEE Transactions on Antennas and Propagation, vol. 55, no. 2, pp. 283-289, Feb. 2007.

[31] A. Dhouibi, S. N. Burokur, A. de Lustrac and A. Priou, "Compact Metamaterial-Based Substrate-Integrated Luneburg Lens Antenna," in IEEE Antennas and Wireless Propagation Letters, vol. 11, pp. 1504-1507, 2012.

[32] A. Sayanskiy, S. Glybovski, V. P. Akimov, D. Filonov, P. Belov and I. Meshkovskiy, "Broadband 3-D Luneburg Lenses Based on Metamaterials of Radially Diverging Dielectric Rods," in IEEE Antennas and Wireless Propagation Letters, vol. 16, pp. 1520-1523, 2017.

[33] Z. L. Mei, J. Bai, T. M. Niu and T. J. Cui, "A Half Maxwell Fish-Eye Lens Antenna Based on Gradient-Index Metamaterials," in IEEE Transactions on Antennas and Propagation, vol. 60, no. 1, pp. 398-401, Jan. 2012.

[34] B. Fuchs, O. Lafond, S. Rondineau, M. Himdi and L. L. Coq, "Off-Axis Performances of Half Maxwell Fish-Eye Lens Antennas at 77 GHz," in IEEE Transactions on Antennas and Propagation, vol. 55, no. 2, pp. 479-482, Feb. 2007.

[35] Y. Shi, K. Li, J. Wang, L. Li and C. -H. Liang, "An Etched Planar Metasurface Half Maxwell Fish-Eye Lens Antenna," in IEEE Transactions on Antennas and Propagation, vol. 63, no. 8, pp. 3742-3747, Aug. 2015.

[36] G. Du, M. Liang, R. A. Sabory-Garcia, C. Liu and H. Xin, "3-D Printing Implementation of an X-band Eaton Lens for Beam Deflection," in IEEE Antennas and Wireless Propagation Letters, vol. 15, pp. 1487-1490, 2016.

[37] J. Y. Li and M. Ng Mou Kehn, "The 90° Rotating Eaton Lens Synthesized by Metasurfaces," in IEEE Antennas and Wireless Propagation Letters, vol. 17, no. 7, pp. 1247-1251, July 2018.

[38] A. Dhouibi, S. N. Burokur, A. de Lustrac and A. Priou, "X-band metamaterial-based Luneburg lens antenna," 2013 IEEE Antennas and Propagation Society International Symposium (APSURSI), 2013, pp. 1292-1293.

[39] H. Xu, G. Wang, Z. Tao and T. Cai, "An Octave-Bandwidth Half Maxwell Fish-Eye Lens Antenna Using Three-Dimensional Gradient-Index Fractal Metamaterials," in IEEE Transactions on Antennas and Propagation, vol. 62, no. 9, pp. 4823-4828, Sept. 2014.

[40] J. Bor, O. Lafond, B. Fuchs, H. Merlet, P. Le Bars and M. Himdi, "Light and cheap flat foam-based Luneburg lens antenna," The 8th European Conference on Antennas and Propagation (EuCAP 2014), 2014.

[41] Y. -H. Lou, Y. -X. Zhu, G. -F. Fan, W. Lei, W. -Z. Lu and X. -C. Wang, "Design of Ku-Band Flat Luneburg Lens Using Ceramic 3-D Printing," in IEEE Antennas and Wireless Propagation Letters, vol. 20, no. 2, pp. 234-238, Feb. 2021.

[42] S. Zhang, Y. Vardaxoglou, W. Whittow and R. Mittra, "3D-printed graded index lens for RF applications," 2016 International Symposium on Antennas and Propagation (ISAP), 2016, pp. 90-91.

[43] Y. Li and Q. Zhu, "Luneburg lens with extended flat focal surface for electronic scan applications," Opt. Express 24(7), 7201–7211 (2016).

[44] B. Fuchs, O. Lafond, S. Rondineau, and M. Himdi, "Design and characterization of half Maxwell fish-eye lens antennas in millimeter waves," IEEE Trans. Microw. Theory Techn. 54(6), 2292–2300 (2006).

[45] Y. Su and Z. N. Chen, "A Flat Dual-Polarized Transformation-Optics Beamscanning Luneburg Lens Antenna Using PCB-Stacked Gradient Index Metamaterials," in IEEE Transactions on Antennas and Propagation, vol. 66, no. 10, pp. 5088-5097, Oct. 2018。

[46] B. Arigong, J. Shao, H. Ren, R. Zhou, H. S. Kim, Y. Lin, and H. Zhang, "Flattened generalized luneburg lens via quasi-conformal mapping," in IEEE Antennas and Propagation Society International Symposium (APSURSI) (2013), pp. 1902–1903.

[47] S. Jain, M. Abdel-Mageed and R. Mittra, "Flat-Lens Design Using Field Transformation and Its Comparison with Those Based on Transformation Optics and Ray Optics," in IEEE Antennas and Wireless Propagation Letters, vol. 12, pp. 777-780, 2013.

[48] A. Omar, "Baseband and Super-Resolution-Passband Reconstructions in Microwave Imaging," in IEEE Transactions on Microwave Theory and Techniques, vol. 67, no. 4, pp. 1327-1335, April 2019.

[49] A. L. Mikaelian. Application of stratified medium for waves focusing. Doklady Akademii Nauk SSSR, 81:569–571, 1951.

[50] A. Mikaelian and A. Prokhorov, "V Self-Focusing Media with Variable Index Of Refraction," Prog. Opt. 17, 279–345 (1980).

[51] Bass, Michael, ed. 2010. Handbook of Optics: Volume I - Geometrical and Physical Optics, Polarized Light, Components and Instruments. 3rd ed. New York: McGraw-Hill Professional.

[52] P. A. Bélanger, "Beam propagation and the ABCD ray matrices," Opt. Lett. 16, 196-198 (1991).

[53] Valérie Pineau Noël, Shadi Masoumi, Elahe Parham, Gabriel Genest, Ludovick Bégin, Marc-André Vigneault, and Daniel C. Côté "Tools and tutorial on practical ray tracing for microscopy," Neurophotonics 8(1), 010801 (21 January 2021).

[54] J. Bor, B. Fuchs, O. Lafond, and M. Himdi, "Flat foam-based Mikaelian lens antenna for millimeter wave applications," in 44th European Microwave Conference (2014), pp. 1640–1643.

[55] F. Maggiorelli, A. Paraskevopoulos, J. C. Vardaxoglou, M. Albani, and S. Maci, "Profile Inversion and Closed Form Formulation of Compact GRIN Lenses," IEEE Open J. Antennas Propag. 2, 315–325 (2021).

[56] C. Gomez-Reino, M. V. Perez, and C. Bao, Gradient-Index Optics: Fundamentals and Applications. (Springer, 2002), pp. 128–131.

[57] K. Nishizawa, "Principle and application on gradient index optical imaging," Rev. Laser Eng. 8(5), 748–758 (1980).

[58] M. W. Elsallal, J. Hood, I. McMichael, and T. Busbee, "3D Printed Material Characterization for Complex Phased Arrays and Metamaterials," Microw. J. 59(10), 20–34 (2016).

[59] T. Hayat, M. U. Afzal, A. Lalbakhsh, and K. P. Esselle, "Additively Manufactured Perforated Superstrate to Improve Directive Radiation Characteristics of Electromagnetic Source," IEEE Access 7, 153445–153452 (2019).

[60] S. Zhang, R. K. Arya, S. Pandey, Y. Vardaxoglou, W. Whittow, and R. Mittra, "3D-printed planar graded index lenses," IET Microw., Antennas Propag., vol. 10, no. 13, pp. 1411–1419, 2016.

[61] Pourahmadazar, J., Denidni, T.A. Towards Millimeter-wavelength: Transmission-Mode Fresnel-Zone Plate Lens Antennas using Plastic Material Porosity Control in Homogeneous Medium. Sci Rep 8, 5300 (2018).

[62] C. Mateo-Segura, A. Dyke, H. Dyke, S. Haq, and Y. Hao, "Flat Luneburg Lens via Transformation Optics for Directive Antenna Applications," IEEE Trans. Antennas Propag. 62(4), 1945–1953 (2014).

[63] H. Sato, Y. Takagi, and K. Sawaya, "High Gain Antipodal Fermi Antenna with Low Cross Polarization," IEICE Trans. Commun. E94-B(8), 2292–2297 (2011).

[64] Y. T. Lo and S. W. Lee, "Antenna Handbook: theory, applications, and design," Springer, 16–19 (2013).

[65] S. Sahin, N. K. Nahar, and K. Sertel, "Dielectric properties of low-loss polymers for mmW and THz applications," J. Infrared, Millimeter, Terahertz Waves 40(5), 557–573 (2019).

[66] W. Fan, B. Yan, Z. Wang and L. Wu, "Three-dimensional all-dielectric metamaterial solid immersion lens for subwavelength imaging at visible frequencies," Sci. Adv., vol. 2, no. 8, pp. e1600901, Aug.2016.

126

[67] C. Hsieh, L. Tian, Y. Lu, B. Zhang and G. Barbastathis, "Implementation of the GRIN solid immersion lens," 2012 International Conference on Optical MEMS and Nanophotonics, 2012, pp. 3-4.

[68] Qian Wu, L. P. Ghislain and V. B. Elings, "Imaging with solid immersion lenses, spatial resolution, and applications," in Proceedings of the IEEE, vol. 88, no. 9, pp. 1491-1498, Sept. 2000.

[69] G. Zheng, R. Zhang, S. Li, P. He, H. Zhou and Y. Shi, "A Hyperlens-Embedded Solid Immersion Lens for Beam Focusing Beyond the Diffraction Limit," in IEEE Photonics Technology Letters, vol. 23, no. 17, pp. 1234-1236, Sept.1, 2011.

[70] E. T. F. Rogers, J. Lindberg, T. Roy, S. Savo, J. E. Chad, M. R. Dennis and N. I. Zheludev, "A super-oscillatory lens optical microscope for subwavelength imaging," Nat. Mater., vol. 11, no. 5, pp. 432-435., Mar. 2012.

[71] Y. Zhang, W. Zhong, D. Liu, Y. Zhang and M. Xiao, "Creation of sub-diffraction optical needle by nonlinear super-oscillatory lens," 2016 Conference on Lasers and Electro-Optics (CLEO), 2016, pp. 1-2.

[72] X. Zang, L. Chen, Y. Peng, Z. Jin and Y. Zhu, "Terahertz metalens for manipulating focal point and imaging," 2020 45th International Conference on Infrared, Millimeter, and Terahertz Waves (IRMMW-THz), 2020, pp. 1-2.

[73] H. M. Yao, M. Li and L. Jiang, "Applying Deep Learning Approach to the Far-Field Subwavelength Imaging Based on Near-Field Resonant Metalens at Microwave Frequencies," in IEEE Access, vol. 7, pp. 63801-63808, 2019.

[74] Q. Gao, B. -Z. Wang and X. -H. Wang, "A Novel Compact Metalens to Realize Far-Field Super-Resolution Focusing and Imaging," 2018 International Conference on Microwave and Millimeter Wave Technology (ICMMT), 2018, pp. 1-3.

[75] J. Engelberg, C. Zhou, N. Mazurski, J. Bar-David, U. Levy and A. Kristensen, "Near-IR Wide Field-of-View Huygens Metalens for Outdoor Imaging Applications," 2019 Conference on Lasers and Electro-Optics (CLEO), 2019, pp. 1-2.

[76] V. V. Kotlyar, A. A. Kovalev and A. G. Nalimov, "Planar gradient hyperbolic secant lens for subwavelength focusing and superresolution imaging," Optics, vol. 1, no. 1, pp. 1-10, Dec. 2012.

[77] A. G. Nalimov and V. V. Kotlyar, "Hyperbolic secant slit lens for subwavelength focusing of light," Opt. Lett., vol. 38, no. 15, pp.2702-2704, Aug. 2013.

[78] S. S. Stafeev, E. S. Kozlova, A. G. Nalimov, and V. V. Kotlyar, "Tight focusing of a cylindrical vector beam by a hyperbolic secant gradient index lens," Opt. Lett., vol. 45, no. 7, pp. 1687-1690, Mar. 2020.

[79] T. Baghdasaryan, T. Geernaert, H. Thienpont and F. Berghmans, "Photonic Crystal Mikaelian Lenses and Their Potential Use as Transverse Focusing Elements in Microstructured Fibers," IEEE Photon. J., vol. 5, no. 4, pp. 7100512-7100512, Aug. 2013.

[80] W. Shao and Q. Chen, "2-D Beam-Steerable Generalized Mikaelian Lens with Unique Flat-Shape Characteristic," in IEEE Antennas and Wireless Propagation Letters, vol. 20, no. 10, pp. 2033-2037, Oct. 2021.

[81] J. Chen, H. C. Chu, Y. Lai, Z. Liu, H. Chen, M. Chen and D. Fang, "Conformally Mapped Mikaelian Lens for Broadband Achromatic High Resolution Focusing," Laser Photonics Rev., vol. 15, no. 5, pp. 2000564 Mar. 2021.

[82] W. Y. Shao, H. Sato, X. T. Li, K. K. Mutai, and Q. Chen, "Perforated extensible 3-D hyperbolic secant lens antenna for directive antenna applications using additive manufacturing," Opt. Exp., vol. 29, no. 12, pp. 18932–18949, Jun. 2021.

[83] J. Bor, O. Lafond and M. Himdi, "Creation of a gradient index structure inside foam material - Microwave application for a lens antenna at 60 GHz," 2014 IEEE MTT-S International Microwave Symposium (IMS2014), 2014, pp. 1-4

[84] M. Mueh, V. Mees, M. Maasch and C. Damm, "Fishnets Metamaterial Gradient-Index Lens for Phase Correction of a Horn-Antenna at 60 GHz," 2018 48th European Microwave Conference (EuMC), 2018, pp. 432-435.

[85] N. C. Garcia and J. D. Chisum, "High-Efficiency, Wideband GRIN Lenses With Intrinsically Matched Unit Cells," in IEEE Transactions on Antennas and Propagation, vol. 68, no. 8, pp. 5965-5977, Aug. 2020

[86] A. Papathanasopoulos and Y. Rahmat-Samii, "Multi-Layered Flat Metamaterial Lenses: Design, Prototyping and Measurements," 2020 Antenna Measurement Techniques Association Symposium (AMTA), 2020, pp. 1-6.

[87] N. Zhang, W. X. Jiang, H. F. Ma, W. X. Tang and T. J. Cui, "Compact High-Performance Lens Antenna Based on Impedance-Matching Gradient-Index Metamaterials," in IEEE Transactions on Antennas and Propagation, vol. 67, no. 2, pp. 1323-1328, Feb. 2019.

[88] D. Jia, Y. He, N. Ding, J. Zhou, B. Du and W. Zhang, "Beam-Steering Flat Lens Antenna Based on Multilayer Gradient Index Metamaterials," in IEEE Antennas and Wireless Propagation Letters, vol. 17, no. 8, pp. 1510-1514, Aug. 2018.

[89] A. Dhouibi, S. N. Burokur, A. de Lustrac and A. Priou, "Low-Profile Substrate-Integrated Lens Antenna Using Metamaterials," in IEEE Antennas and Wireless Propagation Letters, vol. 12, pp. 43-46, 2013.

[90] Z. Tao, W. X. Jiang, H. F. Ma and T. J. Cui, "High-Gain and High-Efficiency GRIN Metamaterial Lens Antenna With Uniform Amplitude and Phase Distributions on Aperture," in IEEE Transactions on Antennas and Propagation, vol. 66, no. 1, pp. 16-22, Jan. 2018.

[91] Gytis Kulaitis, "A Statistical Model of Microscope Resolution," Ph.D. dissertation, Institute for Mathematical Stochastics, University of Göttingen, Göttingen, Germany, 2020.

[92] D. W. Hewak and J. W. Y. Lit, "Solution deposited optical waveguide lens," Appl. Opt., vol. 28, no. 19, pp. 4190-4198, 1989.